

# Utilization of Millimeter-Wave Spectrum in Wireless Networks

Lead Guest Editor: Redhwan Q. Shaddad

Guest Editors: Ahmed M. Al-Samman and Murad A. Rassam





---

# **Utilization of Millimeter-Wave Spectrum in Wireless Networks**

Wireless Communications and Mobile Computing

---

## **Utilization of Millimeter-Wave Spectrum in Wireless Networks**

Lead Guest Editor: Redhwan Q. Shaddad

Guest Editors: Ahmed M. Al-Samman and Murad A. Rassam



---

Copyright © 2018 Hindawi. All rights reserved.

This is a special issue published in “Wireless Communications and Mobile Computing.” All articles are open access articles distributed under the Creative Commons Attribution License, which permits unrestricted use, distribution, and reproduction in any medium, provided the original work is properly cited.

## Editorial Board

- Javier Aguiar, Spain  
Wessam Ajib, Canada  
Muhammad Alam, China  
Eva Antonino-Daviu, Spain  
Shlomi Arnon, Israel  
Leyre Azpilicueta, Mexico  
Paolo Barsocchi, Italy  
Alessandro Bazzi, Italy  
Zdenek Becvar, Czech Republic  
Francesco Benedetto, Italy  
Olivier Berder, France  
Ana M. Bernardos, Spain  
Mauro Biagi, Italy  
Dario Bruneo, Italy  
Jun Cai, Canada  
Zhipeng Cai, USA  
Claudia Campolo, Italy  
Gerardo Canfora, Italy  
Rolando Carrasco, UK  
Vicente Casares-Giner, Spain  
Dajana Cassioli, Italy  
Luis Castedo, Spain  
Ioannis Chatzigiannakis, Greece  
Lin Chen, France  
Yu Chen, USA  
Hui Cheng, UK  
Luca Chiaraviglio, Italy  
Ernestina Cianca, Italy  
Riccardo Colella, Italy  
Mario Collotta, Italy  
Massimo Condoluci, Sweden  
Bernard Cousin, France  
Telmo Reis Cunha, Portugal  
Igor Curcio, Finland  
Laurie Cuthbert, Macau  
Donatella Darsena, Italy  
Pham Tien Dat, Japan  
André de Almeida, Brazil  
Antonio De Domenico, France  
Antonio de la Oliva, Spain  
Gianluca De Marco, Italy  
Luca De Nardis, Italy  
Alessandra De Paola, Italy  
Liang Dong, USA
- Trung Q. Duong, Sweden  
Mohammed El-Hajjar, UK  
Oscar Esparza, Spain  
Maria Fazio, Italy  
Mauro Femminella, Italy  
Manuel Fernandez-Veiga, Spain  
Gianluigi Ferrari, Italy  
Ilario Filippini, Italy  
Jesus Fontecha, Spain  
Luca Foschini, Italy  
A. G. Fragkiadakis, Greece  
Sabrina Gaito, Italy  
Óscar García, Spain  
Manuel García Sánchez, Spain  
L. J. García Villalba, Spain  
José A. García-Naya, Spain  
Miguel Garcia-Pineda, Spain  
A.-J. García-Sánchez, Spain  
Piedad Garrido, Spain  
Vincent Gauthier, France  
Carlo Giannelli, Italy  
Carles Gomez, Spain  
Juan A. Gomez-Pulido, Spain  
Ke Guan, China  
Daojing He, China  
Paul Honeine, France  
Sergio Ilarri, Spain  
Antonio Jara, Switzerland  
Xiaohong Jiang, Japan  
Minho Jo, Republic of Korea  
Shigeru Kashihara, Japan  
Dimitrios Katsaros, Greece  
Minseok Kim, Japan  
Mario Kolberg, UK  
Nikos Komninos, UK  
Juan A. L. Riquelme, Spain  
Pavlos I. Lazaridis, UK  
Tuan Anh Le, UK  
Xianfu Lei, China  
Hoa Le-Minh, UK  
Jaime Lloret, Spain  
Miguel López-Benítez, UK  
Martín López-Nores, Spain  
Javier D. S. Lorente, Spain
- Tony T. Luo, Singapore  
Maode Ma, Singapore  
Imadeldin Mahgoub, USA  
Pietro Manzoni, Spain  
Álvaro Marco, Spain  
Gustavo Marfia, Italy  
Francisco J. Martinez, Spain  
Davide Mattera, Italy  
Michael McGuire, Canada  
Nathalie Mitton, France  
Klaus Moessner, UK  
Antonella Molinaro, Italy  
Simone Morosi, Italy  
Kumudu S. Munasinghe, Australia  
Enrico Natalizio, France  
Keivan Navaie, UK  
Thomas Newe, Ireland  
Wing Kwan Ng, Australia  
Tuan M. Nguyen, Vietnam  
Petros Nicopolitidis, Greece  
Giovanni Pau, Italy  
Rafael Pérez-Jiménez, Spain  
Matteo Petracca, Italy  
Nada Y. Philip, UK  
Marco Picone, Italy  
Daniele Pinchera, Italy  
Giuseppe Piro, Italy  
Vicent Pla, Spain  
Javier Prieto, Spain  
Rüdiger C. Pryss, Germany  
Junaid Qadir, Pakistan  
Sujan Rajbhandari, UK  
Rajib Rana, Australia  
Luca Reggiani, Italy  
Daniel G. Reina, Spain  
Abusayeed Saifullah, USA  
Jose Santa, Spain  
Stefano Savazzi, Italy  
Hans Schotten, Germany  
Patrick Seeling, USA  
Muhammad Z. Shakir, UK  
Mohammad Shojafar, Italy  
Giovanni Stea, Italy  
Enrique Stevens-Navarro, Mexico



---

Zhou Su, Japan  
Luis Suarez, Russia  
Ville Syrjälä, Finland  
Hwee Pink Tan, Singapore  
Pierre-Martin Tardif, Canada  
Mauro Tortonesi, Italy

Federico Tramarin, Italy  
Reza Monir Vaghefi, USA  
Juan F. Valenzuela-Valdés, Spain  
Aline C. Viana, France  
Enrico M. Vitucci, Italy  
Honggang Wang, USA

Jie Yang, USA  
Sherali Zeadally, USA  
Jie Zhang, UK  
Meiling Zhu, UK

# Contents

---

## **Utilization of Millimeter-Wave Spectrum in Wireless Networks**

Redhwan Q. Shaddad , Ahmed M. Al-Samman , and Murad A. Rassam  
Editorial (2 pages), Article ID 1641750, Volume 2018 (2018)

## **Spectral and Energy Efficiencies in mmWave Cellular Networks for Optimal Utilization**

Abdulbaset M. Hamed and Raveendra K. Rao   
Research Article (11 pages), Article ID 3097094, Volume 2018 (2018)

## **Measurement Method of Temporal Attenuation by Human Body in Off-the-Shelf 60 GHz WLAN with HMM-Based Transmission State Estimation**

Yusuke Koda , Koji Yamamoto , Takayuki Nishio , and Masahiro Morikura  
Research Article (9 pages), Article ID 7846936, Volume 2018 (2018)

## **Indoor Corridor Wideband Radio Propagation Measurements and Channel Models for 5G Millimeter Wave Wireless Communications at 19 GHz, 28 GHz, and 38 GHz Bands**

Ahmed M. Al-samman , Tharek Abd Rahman , and Marwan Hadri Azmi  
Research Article (12 pages), Article ID 6369517, Volume 2018 (2018)

## **A Stochastic Geometry Approach to Full-Duplex MIMO Relay Network**

Mhd Nour Hindia , Moubachir Madani Fadoul, Tharek Abdul Rahman, and Iraj Sadegh Amiri   
Research Article (11 pages), Article ID 8342156, Volume 2018 (2018)

## **Combined Sector and Channel Hopping Schemes for Efficient Rendezvous in Directional Antenna Cognitive Radio Networks**

AbdulMajid M. Al-Mqdashi, A. Sali, Nor K. Noordin, Shaiful J. Hashim, and Rosdiadee Nordin  
Research Article (19 pages), Article ID 5748067, Volume 2017 (2018)

## Editorial

# Utilization of Millimeter-Wave Spectrum in Wireless Networks

**Redhwan Q. Shaddad** <sup>1</sup>, **Ahmed M. Al-Samman** <sup>2</sup>, and **Murad A. Rassam**<sup>1</sup>

<sup>1</sup>Taiz University, Taiz, Yemen

<sup>2</sup>Universiti Teknologi Malaysia, Johor, Malaysia

Correspondence should be addressed to Redhwan Q. Shaddad; rqs2006@gmail.com

Received 28 May 2018; Accepted 29 May 2018; Published 21 June 2018

Copyright © 2018 Redhwan Q. Shaddad et al. This is an open access article distributed under the Creative Commons Attribution License, which permits unrestricted use, distribution, and reproduction in any medium, provided the original work is properly cited.

To encounter the continuous increasing of bandwidth demand at the end-users of wireless and optical communication networks, the millimeter-wave (MMW) carriers are used for future broadband wireless networks. The next generation of wireless networks is usually developed and implemented based on utilization of the available spectrum in the MMW frequency bands (30–300 GHz) to provide multi-Gigabit networks with high reliable transmission over large distances. The MMW wireless communication suffers from the channel fading which leads to limiting the coverage range and the mobility. To design the wireless networks based on the MMW spectrum, the performance of these networks must be optimized to offer huge data rate, low latency, and high spectrum efficiency.

The recent 5G wireless networks almost utilized are the subband from 28 GHz to 80 GHz in the band of MMW that extended from 30 GHz to 300 GHz. Extensive propagation measurements have been performed at 28 GHz, 38 GHz, and 73 GHz in urban microcellular, urban macrocellular, and/or indoor scenarios. Planning of the 5G wireless network by using MMW frequencies offers high performance capacity, throughput, and QoS compared with microwave frequencies which is applied in the current networks such as Long-Term Evaluation (LTE) wireless networks (2 GHz or 3.6 GHz). The development technologies also make MMW possible for cheap consumer devices such as Full Duplex (FD), Massive Multiple Input Multiple Output (MIMO), Orthogonal Frequency Division Multiplexing Access (OFDMA), and Generalized Frequency Division Multiplexing (GFDM).

When the frequency goes up to the range of MMW, the energy absorption caused by atmosphere, rain, and snow becomes increasingly prominent which causes limitation in

signal transmission distance. In this special issue, most of the accepted papers to be published are proposed to solve these problems.

The first paper “Spectral and Energy Efficiencies in mmWave Cellular Networks for Optimal Utilization” by A. M. Hamed and R. K. Rao is proposed to examine energy efficiency (EE), spectral efficiency (SE), network latency, area spectral efficiency (ASE), and area energy efficiency (AEE) of MMW cellular network in 28 and 73 GHz bands for line-of-sight (LOS) and non-line-of-sight (NLOS) links. This paper presented a frame work for analysis of SE and EE metrics of the network for optimum utilization of network resources. The results have shown that 73 GHz band achieves better SE and the 28 GHz band is superior in terms of EE. It is observed that while the latter band is expedient for indoor networks, the former band is appropriate for outdoor networks.

The second paper “Measurement Method of Temporal Attenuation by Human Body in Off-the-Shelf 60 GHz WLAN with HMM-Based Transmission State Estimation” by Y. Koda et al. conducted a measurement of time-varying signal attenuation induced by human blockage, involving a commercially available IEEE 802.11ad wireless local area network access point (WLAN AP) and wireless station (STA). This paper has estimated signal coexisting at each sampling point using a simple two-state hidden Markov model. The measurements have been validated in that the measured time-varying signal attenuation is in agreement with knife edge diffraction theory.

The third paper “Indoor Corridor Wideband Radio Propagation Measurements and Channel Models for 5G Millimeter Wave Wireless Communications at 19 GHz, 28 GHz, and 38 GHz Bands” by A. M. Al-samman et al. has investigated the propagation characteristics at three different bands 19, 28,

and 38 GHz in an indoor corridor environment for LOS and NLOS scenarios. The results have shown that the received signal power at the higher frequency band is more sensitive to the angle-of-arrival (AOA) variation. It is shown that, within a 1-m receiver movement, the received signal power decreases by up to 11 dB when using the 38 GHz band and the signal only decreased approximately 3 dB for the 19 GHz band.

The fourth paper “Combined Sector and Channel Hopping Schemes for Efficient Rendezvous in Directional Antenna Cognitive Radio Networks” by A. M. Al-Mqdashi et al. has proposed efficient schemes for achieving sector and channel rendezvous in directional antenna cognitive radio networks (DIR-CRNs). Rendezvous is a prerequisite and important process for secondary users (SUs) to establish data communications in CRNs. Two efficient coprimality-based sector hopping schemes have been proposed for providing sector rendezvous in asymmetric and symmetric role environments. The sector hopping (SH) schemes have been combined with an efficient grid-quorum-based channel hopping (CH) scheme for providing a guaranteed sector and channel rendezvous simultaneously between the SUs in DIR-CRNs.

The fifth paper “A Stochastic Geometry Approach to Full-Duplex MIMO Relay Network” by M. N. Hindia et al. has developed a tractable model to analyze the success probability and ergodic capacity of the two-hop MIMO expressions for the random nodes, using tools from stochastic geometry. The results have shown the effect of partial zero forcing (PZF) in mitigating the interferences including the self-interference to demonstrate the feasibility of FD technology even for moderate values of self-interference attenuation.

*Redhwan Q. Shaddad*  
*Ahmed M. Al-Samman*  
*Murad A. Rassam*

## Research Article

# Spectral and Energy Efficiencies in mmWave Cellular Networks for Optimal Utilization

**Abdulbaset M. Hamed and Raveendra K. Rao** 

*Faculty of Engineering, Department of Electrical and Computer Engineering, University of Western Ontario, London, ON, Canada N6A 5B9*

Correspondence should be addressed to Raveendra K. Rao; rrao@uwo.ca

Received 29 September 2017; Revised 18 February 2018; Accepted 28 February 2018; Published 29 April 2018

Academic Editor: Ahmed M. Al-Samman

Copyright © 2018 Abdulbaset M. Hamed and Raveendra K. Rao. This is an open access article distributed under the Creative Commons Attribution License, which permits unrestricted use, distribution, and reproduction in any medium, provided the original work is properly cited.

Millimeter wave (mmWave) spectrum has been proposed for use in commercial cellular networks to relieve the already severely congested microwave spectrum. Thus, the design of an efficient mmWave cellular network has gained considerable importance and has to take into account regulations imposed by government agencies with regard to global warming and sustainable development. In this paper, a dense mmWave hexagonal cellular network with each cell consisting of a number of smaller cells with their own Base Stations (BSs) is presented as a solution to meet the increasing demand for a variety of high data rate services and growing number of users of cellular networks. Since spectrum and power are critical resources in the design of such a network, a framework is presented that addresses efficient utilization of these resources in mmWave cellular networks in the 28 and 73 GHz bands. These bands are already an integral part of well-known standards such as IEEE 802.15.3c, IEEE 802.11ad, and IEEE 802.16.1. In the analysis, a well-known accurate mmWave channel model for Line of Sight (LOS) and Non-Line of Sight (NLOS) links is used. The cellular network is analyzed in terms of spectral efficiency, bit/s, energy efficiency, bit/J, area spectral efficiency, bit/s/m<sup>2</sup>, area energy efficiency, bit/J/m<sup>2</sup>, and network latency, s/bit. These efficiency metrics are illustrated, using Monte Carlo simulation, as a function of Signal-to-Noise Ratio (SNR), channel model parameters, user distance from BS, and BS transmission power. The efficiency metrics for optimum deployment of cellular networks in 28 and 73 GHz bands are identified. Results show that 73 GHz band achieves better spectrum efficiency and the 28 GHz band is superior in terms of energy efficiency. It is observed that while the latter band is expedient for indoor networks, the former band is appropriate for outdoor networks.

## 1. Introduction

The traffic in cellular networks has exponentially increased due to high demand for existing and a variety of new wireless services and growing number of users of networks. Therefore, it has become important to utilize the available bandwidth efficiently. Also, it has become mandatory, due to government regulations on greenhouse gas emissions, to pay careful attention to design of networks that are energy efficient as well. Thus, a key issue in the design and implementation of next generation of cellular networks is the joint optimization of energy and available spectral resources. The mmWave spectrum is known to offer tremendous bandwidth and can be utilized not only to meet the ever increasing demand for high data rate services, but also to accommodate a large number of users. This spectrum is also a serious contender for Ultra

High Definition Video (UHDV) transmission. Several well-known network standards such as ECMA-387, IEEE 802.11ad, and IEEE 802.15.3c are being redefined to fit this spectrum. Despite the massive bandwidth potential in the mmWave band, there exist a number of challenges: (i) modeling and characterization of propagation environment; (ii) design of antenna system; (iii) transceiver integration; (iv) digital signal processing technology.

The mmWave bands suffer from high path loss and hence techniques are required to enhance power received at the receiver. The modeling of propagation environment plays an important role in the design and analysis of communication systems required in cellular networks. In [1], characteristics of mmWave propagation environment are studied and it is observed that bands in this spectrum offer lower delay

spread and it is possible to effectively suppress intersymbol interference. Wells [2] has shown that the 28 and 73 GHz bands are the most natural choices for deployment in the mmWave spectrum. Also, the 28 GHz band is being actively pursued for Local Multipoint Distribution System (LMDS) and is very attractive for use in mmWave cellular networks, given that this band occupies relatively lower range of frequencies within the mmWave spectrum.

In recent years, there have been many efforts to accurately model the mmWave channel for LOS and NLOS transmission links. The communication industry has devoted extensive resources to the development of accurate channel models. For instance, Samsung conducted channel measurements in the 28 GHz band and came up with a model to fit ITU-R and FITU-R standards [3]. This model can be used for a mmWave communication link over a distance of up to 200 meters. In addition, Nokia, Huawei, and Deutsch Telekom have shown keen interest in the 73 GHz band and have developed prototype hardware using the concept of Multiple Input Multiple Output (MIMO) system to support throughput of 20 Gbps. A channel model based on stochastic path loss has been studied for urban propagation environment in [4]. A spatial statistical model of mmWave channel has been developed as a function of channel parameters, including path loss, in [5]. This model has been derived based on real measurements at New York City in 28 and 78 GHz bands for LOS and NLOS links.

A general framework has been proposed for evaluating coverage probability and rate performance in a mmWave cellular network in [6]. The short wavelength of mmWave signals can accommodate a very large number of antennas at the receiver and at the transmitter, which makes beamforming a key enabler technique in obtaining high antenna gain. Beamforming antenna systems for mmWave bands have been studied for 5G networks and a novel hybrid beamforming algorithm has been proposed for indoor and outdoor transmission links [7]. The design and characterization of mmWave antennas for wireless links are discussed in [8, 9].

Shannon's capacity limits and signal processing challenges for giga bit mmWave communication are discussed in [10]. Also, Madhow has addressed opportunities and challenges of utilizing MIMO in LOS mmWave communication systems. An overview of Impulse Radio-Ultra Wide Band (IR-UWB) technology for design of transmitters and receivers is presented in [11]. In [12], coverage and capacity of a dense mmWave network are analyzed using a theoretical model as a function of blockage probability and beamforming bandwidth. Also, the spectral efficiency (SE) (bits/s) of a mmWave network is investigated with LOS and NLOS links in 28 and 73 GHz mmWave bands. Since minimal power consumption has received significance in recent years due to government regulations, it is important to address this issue for mmWave cellular networks. This issue has not received much attention in the literature. The efficiency metrics for LOS and NLOS links are evaluated for 28 and 73 GHz bands in terms of maximum achievable throughput and maximum power efficiency in [13]. However, the work considered only path loss to represent the channel effects for transmission distances up to 200 m. Tan et al. have investigated the achievable

downlink spectral efficiency of multiuser mmWave cellular system considering both small- and large-scale fading effects in [14]. In [15], energy coverage probability was derived for mmWave transmission as a function of network density, beamforming bandwidth, and channel parameters.

The trade-off between energy efficiency and spectral efficiency is examined for different access networks in [16]. It is demonstrated that for best utilization of mmWave bands it is important to understand how to trade tolerable delay for low power. The delay-power trade-off is examined for design of an energy efficient cellular network in [17]. Levanen et al. have proposed technologies to reduce the delay in mmWave communication systems in [18]. The challenges of designing energy efficient mmWave systems are discussed in [19]. The energy efficiency (EE) (bit/J) metric is presented and evaluated for 28 and 73 GHz mmWave bands for LOS and NLOS links. The investigation is presented as a function of BS transmission power, Signal-to-Noise Ratio (SNR), network parameters, and mmWave channel parameters. The spatial characteristics of cellular networks play a significant role in the performance of mmWave cellular networks. The area spectral efficiency (ASE) and the area energy efficiency (AEE) are important metrics that need to be considered in the design of mmWave networks.

Thus, the intent of this paper is to examine energy efficiency (EE), spectral efficiency (SE), network latency, area spectral efficiency (ASE), and area energy efficiency (AEE) of mmWave cellular network in 28 and 73 GHz bands for LOS and NLOS links. The investigation is presented as a function of SNR, channel model parameters, network parameters, user distance from BS, and BS transmission power. This paper is organized as follows: In Section 2, mmWave cellular system is introduced including cellular network model, mmWave signal propagation and wireless channel models, and NR and SINR calculations. Section 3 presents evaluation of network performance metrics, spectral efficiency, energy efficiency, spatial spectral and energy efficiencies, network latency, and outage probability. Also, the evaluation of these efficiencies metrics is discussed. Simulation algorithm and the assumptions that have been made for our analysis are listed in Section 4. Moreover, the network and channel parameters are tabulated, and the numerical results with discussion are also presented. Finally, the work is concluded in Section 5.

## 2. Millimeter Wave Cellular System

The model of mmWave cellular system is shown in Figure 1. The macrocells are divided into small cells shown in the figure. The  $J$  macrocells in the network are ( $j = 1, \dots, J$ ) using the same frequency and therefore create intercell interference. Each of the  $j$ th cells comprises  $I$  small cells each with its own BS ( $i = 1, \dots, I$ ) and uses the same frequency thereby causing intracell interference. It is assumed that each small cell has one BS and it serves  $K$  Mobile Users (MUs) ( $k = 1, \dots, K$ ). The BSs are located at the center of small cells and connected to the gateway of the macrocell. The MUs are spatially distributed and each one is associated with a single BS at any time.

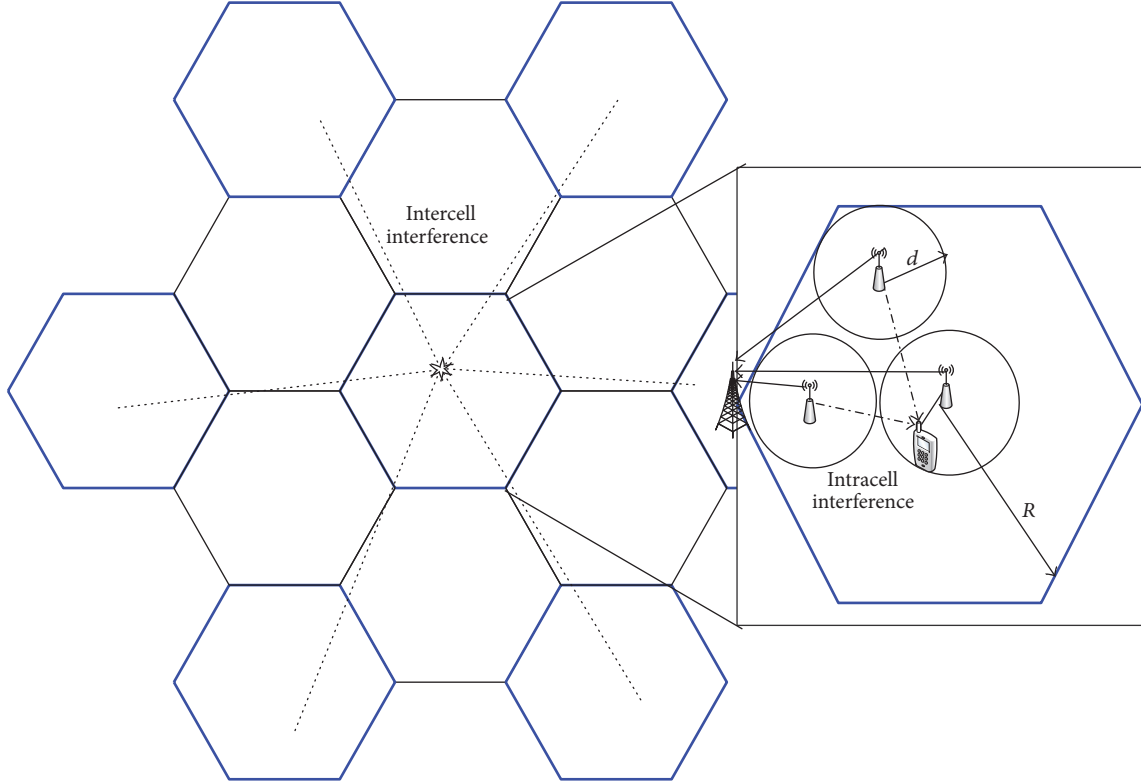


FIGURE 1: Model of mmWave cellular network in which the links “-.-” are for intracell interference, “...” for intercell interference, and “—” for transmission between BSs where the cochannel macrocells are remarked in blue colour.

**2.1. mmWave Wireless Channel Model.** The mmWave signal is susceptible to high path loss, fading, noise, and interference; all these cause serious degradation in Signal-to-Noise Ratio (SNR) at the receiver leading to poor overall system performance. In general, mmWave communication channel can be represented by the double directional channel model given in [20] and is given by

$$\mathbf{H} = \sum_{q=1}^Q \sum_{c=1}^C H_{q,c} e^{j\phi_{q,c}} \delta(\tau - \tau_{q,c}) \delta(\phi_R - \phi_{AoA,q,c}) \cdot \delta(\phi_T - \phi_{AoD,q,c}) \delta(\theta_R - \theta_{ZoA,q,c}) \delta(\theta_T - \theta_{ZoD,q,c}), \quad (1)$$

where  $Q$  is the number of multipath components;  $C$  is the number of rays within the cluster. Each ray is represented by path gain  $H_{q,c}$ , phase  $\phi_{q,c}$ , time-of-arrival (ToA)  $\tau_{q,c}$ , azimuth angle-of-arrival (AoA)  $\phi_{AoA,q,c}$ , azimuth angle-of-departure (AoD)  $\theta_{AoD,q,c}$ , zenith angle-of-arrival (ZoA)  $\theta_{ZoA,q,c}$ , and zenith angle-of-departure (ZoD)  $\theta_{ZoD,q,c}$ . The task of channel modeling is thus to find all these parameters for a mmWave communication channel. For 28 and 73 GHz frequency bands, a model has been obtained to fit the LOS and NLOS transmission links. These bands were selected since they are the bands likely to be deployed in mmWave cellular network. According to this model [4], small-scale fading has a less impact on mmWave signal propagation, and hence the large-scale fading effect is considered in measurements. In [5],

mmWave channel path loss effects are considered and a statistical model based on realistic measurements is presented for an urban environment, LOS and NLOS links, and is given by

$$L_{N/LOS} [\text{dB}] = \alpha + \beta 10 \log_{10}(r) + \xi [\text{dB}], \quad (2)$$

$$\xi \sim \mathcal{N}(0, \sigma_s^2),$$

where  $L_{N/LOS}$  is the path loss in dB,  $r$  is the distance between transmitter and receiver in meters,  $\alpha$  and  $\beta$  are the least square fits of floating intercept and slope over the measured distances up to 200 m, and  $\sigma_s^2$  is the variance of the lognormal shadowing,  $\xi$ . In this paper, the channel model given by (2) [5] is used and the values of model parameters  $\alpha$ ,  $\beta$ , and  $\sigma_s^2$  are given in Table 1.

**2.2. Signal-to-Noise Ratio Calculation.** The path loss model given by (2) is used to determine the received signal power at the MU and then used to estimate SNR of the  $k$ th MU in the  $i$ th BS. That is,

$$\begin{aligned} \text{SNR}_{i,k[\text{dB}]} &= 10 \log_{10} |h_{i,k}|^2 + P_{i[\text{dBm}]} + G_{i[\text{dBi}]} + G_{k[\text{dBi}]} \\ &\quad - L_{i,k[\text{dB}]}(r_{i,k}) \\ &\quad - (\text{KT}_{[\text{dBm/Hz}]} + 10 \log_{10}(W_{mu}) + \text{NF}_{[\text{dB}]}) \end{aligned} \quad (3)$$

TABLE 1: Parameters of statistical channel model [5].

Path loss parameter	$\alpha$	$\beta$	$\sigma_s^2$	$\nu$
28 GHz				
NLOS	72	2.92	8.7	1
LOS	61.4	2	5.8	5
73 GHz				
NLOS	86.6	2.45	8.0	1
LOS	69.8	2	5.8	8

where  $P_i$  is the BS <sub>$i$</sub>  transmission power, KT is the noise power density at the MU, and NF is the noise figure. The transmitter and receiver antenna gains,  $G_i$  and  $G_k$ , are calculated using  $G = 20\log_{10}(\pi l/\lambda)$  for the 28 and 73 GHz frequency bands and antenna length of  $l$ . Assuming an independent Nakagami fading for each link, the small-scale fading component,  $|h_{i,k}|^2$ , can be modeled as a normalized Gamma random variable, that is,  $|h_{i,k}|^2 \sim \mathcal{G}(\nu, 1/\nu)$  [15]. The small-scale fading is considered less severe in mmWave band [12], and hence  $\nu$  is very large integer for LOS link, and  $\nu = 1$  when the link is NLOS. The path loss component  $L_{i,k}$  can be calculated using (2).

**2.3. Signal-to-Interference-Plus-Noise Ratio (SINR) Model.** Based on the network model shown in Figure 1, for the  $k$ th MU in the  $i$ th small cell serving BS in the  $j$ th macro cell, the interference consists of two components which are intracell interference and intercell interference. The first one is caused by the active BSs located in the same  $j$ th cell which is more severe since it is close to the MU. While the second component is generated from the BSs in the other macro cells which is less intense. When the cochannel interference due to first tier macrocell is considered, the downlink aggregated interference in the  $s$  small cell BS and  $p$  macro cell for the  $k$ th MU can be expressed as

$$\begin{aligned} \Lambda_{j,i,k} = & \sum_{\substack{i=1 \\ i \neq s}}^I P_{p,i} G_{p,i} G_{p,s,k} |h_{p,i,k}|^2 L_{p,i,k}(r_{i,k}) \\ & + \sum_{\substack{j=1 \\ j \neq p}}^J \sum_{i=1}^I P_{j,i} G_{j,i} G_{j,i,k} |h_{j,i,k}|^2 L_{j,i,k}(r_{j,i,k}). \end{aligned} \quad (4)$$

Therefore, the SINR at the MU <sub>$k$</sub>  for BS <sub>$i$</sub>  is given by

$$\text{SINR}_{j,i,k[\text{dB}]} = \text{SNR}_{i,k[\text{dB}]} - 10 \log_{10} \left( \frac{\Lambda_{i,k}}{\sigma_k^2} + 1 \right), \quad (5)$$

where  $\sigma_k^2$  is the thermal noise power at the  $k$ th MU. The distance between BS and MU (3) and (4) is <200 m and is a random variable with probability distribution function  $f_d(r) = 2r/d^2$ .

### 3. Energy and Spectral Efficiency of mmWave Network

Energy and spectrum are system resources that have to be appropriately traded to efficiently design a mmWave

communication system. Minimal use of energy resources in the systems has become an important issue; however, efficient use of mmWave spectrum requires more power due to high path loss. Therefore, a balance between the use of energy and spectral resources of the system deserves a careful study. This is examined in this section for a mmWave cellular network. Analysis of energy and spectral efficiency metrics for such network is considered which can play an important role in the standardization of mmWave cellular network.

**3.1. Network Spectral Efficiency.** The downlink spectral efficiency quantifies the amount of data rate delivered by the BS to MUs over a certain bandwidth,  $W_k$ . This indicates how efficiently the mmWave spectrum is utilized. Spectral efficiency is bounded by Shannon's limit  $W_k \log_2(1 + \text{SNR}_k)$  [21] for a given SNR. For the case of mmWave network SNR is replaced by SINR. Thus, spectral efficiency of the network, depicted in Figure 1, can be evaluated using

$$\begin{aligned} \eta_{\text{SE}} = & \sum^J \sum^I \sum^K W_k \mathbb{E}_r \left[ \mathbb{E}_h \left[ \log_2(1 + \text{SINR}_{j,i,k}) \right] \right] \\ & \cdot (1 - P_{\text{out},j}(R)), \text{ (bit/s)}, \end{aligned} \quad (6)$$

where SINR can be obtained from (5), and  $W_k$  is the allocated mmWave bandwidth for the MUs.  $\mathbb{E}_r$  and  $\mathbb{E}_h$  are the expectation values taken for over MU's random location and the small-scale fading effect, respectively. The outage probability within a communication range  $R$ ,  $P_{\text{out},j}$ , is given by [22]

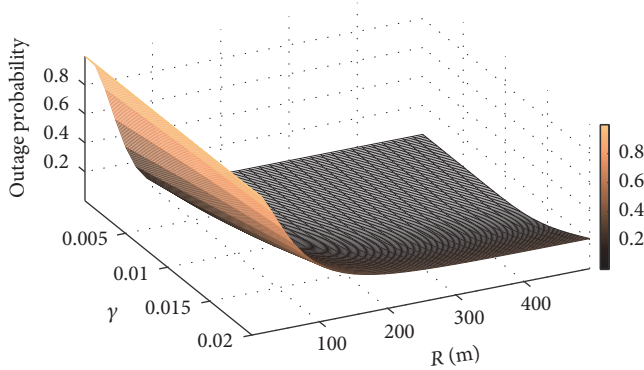
$$P_{\text{out},j}(R) = \exp \left( -\frac{2\pi\rho_j}{\gamma_j^2} (1 - (1 + \gamma_j R) e^{-\gamma_j R}) \right), \quad (7)$$

where  $\gamma$  is the parameter that depends on the propagation environment density, and  $\rho$  is the BS density. The outage probability is plotted as a function of  $\gamma$  and  $R$  for a given  $\rho = 10^{-4}$  in Figure 2. It is observed that  $P_{\text{out}}$  is nearly constant for  $R > 300$  m. Since the proposed network dimensions are large, with macro cell radius  $R \geq 500$  m, the outage probability can be approximated by  $P_{\text{out},j} = e^{-2\pi\rho_j/\gamma_j^2}$ .

**3.2. Network Energy Efficiency.** The energy efficiency is defined as a ratio between what the system delivers to what it consumes, and hence the efficiency function can be described as  $f(x)/x$ , where  $x \in [0, X]$  indicates the system's resources constrained by  $X$  [23]. In this paper,  $f(x)$  represents the

TABLE 2: Parameters used in the simulation of cellular network.

Symbol	Descriptions	Value
$W_k$	User bandwidth	0.1 GHz
$P_t$	BS transmission power	-10 dBm-40 dBm
KT	Noise power density	-174 dBm/Hz
NF	Noise figure	6 dB
$d$	Maximum BS serving distance	100 m
$R$	Macro cell radius	500 m
$J$	Maximum number of cells sharing the spectrum	7
$I$	Maximum number of BSs in the macro cell	$uniform \sim 1/\rho$
$K$	Number of simultaneous users in BSs	20
$\rho$	BS density	$\left(\frac{d}{R}\right)^2$
$\gamma$	Propagation environment density	$10^{-2}$
$l_t$	Transmitter antenna length	0.1 m
$l_r$	Receiver antenna length	0.005 m

FIGURE 2: Outage probability as a function of  $\gamma$  and  $R$  for  $\rho = 10^{-4}$ .

overall downlink data rate efficiency that can be reliably transmitted by a mmWave communication system, and  $x$  denotes the Signal-to-Noise Ratio, which is a function of BS's transmission power, noise, and channel effects. For the mmWave network, the energy efficiency can be formulated as

$$\eta_{EE} = \sum_{j=1}^J \sum_{i=1}^I \sum_{k=1}^K W_k \mathbb{E}_r \left[ \mathbb{E}_h \left[ \frac{\log_2(1 + \text{SINR}_{j,i,k})}{\text{SNR}_{j,i,k}} \right] \right] \cdot (1 - P_{\text{out},j}(R)), \text{ (bit/J)}, \quad (8)$$

where SNR and SINR can be determined using (3) and (5), respectively. The energy efficiency indicates the amount of data rate that can be delivered per unit of SNR per Hertz of bandwidth. The efficiency metrics are useful in the standardization of mmWave cellular networks, as spectral efficiency provides the maximum rate for each frequency band and transmission range and energy efficiency gives insight into how to utilize the energy resources in cells as a function of data rate.

**3.3. Spatial Spectral and Energy Efficiency.** Spatial characteristics of mmWave network are crucial in the evaluation of system performance. For example, the propagation loss is highly affected by network dimensions, and hence SNR and SINR are also impacted. Therefore, studying the spectral and energy efficiencies is not enough for efficient design of mmWave networks. The spatial spectral and energy efficiencies are better metrics for design of networks [24]. Accordingly, these metrics are examined for mmWave networks. These metrics are evaluated for macrocell as a sum of each small cell spatial efficiency in which the serving distance,  $r$ , determines the cells' area.

## 4. Numerical Results

Monte Carlo simulations have been performed in MATLAB environment to evaluate spectral, energy and spatial spectral and energy efficiencies for the 28 and 73 GHz mmWave bands. The efficiency metrics are investigated in terms of BS transmission power, BS serving distance, and SNR. The steps used in the simulation are given below:

- (1) The path loss for 28 and 73 GHz bands is calculated for LOS and NLOS using (2) for each value of  $P$  and  $r$ , and the model parameters are given in Table 1.
- (2) SNR is computed using (3), in which small-scale fading is modelled using Gamma distribution,  $|h|^2 \sim \mathcal{G}(v, 1/v)$ , and (3) parameters are given in Table 2.
- (3) For the network model, Figure 1, the aggregated intercell and intracell interferences are obtained using (4).
- (4) The SINR is determined (5) for  $\sigma_k^2 = KTW_k$ .
- (5) Spectral and energy efficiency metrics are computed using (6) and (8) with  $P_{\text{out}}$  calculated using (7); see Figure 2.
- (6) The spatial spectral and energy efficiency metrics are computed using  $\sum(\eta_{SE,j,i,k}/A_{j,i})$  and  $\sum(\eta_{EE,j,i,k}/A_{j,i})$ ,

respectively, with  $A_{j,i} = \pi d_{j,i}^2$  being the coverage area of each small cell BS [25].

The following assumptions are made in Monte Carlo simulation.

- (1) Channel fading coefficients,  $h_{i,j,k}$ , in (3) and (4) are independent and identical distributed random variables.
- (2) Transmission power,  $P_i$ , in (3), is identical for all small cell BSs.
- (3) Antenna gain,  $G_j$ , is equal for all BSs that are assumed to be same, and antenna gain,  $G_k$ , for all MUs is assumed to be identical.
- (4) Intercell interference is based on only the first tier of the macrocells.
- (5) Intercell distance,  $r_{i,j,k} = 3R + d$ , and the intracell distance,  $r_{i,k} = 2d$ , represent the worst MUs in small cells.
- (6) Macro cell radius of  $R = 500$  m is assumed and the maximum serving distance of a small cell BS is set to  $d = 100$  m.

The cellular network parameters used in the simulations are given in Table 2. Simulation and numerical process of this work are summarized in the flow chart shown in Figure 3.

**4.1. Spectral Efficiency.** The spectral efficiency of the network is evaluated in terms of achievable data rate for a specific allocated bandwidth to MU. This efficiency metric (bit/s) is plotted in Figure 4 as a function of maximum serving distances for LOS and NLOS links in 28 and 73 GHz bands with transmission power fixed at 10 dBm. It is observed that the maximum achievable data rate in the network can reach 1 Tbit/s as  $d$  is diminished. In this case, the macrocell will have a large number of small cells and intracell interference is increased. Also, it is noted that the spectral efficiency slightly deteriorates for LOS link while for NLOS link it decreases rapidly to 0.15 G bit/s for  $d = 100$  m. The spectral efficiency is also investigated as a function of BS power used for transmission for a specific value of serving distance,  $d = 45$  m. Figure 5 demonstrates that the spectral efficiency is enhanced as power transmitted by the BS is increased. It is observed that there is no significant improvement in the spectral efficiency when the transmission power is above 40 dBm. This indicates that pumping more power is waste of BS power resource and hence impacts the energy efficiency. Thus, for optimum mmWave band utilization, transmission power over 40 dBm is not required. The figure also illustrates the superiority of high frequency band, 73 GHz, for the LOS link.

For high power transmission, the achieved spectral efficiencies of the two transmission bands are above 1 Tbit/s. Since the SNR at MUs is a function of the BS transmission power, receiver noise, and channel effects, the spectral efficiency for the 73 GHz band for LOS link is presented in Figure 6 as a function of serving distance and SNR. It is noted that the spectral efficiency is an increasing function of SNR

which indicates the mmWave system can overcome the noise and channel impairments. The spectral efficiency of mmWave cellular networks has been investigated in [14, 26] and the numerical results presented in these works are consistent with the results illustrated in Figure 5. However, the spectral efficiency results of this paper are based on real channel measurements.

**4.2. Energy Efficiency.** Energy efficiency metric is a “green communication” indicator, since the transmitted power by the BS plays an important role in its determination. The energy efficiency metric is a function of the data rate over the mmWave links and SNR at MUs. The energy efficiency is examined as a function of BS serving distance, the transmission power, and the SNR. The metric is plotted as a function of transmission power for two mmWave bands and links in Figure 7. It is observed that the 73 GHz band is less energy efficient compared to the 28 GHz band. The energy efficiency is degraded as the transmission power is increased. Figure 8 shows a comparison of energy efficiency between the two frequency bands for LOS transmission link as a function of  $d$  and SNR. It is observed that 28 GHz band, Figure 8(b), attains higher energy efficiency than the 73 GHz band, Figure 8(a). In fact, the SNR for LOS transmission at 73 GHz band is greater than the SNR for NLOS link at the 28 GHz band. Also, it is noted that the efficiency improves up to certain serving distance,  $d = 30$  m, and then becomes almost constant for  $d > 30$  m. It is noted that trade-off between serving distance and the transmission power has to be considered in dimensioning of the network and for optimum utilization for the two mmWave bands. Energy efficiency of mmWave cellular network has been examined in terms of number of users and BS antenna size for full-duplex relaying backhaul small cell mmWave networks in [19] for 28 GHz and 60 GHz bands. The results show an increasing function of the transmitted power which contradicts the energy efficiency concept illustrated in Figure 7. Also, this metric has been investigated in terms of propagation environment parameters and BS density for heterogeneous mmWave network overlaid by small cell BSs in [22]. The results are consistent with the results illustrated in Figure 8.

**4.3. Network Latency.** Delay is critical metric for real time applications in mmWave networks. Thus, it is important to address the network delay as a function of network parameters. The delay in mmWave networks is due to several components such as radio access network, backhaul, core network, and data centers. In this paper, we consider the transmission delay between MU and BS. For a given user bandwidth and information quantity  $Q_k$ , the transmission delay  $D$  is given by  $D = Q_k/C$  [27]. For the network shown in Figure 1, the delay-per-bit per user can be expressed as

$$D_k = \frac{Q_k}{W_k \mathbb{E}_r \left[ \mathbb{E}_h \left[ \log_2 \left( 1 + \text{SINR}_{j,i,k} \right) \right] \right] \left( 1 - P_{\text{out},j}(R) \right)}, \quad (9)$$

where  $Q_k = 1$  and  $\text{SINR}_{j,i,k}$  is given by (5). The trade-off among latency and efficiency metrics of the mmWave

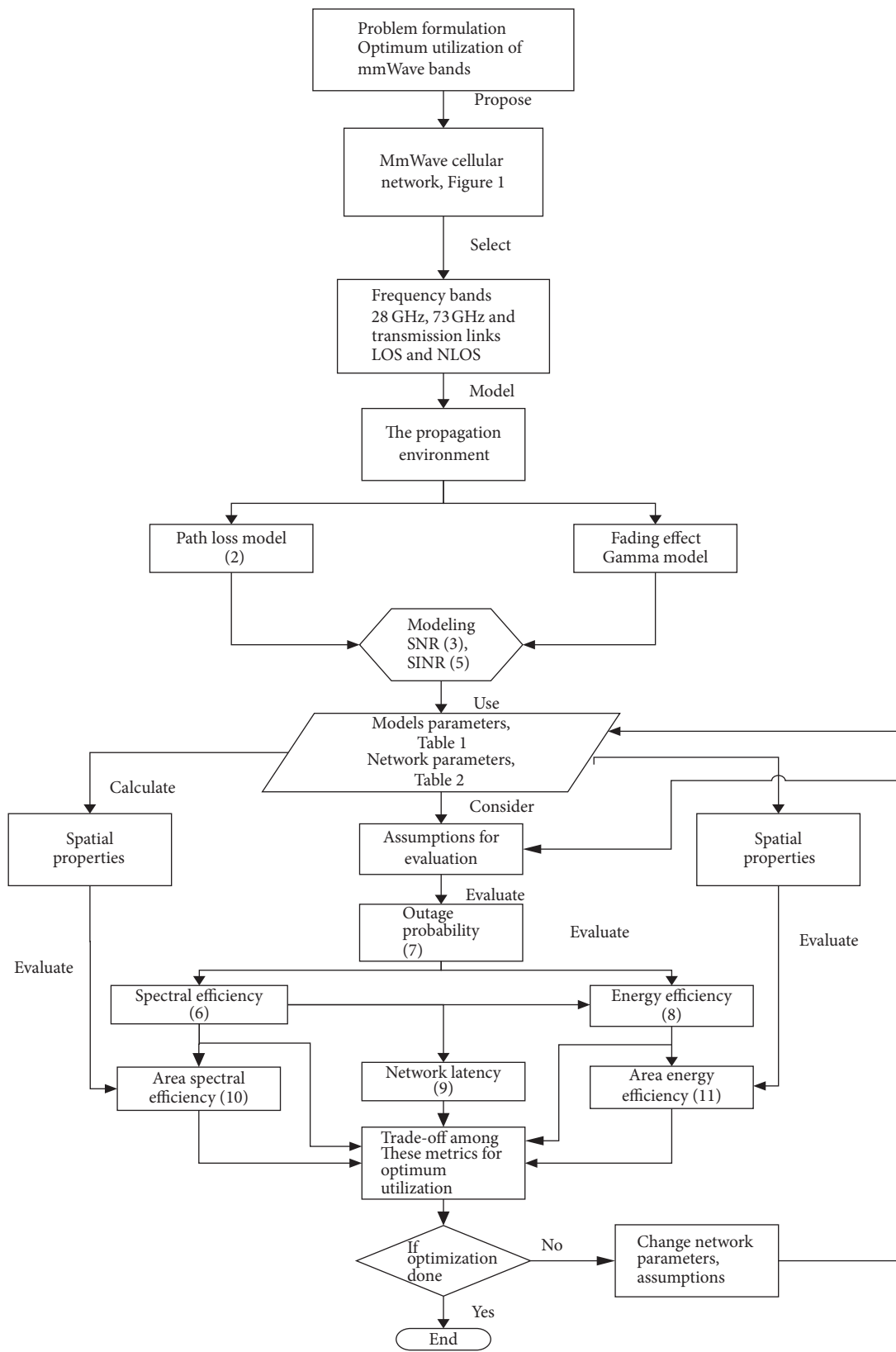


FIGURE 3: Flow chart used for evaluation of trade-off between spectral and energy efficiencies for optimum utilization in mmWave network.

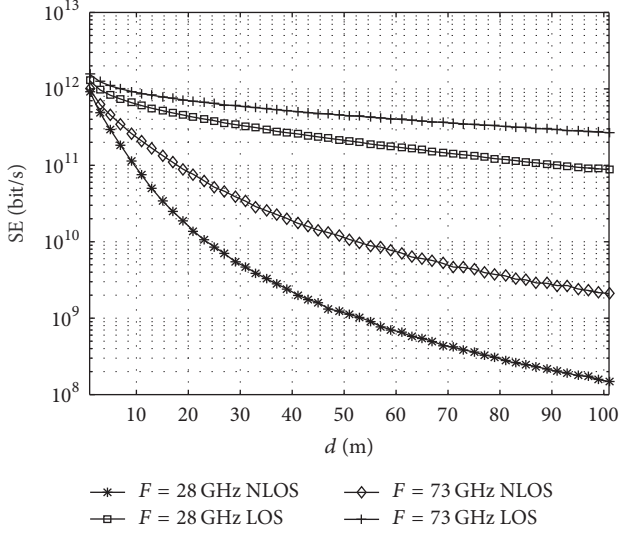


FIGURE 4: Spectral efficiency of 28 GHz and 73 GHz mmWave bands for NLOS and LOS links as a function of the maximum serving distance.

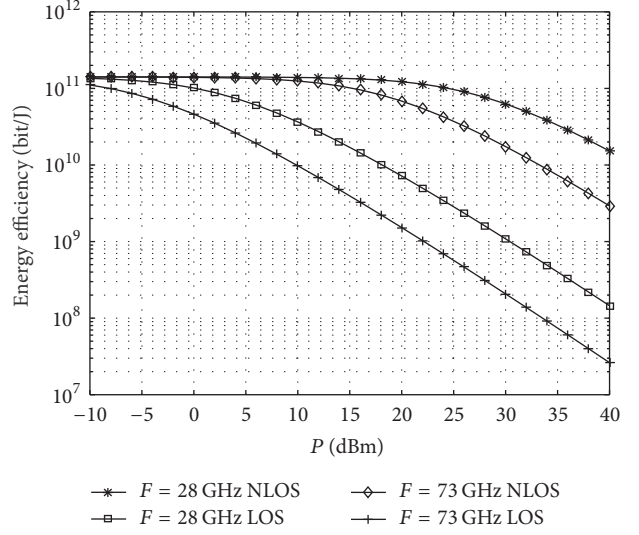


FIGURE 7: Energy efficiency of 28 GHz and 73 GHz mmWave bands for NLOS and LOS links as a function of BS power.

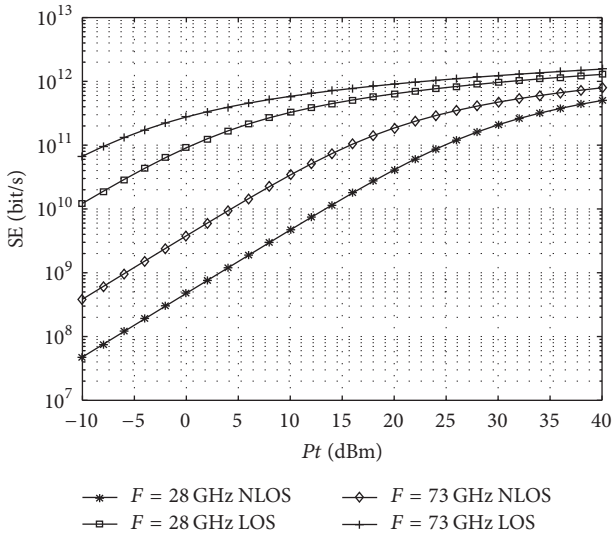


FIGURE 5: Spectral efficiency of 28 GHz and 73 GHz mmWave bands for NLOS and LOS links as a function of transmission power.

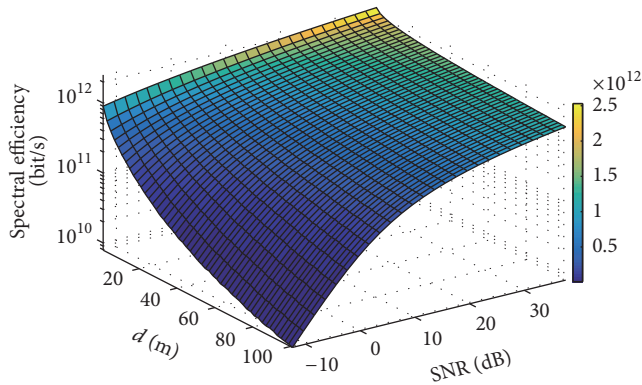


FIGURE 6: Spectral efficiency of 73 GHz band LOS link as a function of  $d$  and SNR.

network can be discussed in terms of delay-per-bit and energy efficiency. Delay-per-bit is obtained by simulating (9) using channel parameters given in Table 1 and network parameters given in Table 2. The delay is plotted as a function of BS power and user distance in Figures 9(a) and 9(b), respectively. These figures show that 73 GHz band for LOS link achieves less latency than the 28 GHz band for NLOS link. Figure 9(a) shows that the delay decreases as the BS power increases. For example, the network latency is less than 1 ns/bit when the BS power is greater than 20 dBm. The energy efficiency is highly impacted for such large values of BS power as shown in Figure 7. In terms of user distance, the network latency increases as the distance increases as is clear from Figure 9(b). In contrast the spectral efficiency is reduced as a function of user distance which indicates that the two metrics are in conflict. Therefore, trade-offs among network latency, energy efficiency, and spectral efficiency metrics must be considered for optimum utilization of the mmWave bands.

**4.4. Area Spectral Efficiency.** The area spectral efficiency (ASE) is defined as the ratio of the average spectral efficiency to the utilized area for a given frequency band. For the network in Figure 1, The ASE is calculated as the sum of the spectral efficiencies of each small cell divided by its serving area and is given by

$$\sum \frac{\eta_{SE,j,i,k}}{A_{j,i}}. \quad (10)$$

This ASE metric links the network spectral efficiency and the service area and is investigated as a function of  $P$ ,  $d$ , and SNR. In Figure 10(a), ASE is plotted in terms of  $d$ . It is noted that ASE is a decreasing function of the distance since the area is proportional to  $d^2$ . Also, ASE is plotted in terms of  $d$  and SNR in Figure 10(b) which depicts how both factors affect the ASE. It is clear that for large coverage area the network requires more BS power to achieve acceptable ASE.

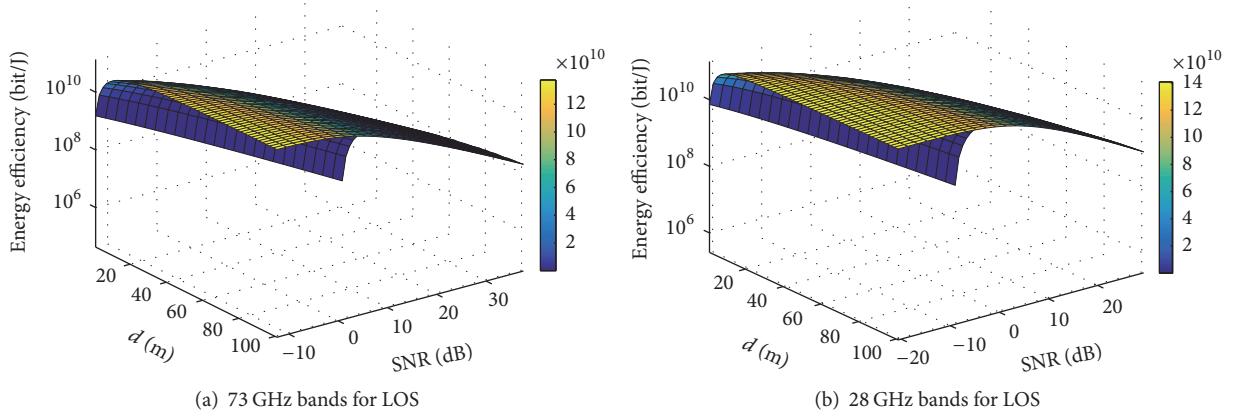
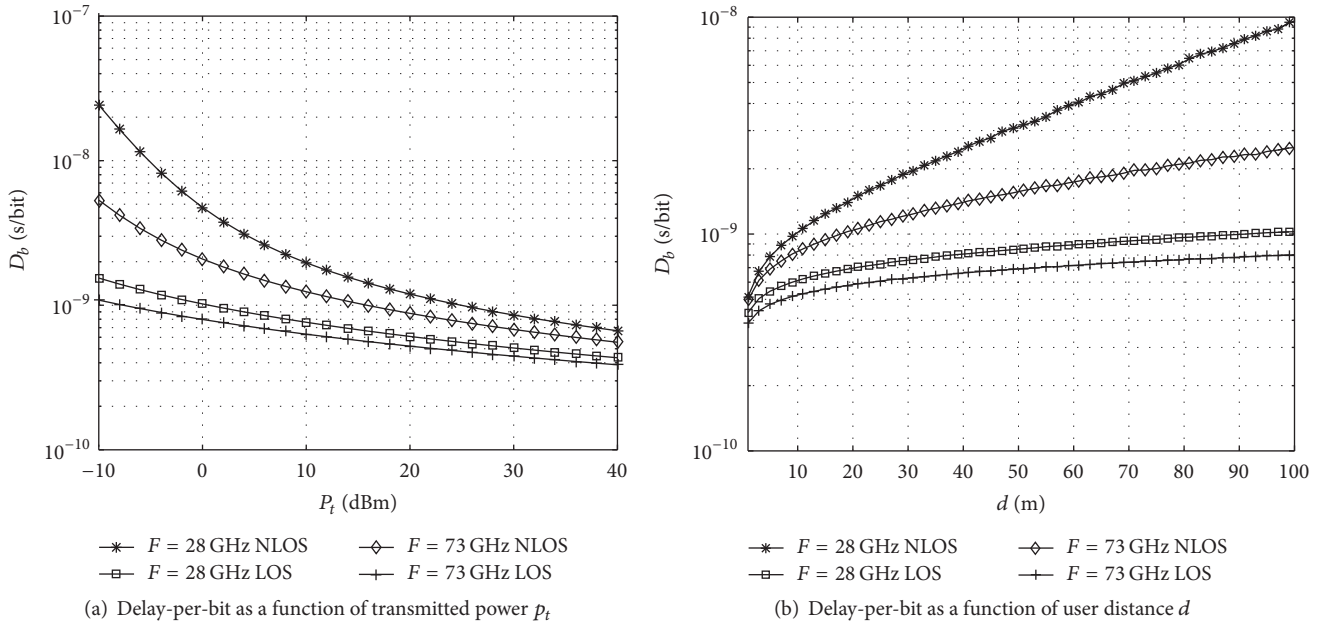

 FIGURE 8: Energy efficiency of 73 and 28 GHz bands for LOS link as a function of  $d$  and SNR.


FIGURE 9: Delay-per-bit for 73 and 28 GHz bands for LOS and NLOS links.

**4.5. Area Energy Efficiency (AEE).** The AEE is used to characterize the area data rate per unit BS power expenditure and can be defined as

$$AEE = \sum \frac{\eta_{EE,j,i,k}}{A_{j,i}}, \quad (11)$$

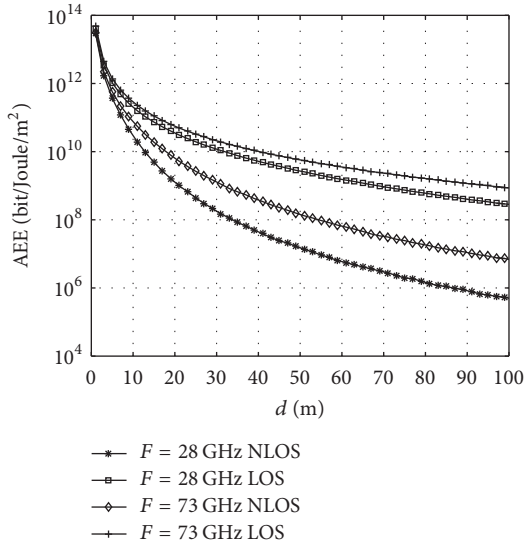
where  $\eta_{EE,j,i,k}$  is given by (8) and  $A_{j,i} = \pi d_{j,i}^2$ . This metric provides insight into the deployment and implementation challenges for optimum mmWave band utilization. The AEE is evaluated as a function of BS power and is shown in Figure 11(b). The metric severely deteriorates for high values of BS power; however, it maintains a certain level of performance at lower values of power. Also, it is observed that AEE slightly decreases as the radius of small cell increases as shown in Figure 11(a).

From the above results, it is clear that there is always a conflict between spectral efficiency and energy efficiency

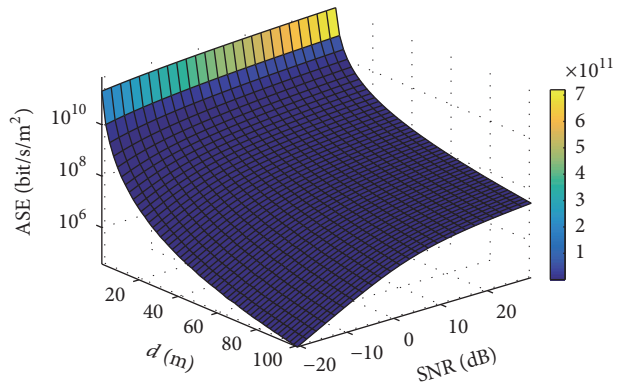
in terms of power transmission. The optimum utilization of mmWave bands requires trade-off between these two performance metrics. The 28 GHz band achieves higher energy efficiency for a wide range of power transmission level while it provides acceptable spectral efficiency for  $P_t > 20$  dBm. On the other hand, the 73 GHz is superior in terms of spectral efficiency; however, it performs poorly with respect to energy efficiency. Regarding the transmission environment, it can be said that the 28 GHz band is more advantageous than the 73 GHz band for NLOS links such as indoor networks. However, the 73 GHz bands are more suitable for LOS link such as outdoor mmWave links.

## 5. Conclusions

In this paper, mmWave cellular network is considered for indoor and outdoor applications in which the macrocells are

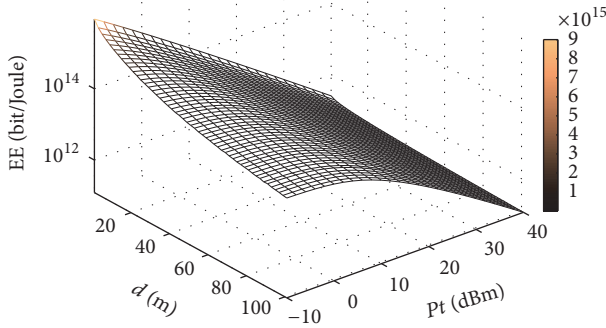


(a) ASE of 73 and 28 GHz bands for LOS and NLOS links as a function of BS serving distance

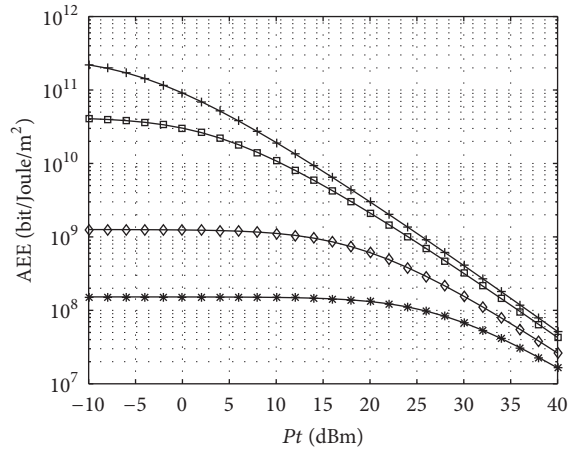


(b) ASE of 73 GHz band LOS as function of d and SNR

FIGURE 10: Area spectral efficiency of mmWave bands.



(a) AEE 73 GHz band LOS



(b) AEE of 73 and 28 GHz bands for LOS and NLOS

FIGURE 11: Area energy efficiency of mmWave bands as a function of  $d$  and  $P$ .

overlaid with multiple small cells. A channel model based on real measurements available in literature for LOS and NLOS transmission links was used to derive expressions for SNR and SINR in network considering intercell and intracell interference components. The paper presented a framework for analysis of spectral and energy efficiency metrics of the network for optimum utilization of network resources. The framework also included an investigation of spectral efficiency, energy efficiency, and spatial performance metrics. The analysis was done using Monte Carlo simulation considering the effects of interference, the path loss, and small-scale fading. The investigation of metrics has been

carried out as a function of BS power, SNR, mmWave network parameters, and channel model parameters. The results show that the spectral efficiency is always in conflict with the energy efficiency with regard to BS power and the maximum BS serving distance. The 28 GHz band can be expedient for NLOS links in the network, and the 73 GHz band is more appropriate for LOS links.

### Conflicts of Interest

The authors declare that they have no conflicts of interest.

## Acknowledgments

The first author would like to acknowledge University of Tripoli, Libya, and the Libyan Ministry of Education for their support and scholarship.

## References

- [1] Y. Li, P. Wang, F. Chen, G. Wang, and Y. Liu, "Simulation and Analysis of Millimeter-Wave Propagation Characteristics in Complex Office Environment," *Journal of Computer and Communications*, vol. 03, no. 03, pp. 56–60, 2015.
- [2] J. Wells, "Faster than fiber: The future of multi-G/s wireless," *IEEE Microwave Magazine*, vol. 10, no. 3, pp. 104–112, 2009.
- [3] J. Ko, Y.-S. Noh, Y.-C. Kim et al., "28 GHz millimeter-wave measurements and models for signal attenuation in vegetated areas," in *Proceedings of the 11th European Conference on Antennas and Propagation, EUCAP 2017*, pp. 1808–1812, France, March 2017.
- [4] T. Bai, V. Desai, and R. W. Heath Jr., "Millimeter wave cellular channel models for system evaluation," in *Proceedings of the 2014 International Conference on Computing, Networking and Communications, ICNC 2014*, pp. 178–182, USA, February 2014.
- [5] M. R. Akdeniz, Y. Liu, M. K. Samimi et al., "Millimeter wave channel modeling and cellular capacity evaluation," *IEEE Journal on Selected Areas in Communications*, vol. 32, no. 6, pp. 1164–1179, 2014.
- [6] L. Zhao, J. Cai, and H. Zhang, "Radio-efficient adaptive modulation and coding: Green communication perspective," in *Proceedings of the 2011 IEEE 73rd Vehicular Technology Conference, VTC2011-Spring*, Hungary, May 2011.
- [7] W. Roh, J.-Y. Seol, J. Park et al., "Millimeter-wave beamforming as an enabling technology for 5G cellular communications: theoretical feasibility and prototype results," *IEEE Communications Magazine*, vol. 52, no. 2, pp. 106–113, 2014.
- [8] X. Wu, G. V. Eleftheriades, and T. E. Van Deventer-Perkins, "Design and characterization of single- and multiple-beam MM-wave circularly polarized substrate lens antennas for wireless communications," *IEEE Transactions on Microwave Theory and Techniques*, vol. 49, no. 3, pp. 431–441, 2001.
- [9] Y. P. Zhang and D. Liu, "Antenna-on-chip and antenna-in-package solutions to highly integrated millimeter-wave devices for wireless communications," *IEEE Transactions on Antennas and Propagation*, vol. 57, no. 10, pp. 2830–2841, 2009.
- [10] U. Madhow, "MultiGigabit millimeter wave communication: System concepts and challenges," in *Proceedings of the 2008 Information Theory and Applications Workshop - ITA*, pp. 193–196, USA, February 2008.
- [11] C. Stallo, E. Cianca, S. Mukherjee, T. Rossi, M. de Sanctis, and M. Ruggieri, "UWB for multi-gigabit/s communications beyond 60 GHz," *Telecommunication Systems*, vol. 52, no. 1, pp. 161–181, 2013.
- [12] T. Bai, A. Alkhateeb, and R. W. Heath, "Coverage and capacity of millimeter-wave cellular networks," *IEEE Communications Magazine*, vol. 52, no. 9, pp. 70–77, 2014.
- [13] A. M. Hamed and R. K. Rao, "Evaluation of capacity and power efficiency in millimeter-wave bands," in *Proceedings of the 2016 International Symposium on Performance Evaluation of Computer and Telecommunication Systems, SPECTS 2016*, Canada, July 2016.
- [14] W. Tan, P. J. Smith, H. A. Suraweera, M. Matthaiou, and S. Jin, "Spectral efficiency of multi-user mmwave systems with uniform linear arrays and MRT," in *Proceedings of the 83rd IEEE Vehicular Technology Conference, VTC Spring 2016*, China, May 2016.
- [15] T. A. Khan, A. Alkhateeb, and R. W. Heath, "Energy coverage in millimeter wave energy harvesting networks," in *Proceedings of the IEEE Globecom Workshops, GC Wkshps 2015*, USA, December 2015.
- [16] A. Mesodiakaki, F. Adelantado, A. Antonopoulos, L. Alonso, and C. Verikoukis, "Energy and spectrum efficient user association in 5G heterogeneous networks," in *Proceedings of the 27th IEEE Annual International Symposium on Personal, Indoor, and Mobile Radio Communications, PIMRC 2016*, Spain, September 2016.
- [17] Y. Chen, S. Zhang, S. Xu, and G. Y. Li, "Fundamental trade-offs on green wireless networks," *IEEE Communications Magazine*, vol. 49, no. 6, pp. 30–37, 2011.
- [18] T. Levanen, J. Pirskanen, and M. Valkama, "Radio interface design for ultra-low latency millimeter-wave communications in 5G Era," in *Proceedings of the 2014 IEEE Globecom Workshops, GC Wkshps 2014*, pp. 1420–1426, USA, December 2014.
- [19] Z. Wei, X. Zhu, S. Sun, Y. Huang, A. Al-Tahmeesschi, and Y. Jiang, "Energy-Efficiency of Millimeter-Wave Full-Duplex Relaying Systems: Challenges and Solutions," *IEEE Access*, vol. 4, pp. 4848–4860, 2016.
- [20] M. Steinbauer, A. F. Molisch, and E. Bonek, "The double-directional radio channel," *IEEE Antennas and Propagation Magazine*, vol. 43, no. 4, pp. 51–63, 2001.
- [21] C. E. Shannon, "A mathematical theory of communication," *Bibliometrics*, vol. 5, no. 1, pp. 3–55, 2001.
- [22] J. Choi, "Energy efficiency of a heterogeneous network using millimeter-wave small-cell base stations," in *Proceedings of the 26th IEEE Annual International Symposium on Personal, Indoor, and Mobile Radio Communications, PIMRC 2015*, pp. 293–297, China, September 2015.
- [23] A. M. Hamed and R. K. Rao, "Energy and spectral efficiency in cellular networks considering fading, path loss, and interference," in *Proceedings of the 30th IEEE Canadian Conference on Electrical and Computer Engineering, CCECE 2017*, Canada, May 2017.
- [24] H. Pervaiz, L. Musavian, and Q. Ni, "Area energy and area spectrum efficiency trade-off in 5G heterogeneous networks," in *Proceedings of the IEEE International Conference on Communication Workshop, ICCW 2015*, pp. 1178–1183, UK, June 2015.
- [25] M.-S. Alouini and A. J. Goldsmith, "Area spectral efficiency of cellular mobile radio systems," *IEEE Transactions on Vehicular Technology*, vol. 48, no. 4, pp. 1047–1066, 1999.
- [26] A. Mesodiakaki, F. Adelantado, L. Alonso, M. Di Renzo, and C. Verikoukis, "Energy-and Spectrum-Efficient User Association in Millimeter-Wave Backhaul Small-Cell Networks," *IEEE Transactions on Vehicular Technology*, vol. 66, no. 2, pp. 1810–1821, 2017.
- [27] J.-M. Gorce, R. Zhang, K. Jaffrès-Runser, and C. Goursaud, "Energy, latency and capacity trade-offs in wireless multi-hop networks," in *Proceedings of the 2010 IEEE 21st International Symposium on Personal Indoor and Mobile Radio Communications, PIMRC 2010*, pp. 2757–2762, Turkey, September 2010.

## Research Article

# Measurement Method of Temporal Attenuation by Human Body in Off-the-Shelf 60 GHz WLAN with HMM-Based Transmission State Estimation

Yusuke Koda , Koji Yamamoto , Takayuki Nishio , and Masahiro Morikura

*Graduate School of Informatics, Kyoto University, Yoshida-honmachi, Sakyo-ku, Kyoto 606-8501, Japan*

Correspondence should be addressed to Yusuke Koda; [koda@imc.cce.i.kyoto-u.ac.jp](mailto:koda@imc.cce.i.kyoto-u.ac.jp)

Received 28 September 2017; Revised 15 February 2018; Accepted 20 March 2018; Published 23 April 2018

Academic Editor: Ahmed M. Al-Samman

Copyright © 2018 Yusuke Koda et al. This is an open access article distributed under the Creative Commons Attribution License, which permits unrestricted use, distribution, and reproduction in any medium, provided the original work is properly cited.

This paper discusses a measurement method of time-variant attenuation of IEEE 802.11ad wireless LAN signals in the 60 GHz band induced by human blockage. The IEEE 802.11ad access point (AP) transmits frames intermittently, not continuously. Thus, to obtain the time-varying signal attenuation, it is required to estimate the duration in which the AP transmitted signals. To estimate whether the AP transmitted signals or not at each sampling point, this paper applies a simple two-state hidden Markov model. In addition, the validity of the model is tested based on Bayesian information criterion in order to prevent model overfitting and consequent invalid results. The measurement method is validated in that the distribution of the time duration in which the signal attenuates by 5 dB is consistent with the existing statistical model and the range of the measured time duration in which the signal attenuation decreases from 5 dB to 0 dB is similar to that in the previous report.

## 1. Introduction

A millimeter wave (mmWave) wireless LAN (WLAN) that leverages a channel bandwidth of over 2 GHz offers multi-gigabit data transfers, which attracts a lot of attention [1–4]. However, the mmWave WLAN experiences more signal attenuation induced by human blockage than WLANs that operate at the microwave band [5]. The attenuation is attributable to the use of higher directional antennas that are to compensate for a larger pass loss and to propagation characteristics of mmWave [6].

Many studies have suggested that communication devices perform a reactive action to respond to the human blockage [2, 7–9]. For example, the beam steering is an effective technique to overcome human blockage [2]. When the signal degradation is detected, the beam is switched at the direction in which a communication link utilizing reflected path without human blockage can be established. The authors in [8] proposed a multiband WLAN where a mmWave WLAN cooperates with a WLAN that operates at the 5 GHz band. They proposed changing the operating frequency to 5 GHz and thereby recovering the link quality when the human blockage is detected in the mmWave WLAN.

These reactive actions should be performed before the signal attenuates by an unacceptable threshold level. For example, when the signal attenuates by 5 dB, the physical layer (PHY) data rate is decreased by up to 2 Gbit/s [10], which can be a crucial problem for services that require high data rate. To do this, the period of monitoring received signal strength is to be smaller than the time span in which the signal attenuates by the threshold. In order to determine an appropriate period of the monitoring, characteristics of time-variant signal attenuation in the mmWave band induced by human bodies should be fully investigated.

The measurement of the time-variant signal attenuation in the millimeter wave band has been conducted in many studies [6, 11–17]. The authors in [13] measured the attenuation in the 60 GHz band and then compared the results with a knife edge diffraction model where the human body is modeled by two cylinders. The authors in [11] measured statistical characteristics of the time duration in which the signal attenuates by 5 dB, the time duration in which the signal attenuation level recovers from 5 dB to 0 dB, and time duration in which the human blockage event continues. From these parameters, they built a piecewise linear model for the time series of the signal attenuation in 60 GHz.

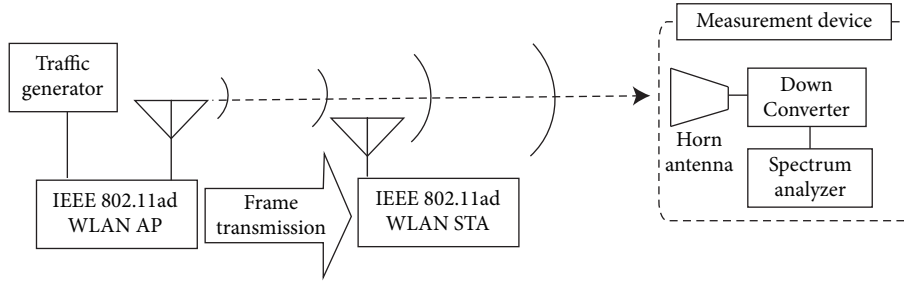


FIGURE 1: Block diagram of measurement system.

These measurements generally have employed horn antennas in a transmitter, while transmitters in mmWave WLANs employ consumer-grade array antennas to perform beamforming [4]. The authors in [5] revealed a significant difference between these two types of antennas in terms of directivity and side lobes. The difference between two types of antennas might give rise to the gap between the measurement results because antenna pattern of the transmitters gives an impact on the time series of signal attenuation [16]. For practical operation of mmWave WLANs, the gap should be investigated using a commercially available IEEE 802.11ad WLAN access point (AP) as a transmitter.

Being different from many measurements above where transmitters transmit continuous waves to receivers, the measurement of signals transmitted by an IEEE 802.11ad WLAN AP requires the estimation of whether the AP transmits signals or not at each sampling point in a sweep. This is due to the transmission mechanism of the AP. The AP transmits signals intermittently to a station (STA) according to medium access control (MAC) protocols [10]. The durations in which the AP transmits a signal might be smaller than a sweep length; hence, in each sweep length, there exist both durations in which the AP transmitted signals and durations in which the AP did not. Thus, in order to temporally track the signal attenuation due to human blockage, it is required to classify the samples into samples in the former durations and samples in the later durations.

In order to classify time-dependent variables, hidden Markov models (HMMs) are widely used in cognitive radio networks [18, 19]. The HMMs allow us to consider dependence between classes of subsequent values; thus, many studies have applied the HMM to the classification of time-dependent variables, in which there often exists dependence between subsequent values. In [18], the authors presented the method to estimate whether the interference signals exist or not in each time slot from overall samples in each slot. These studies have assumed that whether interference signals exist in each sample or not is identical in each time slot. This assumption is reasonable for time division multiple access, where the transmission time is slotted, and whether interference signals exist or not is identical in each time slot. However, the same way is not applicable to estimate whether WLAN signals exist or not in obtained samples because the transmission in WLANs is not slotted and in a sweep length there might exist both durations when the signals are present and those when the signals are absent.

In this paper, we conduct a measurement of time-varying signal attenuation induced by human blockage, involving a commercially available IEEE 802.11ad WLAN AP and STA. We present the estimation of whether signal is present or not at each sampling point using a simple two-state hidden Markov model. Being different from above-mentioned studies, we estimate classes, that is, signal presence or absence of *each* sample, not those of *overall* samples in a sweep length.

The contributions of this paper are threefold:

- (i) In order to estimate whether the AP transmitted frames or not at each sampling point, we apply a simple two-state HMM.
- (ii) Applying a two-state HMM to data obtained when the AP does not transmit any signals causes model overfitting and consequent invalid power calculation. Thus, we perform Bayesian information criterion-(BIC-) based model selection, where we select which two-state HMM or one-state model is more applicable to obtained data. We thereby detect this kind of the data and prevent model overfitting.
- (iii) Our measurements are validated in that the statistical characteristics of the duration in which the signal attenuates by 5 dB are consistent with the statistical model built in a previous report, and the range of the duration in which the signal attenuation decreases from 5 dB to 0 dB is similar to that in the report.

The rest of this paper is organized as follows. Section 2 presents the architecture of our measurement system in detail. Section 3 presents the method to obtain the time-varying attenuation, involving an estimation of whether the AP transmitted a frame or not using HMM. Section 4 shows the measurement results. Section 5 concludes the paper.

## 2. Measurement Setup

Figure 1 shows the measurement system. The horn antenna receives radio frequency (RF) signals at 60.48 GHz, where the antenna is affixed to a waveguide flange input on the down converter. Then, the down converter converts the RF signal to a baseband signal. The microwave spectrum analyzer filters I-channel components of the baseband signal at the center frequency of 100 MHz with a bandwidth of 10 MHz. These signals are then sampled by an A/D converter in a spectrum analyzer. Figures 2 and 3 show pictures of the measurement

TABLE 1: Measurement equipment.

IEEE 802.11ad WLAN AP	Dell Wireless Dock D5000
IEEE 802.11ad WLAN STA	Dell Latitude E5540
Client laptop	Dell Latitude E5540
Wired network	1000BASE-T Gigabit Ethernet
Microwave spectrum analyzer	Tektronix RSA306
Down converter	Sivers IMA FC2221V
Antenna	Sivers IMA Horn antenna, 24 dBi

TABLE 2: Measurement parameters.

Channel	60.48 GHz
Sampling frequency $1/T$	14 MHz
Receiver antenna gain	24 dBi
Acquisition bandwidth	10 MHz
Number of samples per sampling $K$	2800

system and the measurement device, respectively. Details regarding the measurement equipment and the measurement parameters are shown in Tables 1 and 2, respectively.

Note that the choice of the bandwidth, which is smaller than the IEEE 802.11ad WLAN channels, is attributed to the time resolution in which we obtain the signal attenuation. In order to show the consistency in the time duration in which signal attenuates by 5 dB and thereby to validate our measurement method, the time resolution of tens of ms is required (the time duration is reported to have the value of tens of ms in [11]). Because there is a tradeoff between the acquisition bandwidth and the time resolution (a wider acquisition bandwidth sacrifices the time resolution), we conduct the measurement in a smaller bandwidth than the IEEE 802.11ad WLAN channel bandwidth. In our measurement system, the measurement bandwidth of 10 MHz allowed us to obtain the temporal signal attenuation in a time resolution of around 20 ms.

The measurement was conducted under the condition that the AP transmits data frames to the STA as shown in Figure 1. The frame transmission was done by generating uplink traffic from the laptop connected to the AP with a gigabit Ethernet cable. The traffic was generated by Iperf3 [20].

For the sake of clarity of the discussion in the following sections, we show the signal representation. Let  $r(t)$  be the representation of I-channel components of the 11ad WLAN signal converted by the down converter and let  $b(t)$  be the impulse response of the acquisition band-pass filter in the spectrum analyzer. Then, the signal that is to be sampled by the A/D converter in the spectrum analyzer is represented by  $y(t) = (r(t) + n(t)) * b(t)$ , where  $n(t)$  is the noise inherent in the measurement device and  $*$  represents the convolution of two functions. Note that  $r(t)$  is equivalent to 0 when the AP does not transmit any frames.

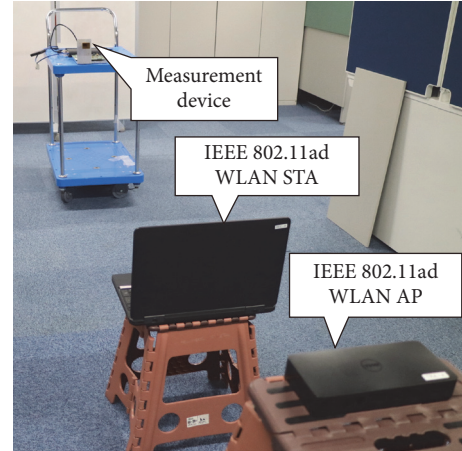


FIGURE 2: Measurement system.

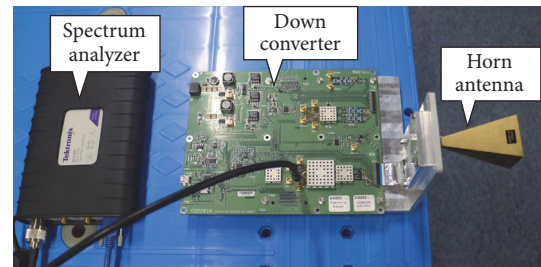


FIGURE 3: Measurement device.

### 3. Measurement Method of Temporal Signal Attenuation

**3.1. Overview.** Let the vector that identifies whether the AP transmits frames or not be denoted by  $\mathbf{z}(t) = (z_0(t), z_1(t))^T$ , which is defined as

$$\mathbf{z}(t) := \begin{cases} (0, 1)^T & \text{if the AP transmits a frame,} \\ (1, 0)^T & \text{otherwise.} \end{cases} \quad (1)$$

Let  $\mathcal{D}$  be the union of disjoint time intervals when the AP transmits frames, defined as

$$\mathcal{D} := \{t \mid z_1(t) = 1\}. \quad (2)$$

Let  $\mathcal{D}(t_m) := \mathcal{D} \cap [t_m, t_m + KT]$  be the time duration when the AP transmitted frames in the sampling window  $[t_m, t_m + KT]$ , where  $t_m$  denotes the time at which the analyzer starts the  $m$ th sweep, while  $K$  and  $T$  denote the number of samples and the sampling period, respectively; therefore,  $t_m + KT$  denotes the time at which the analyzer ends the sweep. The timing of sweeps is depicted in Figure 4. Note that the time length  $KT$  for which the analyzer sweeps (it is  $200 \mu\text{s}$  in the measurements) is shorter than the interval  $t_{m+1} - t_m$  between successive sweeps (it is 20 ms).

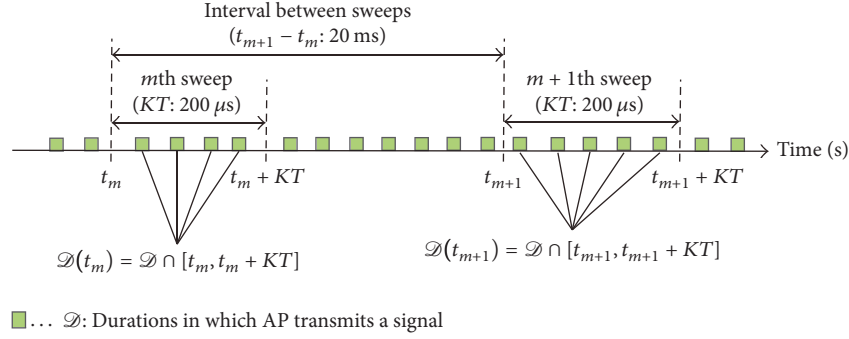


FIGURE 4: Timing of sweeps.

Our goal is to obtain the time-dependent attenuation value  $A(t_m)$  given by

$$A(t_m) = \frac{P(t_m)}{P(t_1)}, \quad (3)$$

where  $P(t_m)$  is the mean power of the measured signal, given by

$$P(t_m) = \frac{\int_{D(t_m)} |y(t)|^2 dt}{\int_{D(t_m)} dt}, \quad (4)$$

that is, the mean value of the power samples  $p_m[k_m] := |y(t_m + k_m T)|^2$  for  $k_m \in \{1, \dots, K\}$  taken only if  $z_1(t_m + k_m T) = 1$ .  $P(t_m)$  for  $m > 1$  is obtained in the possible presence of human bodies, while  $P(t_1)$  is obtained in the absence of human bodies and is the reference used to compute the attenuation  $A(t_m)$ .

We calculate  $A(t_m)$  by three steps: the BIC-based model selection, the HMM-based frame transmission state estimation, and averaging. First, BIC-based model selection decides which of a two-state HMM and a one-state model is more appropriate to be applied to the obtained data  $\mathbf{p}_m = (p_m[1], \dots, p_m[K])^T$ . Only when the two-state HMM is selected is the HMM-based frame transmission state estimation conducted. Then, we estimate whether  $z_1(t_m + k_m T) = 1$  or not for  $k_m \in \{1, \dots, K\}$ , that is, whether the AP transmitted frames or not at each sampling point. Finally, we calculate the average of  $p_m[k_m]$  for  $k_m$  which is estimated to be  $z_1(t_m + k_m T) = 1$ .

### 3.2. HMM-Based Frame Transmission State Estimation

**3.2.1. HMM-Based Estimation Scheme.** Let  $\mathbf{z}_m[k_m] = (z_{m,0}[k_m], z_{m,1}[k_m])^T$  denote  $\mathbf{z}(t_m + k_m T)$ . The main purpose of this subsection is to decide whether  $z_{m,1}[k_m] = 1$  or not for  $k_m \in \{1, \dots, K\}$ . The decision is based on modeling the power observations  $p_m[k_m]$  using a two-state HMM. We now consider that the two-state HMM is selected in the BIC-based model selection in advance. The model selection is discussed in Section 3.3.

An HMM is a statistical model that forms a sequence of observations whose distribution depends on a latent variable

that follows a Markov chain. We now consider  $\mathbf{z}_m[k_m]$  as the latent variable on which the distribution of  $p_m[k_m]$  depends. We refer to the phenomenon that  $z_{m,1}[k_m] = 1$  as *frame transmission state*; the phenomenon that  $z_{m,1}[k_m] = 0$  is considered as *pausing state*. We assume that the distribution conditioned on  $\mathbf{z}_m[k_m]$  is an exponential distribution; thus, the probability density functions of  $p_m[k_m]$  conditioned on  $\mathbf{z}_m[k_m]$  are given as follows:

$$\begin{aligned} p(p_m[k_m] | z_{m,0}[k_m] = 1) &= \lambda_0 \exp(-\lambda_0 p_m[k_m]), \\ p(p_m[k_m] | z_{m,1}[k_m] = 1) &= \lambda_1 \exp(-\lambda_1 p_m[k_m]), \end{aligned} \quad (5)$$

where  $\lambda_i$  for  $i \in \{0, 1\}$  denotes the parameter of the exponential distribution when  $z_{m,i}[k_m] = 1$ . The assumption is validated by the experimental results.

We estimate the most likely sequence of the latent variables utilizing Viterbi algorithm. Viterbi algorithm requires the parameters of the HMM which include  $\lambda_i$ , transition probabilities, and initial state probabilities. Because of the lack of the knowledge of the true parameters, we estimate the most likely parameters using expectation maximization (EM) algorithm. Each algorithm is described in detail as follows.

**3.2.2. Parameter Estimation.** We estimate the parameters of the HMM given by  $\boldsymbol{\theta} = (\lambda_0, \lambda_1, q_{0,0}, q_{0,1}, q_{1,0}, q_{1,1}, \pi_0, \pi_1)^T$ , where  $q_{i,j}$  for  $i \in \{0, 1\}$  and  $j \in \{0, 1\}$  represents the transition probability of a latent variable that is defined as  $\mathbb{P}(z_{m,j}[k_m + 1] = 1 | z_{m,i}[k_m] = 1)$ ;  $\pi_i$  represents the initial state probability that is defined as  $\mathbb{P}(z_{m,i}[1] = 1)$ .

The estimation utilizes EM algorithm [21]. The EM algorithm derives the estimator  $\hat{\boldsymbol{\theta}}$  maximizing a likelihood  $p(\mathbf{p}_m | \boldsymbol{\theta})$  via the iteration of E-step and M-step. The E-step derives the expectation of  $\ln p(\mathbf{p}_m, \mathbf{Z}_m | \boldsymbol{\theta})$  under the posterior distribution of  $\mathbf{Z}_m := (\mathbf{z}_m[1], \dots, \mathbf{z}_m[K])$  and a current estimator:

$$\boldsymbol{\theta}^{(n)} = (\lambda_0^{(n)}, \lambda_1^{(n)}, q_{0,0}^{(n)}, q_{0,1}^{(n)}, q_{1,0}^{(n)}, q_{1,1}^{(n)}, \pi_0^{(n)}, \pi_1^{(n)})^T, \quad (6)$$

where  $n$  is an iteration number. The M-step derives the estimator:

$$\begin{aligned} \boldsymbol{\theta}^{(n+1)} &= (\lambda_0^{(n+1)}, \lambda_1^{(n+1)}, q_{0,0}^{(n+1)}, q_{0,1}^{(n+1)}, q_{1,0}^{(n+1)}, q_{1,1}^{(n+1)}, \pi_0^{(n+1)}, \\ &\pi_1^{(n+1)})^T, \end{aligned} \quad (7)$$

which maximizes the expectation. Details of each step are described later. The iteration is guaranteed to converge to the locally optimal estimator  $\hat{\boldsymbol{\theta}}$  [21].

The goal of the E-step is to derive the expectation of  $\ln p(\mathbf{p}_m, \mathbf{Z}_m | \boldsymbol{\theta})$  under the posterior distribution of  $\mathbf{Z}_m$  given  $\mathbf{p}_m$  and the current estimator  $\boldsymbol{\theta}^{(n)}$ . Consider the expectation  $Q(\boldsymbol{\theta}, \boldsymbol{\theta}^{(n)})$ , which is described as follows:

$$\begin{aligned} Q(\boldsymbol{\theta}, \boldsymbol{\theta}^{(n)}) &:= \mathbb{E}_{\mathbf{Z}_m} [\ln p(\mathbf{p}_m, \mathbf{Z}_m | \boldsymbol{\theta}) | \mathbf{p}_m, \boldsymbol{\theta}^{(n)}] \\ &= \sum_{\mathbf{Z}_m} p(\mathbf{Z}_m | \mathbf{p}_m, \boldsymbol{\theta}^{(n)}) \ln p(\mathbf{p}_m, \mathbf{Z}_m | \boldsymbol{\theta}). \end{aligned} \quad (8)$$

As in [21], the expectation is given as follows:

$$\begin{aligned} Q(\boldsymbol{\theta}, \boldsymbol{\theta}^{(n)}) &= \sum_{i=0}^1 \gamma(z_{m,i} [1]) \ln \pi_i \\ &+ \sum_{k_m=2}^K \sum_{j=0}^1 \sum_{i=0}^1 \xi(z_{m,j} [k_m - 1], z_{m,i} [k_m]) \ln q_{j,i} \quad (9) \\ &+ \sum_{k_m=1}^K \sum_{i=0}^1 \gamma(z_{m,i} [k_m]) \\ &\cdot \ln p(p_m [k_m] | z_{m,i} [k_m] = 1, \boldsymbol{\theta}^{(n)}), \end{aligned}$$

where

$$\begin{aligned} \gamma(z_{m,i} [k_m]) &:= \mathbb{E}_{\mathbf{z}_m[k_m]} [z_{m,i} [k_m] | \mathbf{p}_m, \boldsymbol{\theta}^{(n)}] \\ &= \sum_{\mathbf{z}_m[k_m]} z_{m,i} [k_m] p(\mathbf{z}_m [k_m] | \mathbf{p}_m, \boldsymbol{\theta}^{(n)}), \\ \xi(z_{m,j} [k_m - 1], z_{m,i} [k_m]) & \\ &:= \mathbb{E}_{\mathbf{z}_m[k], \mathbf{z}_m[k-1]} [z_{m,j} [k_m - 1] z_{m,i} [k] | \mathbf{p}_m, \boldsymbol{\theta}^{(n)}] \quad (10) \\ &= \sum_{\mathbf{z}_m[k_m-1]} \sum_{\mathbf{z}_m[k_m]} z_{m,j} [k_m - 1] z_{m,i} [k_m] \\ &\cdot p(\mathbf{z}_m [k_m - 1], \mathbf{z}_m [k_m] | \mathbf{p}_m, \boldsymbol{\theta}^{(n)}). \end{aligned}$$

These expectations,  $\gamma(z_{m,i} [k_m])$  and  $\xi(z_{m,j} [k_m - 1], z_{m,i} [k_m])$ , are derived via the forward-backward algorithm [21].

The M-step derives the revised estimator  $\boldsymbol{\theta}^{(n+1)}$  that maximizes  $Q(\boldsymbol{\theta}, \boldsymbol{\theta}^{(n)})$ , which satisfies

$$\boldsymbol{\theta}^{(n+1)} = \arg \max_{\boldsymbol{\theta}} Q(\boldsymbol{\theta}, \boldsymbol{\theta}^{(n)}). \quad (11)$$

The maximization with respect to  $\pi_i, q_{i,j} \forall i, j$  is achieved using appropriate Lagrange multipliers with the results [21]:

$$\begin{aligned} \pi_i^{(n+1)} &= \frac{\gamma(z_{m,i} [1])}{\sum_{j=0}^1 \gamma(z_{m,j} [1])}, \\ q_{j,i}^{(n+1)} &= \frac{\sum_{k_m=2}^K \xi(z_{m,j} [k_m - 1], z_{m,i} [k_m])}{\sum_{i=0}^1 \sum_{k_m=2}^K \xi(z_{m,j} [k_m - 1], z_{m,i} [k_m])}. \end{aligned} \quad (12)$$

The maximization with respect to  $\lambda_i, \forall i$ , is achieved via partial derivative with respect to  $\lambda_i$ , which results in

$$\lambda_i^{(n+1)} = \frac{\sum_{k_m=1}^K \gamma(z_{m,i} [k_m])}{\sum_{k_m=1}^K p_m [k_m] \gamma(z_{m,i} [k_m])}. \quad (13)$$

These steps are iterated until the convergence condition,  $|Q(\boldsymbol{\theta}^{(n+1)}, \boldsymbol{\theta}^{(n)}) - Q(\boldsymbol{\theta}^{(n)}, \boldsymbol{\theta}^{(n-1)})| < \epsilon_0$ , is satisfied, where  $\epsilon_0$  is the predefined tolerance. We set the tolerance to be  $10^{-2}$ , which is much smaller than the likelihoods that have a value of the order of  $10^5$  in these experiments.

**3.2.3. Estimation of a Sequence of Latent Variables.** The goal to estimate the most likely sequence of latent variables is achieved via Viterbi algorithm. Viterbi algorithm seeks for the sequence of latent variables  $\hat{\mathbf{Z}}_m$ , which is described as

$$\hat{\mathbf{Z}}_m = \arg \max_{\mathbf{Z}_m} p(\mathbf{p}_m, \mathbf{Z}_m | \hat{\boldsymbol{\theta}}). \quad (14)$$

Viterbi algorithm in the HMM works as maximum likelihood detection of convolutional codes [22]. Consider the trellis diagram, where, for all values  $k_m$ , all possible latent variables in the  $k_m$ th sampling point are deployed as the nodes at the trellis depth  $k_m$  and all the nodes at the trellis depth  $k_m$  are connected to all the nodes at the trellis depth  $k_m + 1$ .  $\hat{\mathbf{Z}}_m = (\hat{z}_m[1], \dots, \hat{z}_m[K])$  is achieved by seeking for the trellis path maximizing path metric, defining the branch metric from the  $(i+1)$ th node at the depth  $k_m$  to the  $(j+1)$ th node at the depth  $k_m + 1$ ,  $B_{k_m}^{(i \rightarrow j)}$ , as follows:

$$\begin{aligned} B_{k_m}^{(i \rightarrow j)} &= \ln \{ p(\mathbf{z}_{m,j} [k_m + 1] = 1 | \mathbf{z}_{m,i} [k_m] = 1, \hat{\boldsymbol{\theta}}) \\ &\cdot p(p_m [k_m + 1] | \mathbf{z}_{m,j} [k_m + 1] = 1, \hat{\boldsymbol{\theta}}) \}. \end{aligned} \quad (15)$$

**3.2.4. Model Verification.** We show that Viterbi algorithm can estimate latent variables in each sampling point. Using the results, we validate the assumption that  $p_m[k_m]$  in each state follows the exponential distribution.

Figure 5 shows an example of the estimation of latent variables. This shows that each latent variable is consecutive for a certain duration. This result agrees with the fact that the AP transmits a frame in a certain duration: from the start of transmission to the end.

Figure 6 shows the cumulative frequencies of  $p_m[k_m]$  in each estimated state and theoretical cumulative distribution function (CDF) of each exponential distribution. The parameters of each exponential distribution are estimated via EM algorithm. This figure shows that the distribution of  $p_m[k_m]$  in each state coincides with the theoretical CDF, which also shows the validity of the assumption that  $p_m[k_m]$  in each state follows the exponential distribution.

**3.3. BIC-Based Model Selection.** In the previous subsection, we considered that fitting the data using a two-state model is more appropriate than using a one-state model. However, there exist data in which no frames are observed because the AP did not transmit any frames for the time duration

```

input: power observations  $\mathbf{P} = (\mathbf{p}_1, \dots, \mathbf{p}_M)$ 
output: time series of signal attenuation  $(A(t_1), \dots, A(t_M))^T$ 
(1) for  $m \in \{1, \dots, M\}$  do
(2)   conduct maximum likelihood estimation of a one-state exponential distribution model and calculate BIC,  $\text{BIC}_1$ 
(3)   conduct EM algorithm in a two-state HMM and compute BIC,  $\text{BIC}_2$ 
(4)   if  $\text{BIC}_2 < \text{BIC}_1$  then
(5)     estimation of the maximum-likely latent variables  $\hat{\mathbf{Z}}_m$  using Viterbi algorithm
(6)      $P_m \leftarrow$  average of  $p_m[k_m]$  for  $\forall k_m \in \{k \in \{1, \dots, K\} \mid \hat{z}_{m,1}[k] = 1\}$ 
(7)      $A(t_m) \leftarrow P_m/P_1$ 
(8)   end if
(9) end for

```

ALGORITHM 1: Procedure for measuring temporal signal attenuation in mmWave WLAN.

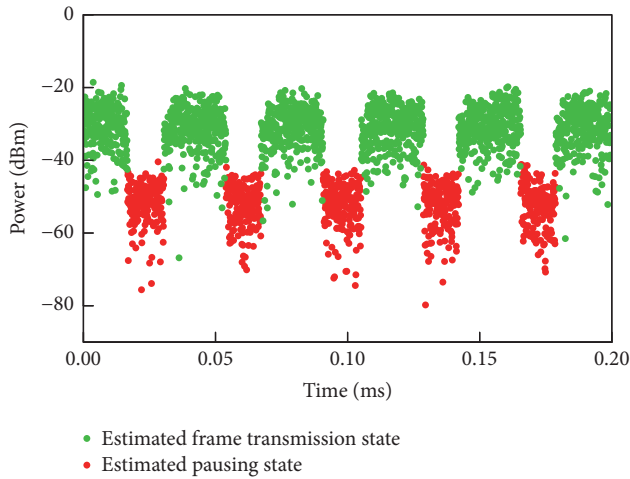


FIGURE 5: Example of the estimate of whether the AP transmitted frames or not.

of  $[t_m, t_m + KT]$  (as an alternative approach, we can set the sampling rate and the number of samples per sweep so that at least one beacon signal is received. Note that the beacon interval of the AP we employed is 1.1 ms [11]). In this case, applying a one-state model, where  $p_m[k_m]$  follows an identical exponential distribution, is more appropriate because applying a two-state model causes model overfitting and consequent invalid calculation of  $A(t_m)$ . If a two-state HMM is applied in this case, there exists  $k_m \in \{1, \dots, K\}$  for which  $\hat{z}_{m,1}[k] = 1$  although the truth is that  $\hat{z}_{m,1}[k_m] = 0 \forall k_m \in \{1, \dots, K\}$ . Thus, it is required that which model to be appropriate is decided and that if the one-state model is estimated to be appropriate, we decide that we do not calculate  $A(t_m)$ .

To decide which model to be appropriate, we utilize BIC [21]. BIC is given as follows:

$$\text{BIC} = -L(\hat{\theta}) + \frac{d}{2} \ln K, \quad (16)$$

where  $L(\cdot)$  denotes the log-likelihood function and  $d$  is the number of parameters that are required to describe each model. In the two-state HMM,  $d = 5$ ; that is, the parameters are  $\lambda_0, \lambda_1, q_{0,0}, q_{1,0},$  and  $\pi_0$ . Note that  $q_{0,1}, q_{1,1},$

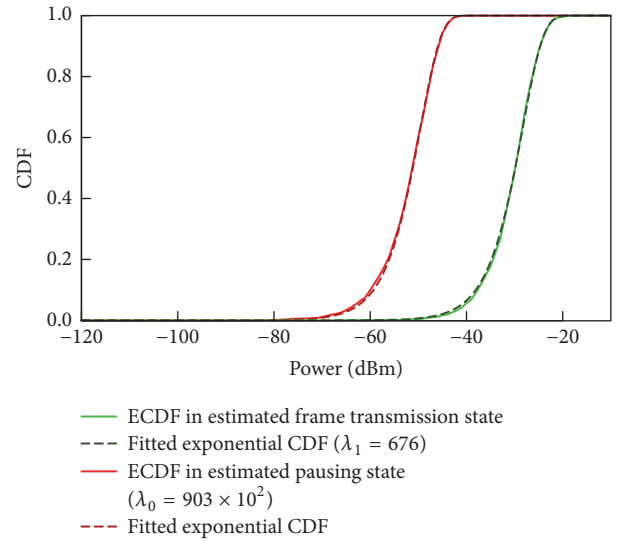


FIGURE 6: Cumulative frequencies of power observations in each state and CDF of fitted exponential distributions.

and  $\pi_1$  are not counted because these parameters are decided deterministically from  $q_{0,0}, q_{1,0},$  and  $\pi_0$ , respectively. In the one-state model,  $d = 1$ .  $\hat{\theta}$  is the vector containing the model parameters with maximum likelihood. The model whose BIC is smaller than that of the counterpart is applied.

The second term of BIC is interpreted to be the penalty of increasing the number of model parameters. The penalty of BIC is more than that of Akaike information criterion (AIC) [23], which is a reason why we adopt BIC. BIC tends not to select the two-state model that has more parameters and therefore prevents from model overfitting.

#### 3.4. Procedure of Calculating Time-Varying Signal Attenuation.

We summarized the procedure of the calculation of  $A(t_m)$  in Algorithm 1. First, we compute BIC of each model. BIC of the one-state exponential distribution model,  $\text{BIC}_1$ , is calculated via maximum likelihood estimation; that of the two-state HMM,  $\text{BIC}_2$ , is calculated via EM algorithm. If  $\text{BIC}_2 < \text{BIC}_1$ , Viterbi algorithm is conducted to estimate the latent variables and then  $A(t_m)$  is calculated by averaging  $p_m[k]$  in frame

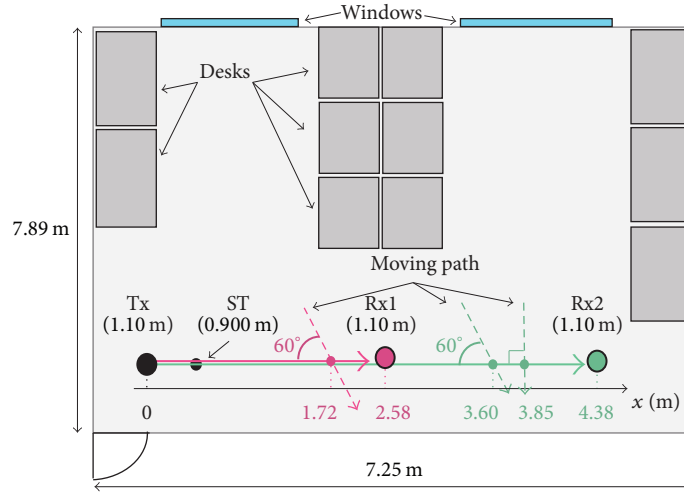


FIGURE 7: Top view of measurement environment with the moving path and positions of the AP, STA, and measurement device, denoted by TX, ST, and RX1 or RX2, respectively. Values in parentheses indicate the height of each device.

transmission state. If not, it is decided that the calculation of  $A(t_m)$  is not conducted because the AP did not transmit any frames.

#### 4. Measurement of Time-Varying Attenuation in IEEE 802.11ad WLAN

**4.1. Objective.** The main objective of the measurements is to validate the measurement method by demonstrating the consistency in quantities associated with the signal attenuation under a similar condition to that in the previous report [11]; additional measurements in other conditions are out of the scope of this paper. As in [11], we measured the duration  $t_{\text{decay},5\text{ dB}}$  in which signal attenuation level increases from 0 dB to 5 dB, the duration  $t_{\text{rise},5\text{ dB}}$  in which signal attenuation level decreases from 5 dB to 0 dB, and the mean signal attenuation  $A_{\text{mean}}$  in the interval  $[t_b + (t_e - t_b)/3, t_e - (t_e - t_b)/3]$ , where  $t_b$  and  $t_e$  represent, respectively, the last zero crossing time before a shadowing event and the first zero crossing time after the shadowing event.

**4.2. Experiment Description.** The measurements were conducted in a similar experimental scenario to the previous report [11] in order to compare our results with the results in the report. The moving paths of the pedestrian were kept fixed as in Figure 7, which are similar moving paths to those in the report.

Figure 7 also depicts the deployment of the measurement equipment. The AP and STA were kept fixed at the positions TX and ST, whereas the measurement device was placed at the positions RX1 and RX2. The separation distances between TX and RX1 and between TX and RX2 were 2.58 m and 4.38 m, respectively. The height of the AP and the measurement device was 1.10 m; that of the STA was 0.90 m.

**4.3. Experimental Results.** Figure 8 shows an example of the time series of measured signal attenuation induced by human blockage. The signal attenuation level oscillates by up to 2 dB

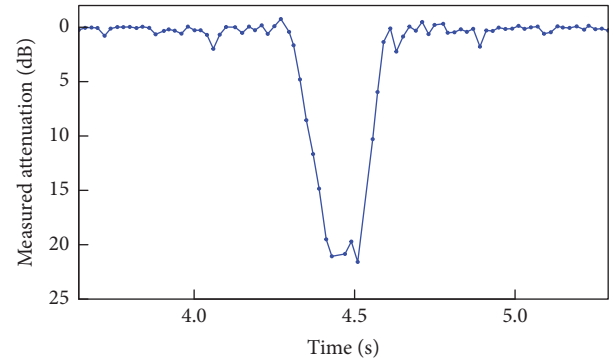


FIGURE 8: Time series of measured attenuation of signal transmitted by IEEE 802.11ad AP induced by human blockage.

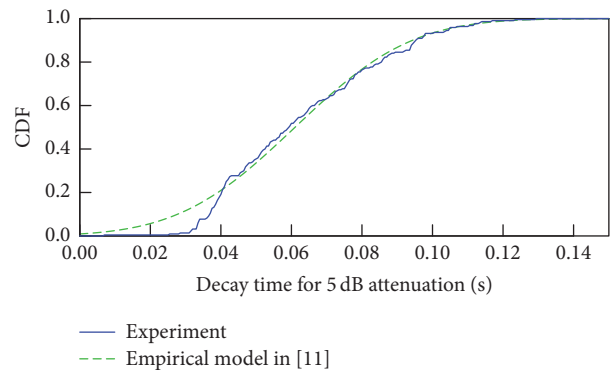


FIGURE 9: CDF of decay time for 5 dB attenuation,  $t_{\text{decay},5\text{ dB}}$ .

before and after the signal attenuates. This is in agreement with a knife edge diffraction theory [24].

Figure 9 shows the CDF of the decay time  $t_{\text{decay},5\text{ dB}}$ . The empirical model in [11] is the Gaussian distribution with the mean of 0.061 s and the standard deviation of 0.026 s.

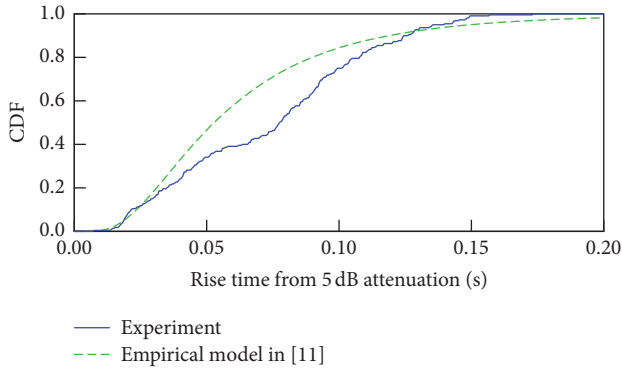


FIGURE 10: CDF of rise time from 5 dB attenuation,  $t_{\text{rise},5 \text{ dB}}$ .

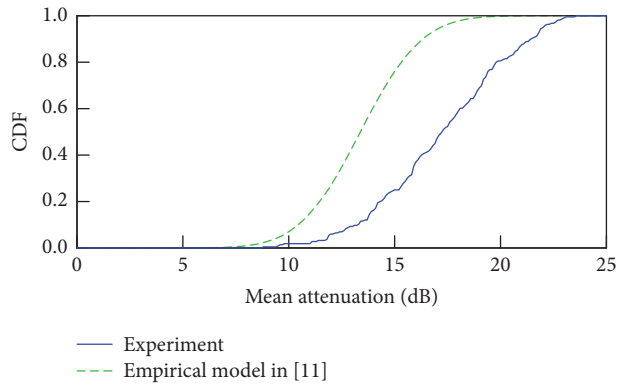


FIGURE 11: CDF of mean signal attenuation while pedestrian is blocking the LOS path,  $A_{\text{mean}}$ .

The measured cumulative frequency of  $t_{\text{decay},5 \text{ dB}}$  coincides with the model. In fact, the model cannot be rejected by the Kolmogorov-Smirnov test [25] with a significance level of 1%. Thus, in terms of the decay time  $t_{\text{decay},5 \text{ dB}}$ , the empirical model is valid for the IEEE 802.11ad WLAN signals transmitted by a commercially available AP with a consumer-grade array antenna as well as ones transmitted by a transmitter with a horn antenna.

Figure 10 shows the CDF of the rise time  $t_{\text{rise}}$ . The empirical model in [11] is the log-normal distribution with the log mean of  $-2.94$  and the log standard deviation of  $0.63$ . We can see that although there is a difference in the shape of the CDF, our results are consistent with the empirical model in that the rise time ranges from  $0.02 \text{ s}$  to  $0.15 \text{ s}$ .

Figure 11 shows the CDF of the mean signal attenuation  $A_{\text{mean}}$ . The empirical model in [11] is the Gaussian distribution with the mean of  $13 \text{ dB}$  and the standard deviation of  $2.0 \text{ dB}$ . This result shows that the signal in IEEE 802.11ad WLAN attenuates about  $4.0 \text{ dB}$  more than the signal in [11]. These differences might be attributable to the difference between the transmit antennas: the horn antenna employed in the report and the array antenna packed in the AP and the position at which the pedestrian crossed the LOS path (the report in [15] demonstrated that blockage at nearer positions to the receiver causes the higher signal attenuation in directional communications).

## 5. Conclusion

This paper discussed a measurement method of time-varying attenuation of signals transmitted by a commercially available IEEE 802.11ad WLAN AP caused by human blockage. We applied a two-state HMM in order to estimate whether the AP transmitted signals or not in each sampling point. We also presented the BIC-based model selection that decides which of one-state model and two-state model is to be applied. The two-state HMM-based estimation showed the valid results: both the sampling points estimated to be in frame transmission state and those estimated to be in pausing state are consecutive for a certain duration, which is consistent with a transmission mechanism of IEEE 802.11ad WLAN APs. The measurements are validated in that the measured time-varying signal attenuation is in an agreement with knife edge diffraction theory. The measurements are also validated in that the statistical characteristics of the duration in which the signal transmitted by the AP attenuates by  $5 \text{ dB}$  were consistent with the existing statistical model. On the other hand, the measurement results are different from the existing report in terms of the mean attenuation while a human is blocking a LOS path.

## Disclosure

This paper was presented in part at IEEE 86th Vehicular Technology Conference (VTC2017-Fall) [26].

## Conflicts of Interest

The authors declare that they have no conflicts of interest.

## Acknowledgments

The authors would like to thank Dr. Katsuyuki Haneda at Aalto University for his advice. This work was supported in part by JSPS KAKENHI (Grant no. JP17H03266) and by KDDI Foundation.

## References

- [1] E. Perahia and M. X. Gong, "Gigabit wireless LANs," *ACM SIGMOBILE Mobile Computing and Communications Review*, vol. 15, no. 3, p. 23, 2011.
- [2] X. Tie, K. Ramachandran, and R. Mahindra, "On 60 GHz wireless link performance in indoor environments," *Lecture Notes in Computer Science (including subseries Lecture Notes in Artificial Intelligence and Lecture Notes in Bioinformatics): Preface*, vol. 7192, pp. 147–157, 2012.
- [3] K. Haneda, "Channel models and beamforming at millimeter-wave frequency bands," *IEICE Transactions on Communications*, vol. E98B, no. 5, pp. 755–772, 2015.
- [4] K. Sakaguchi, E. M. Mohamed, H. Kusano et al., "Millimeter-wave wireless LAN and its extension toward 5G heterogeneous networks," *IEICE Transactions on Communications*, vol. E98B, no. 10, pp. 1932–1948, 2015.
- [5] T. Nitsche, G. Bielsa, I. Tejado, A. Loch, and J. Widmer, "Boon and bane of 60 GHz networks: Practical insights into beamforming, interference, and frame level operation," in *Proceedings*

- of the 11th ACM Conference on Emerging Networking Experiments and Technologies, CoNEXT 2015, Germany, December 2015.
- [6] S. Collonge, G. Zaharia, and G. El Zein, "Influence of the human activity on wide-band characteristics of the 60 GHz indoor radio channel," *IEEE Transactions on Wireless Communications*, vol. 3, no. 6, pp. 2396–2406, 2004.
- [7] Y. Oguma, T. Nishio, K. Yamamoto, and M. Morikura, "Implementation and evaluation of reactive base station selection for human blockage in mmWave communications," in *Proceedings of the 21st Asia-Pacific Conference on Communications, APCC 2015*, pp. 199–203, Kyoto, Japan, October 2015.
- [8] M. Umehira, G. Saito, S. Wada, S. Takeda, T. Miyajima, and K. Kagoshima, "Feasibility of RSSI based access network detection for multi-band WLAN using 2.4/5GHz and 60GHz," in *Proceedings of the 2014 International Symposium on Wireless Personal Multimedia Communications, WPMC 2014*, pp. 243–248, Sydney, Australia, September 2014.
- [9] Y. M. Tsang and A. S. Y. Poon, "Detecting human blockage and device movement in mmwave communication system," in *Proceedings of the 54th Annual IEEE Global Telecommunications Conference: "Energizing Global Communications", GLOBECOM 2011*, Houston, USA, December 2011.
- [10] "Wireless LAN medium access control (MAC) and physical layer (PHY) specification, IEEE Std. 802.11ad-2012".
- [11] M. Jacob, C. Mbianke, and T. Kürner, "A dynamic 60 GHz radio channel model for system level simulations with MAC protocols for IEEE 802.11ad," in *Proceedings of the 14th IEEE International Symposium on Consumer Electronics, ISCE 2010*, Braunschweig, Germany, June 2010.
- [12] M. Jacob, S. Priebe, A. Maltsev, A. Lomayev, V. Erceg, and T. Kürner, "A ray tracing based stochastic human blockage model for the IEEE 802.11ad 60 GHz channel model," in *Proceedings of the 5th European Conference on Antennas and Propagation (EUCAP '11)*, pp. 3084–3088, IEEE, Rome, Italy, April 2011.
- [13] T. Wang, M. Umehira, H. Otsu, S. Takeda, T. Miyajima, and K. Kagoshima, "A twin cylinder model for moving human body shadowing in 60GHz WLAN," in *Proceedings of the 21st Asia-Pacific Conference on Communications, APCC 2015*, pp. 188–192, Japan, October 2015.
- [14] M. Jacob, S. Priebe, M. Peter, and M. Wisozki, "Fundamental analyses of 60 GHz human blockage," in *Proceedings of the IEEE EuCAP 2013*, pp. 117–121, IEEE, Gothenburg, Sweden, 2013.
- [15] G. R. Maccartney, S. Deng, S. Sun, and T. S. Rappaport, "Millimeter-wave human blockage at 73 GHz with a simple double knife-edge diffraction model and extension for directional antennas," in *Proceedings of the 84th IEEE Vehicular Technology Conference, VTC Fall 2016*, Canada, September 2016.
- [16] G. R. MacCartney and T. S. Rappaport, "A flexible millimeter-wave channel sounder with absolute timing," *IEEE Journal on Selected Areas in Communications*, vol. 35, no. 6, pp. 1402–1418, 2017.
- [17] P. Karadimas, B. Allen, and P. Smith, "Human body shadowing characterization for 60-GHz indoor short-range wireless links," *IEEE Antennas and Wireless Propagation Letters*, vol. 12, pp. 1650–1653, 2013.
- [18] A. J. Coulson, "Spectrum sensing using hidden Markov modeling," in *Proceedings of the 2009 IEEE International Conference on Communications, ICC 2009*, pp. 1–6, Dresden, Germany, June 2009.
- [19] K. Haghghi, E. G. Ström, and E. Agrell, "On optimum causal cognitive spectrum reutilization strategy," *IEEE Journal on Selected Areas in Communications*, vol. 30, no. 10, pp. 1911–1921, 2012.
- [20] "Iperf," <https://iperf.fr/>.
- [21] C. Bishop, *Pattern Recognition and Machine Learning*, Springer, Berlin, Germany, 2010.
- [22] A. Goldsmith, *Wireless communications*, Cambridge University Press, 2004.
- [23] H. Akaike, "A New Look at the Statistical Model Identification," *IEEE Transactions on Automatic Control*, vol. 19, no. 6, pp. 716–723, 1974.
- [24] S. R. Saunders and A. A. Zavala, "Antennas and propagation for wireless communication systems," Wiley, 2007.
- [25] A. Papoulis and S. Pillai, *Probability, Random Variables and Stochastic Processes*, McGraw-Hill, New York, NY, USA, 4th edition, 2002.
- [26] Y. Koda, K. Yamamoto, T. Nishio, and M. Morikura, "Time Series Measurement of IEEE 802.11ad Signal Power Involving Human Blockage with HMM-Based State Estimation," in *Proceedings of the 2017 IEEE 86th Vehicular Technology Conference (VTC-Fall)*, pp. 1–5, IEEE, Toronto, Canada, September 2017.

## Research Article

# Indoor Corridor Wideband Radio Propagation Measurements and Channel Models for 5G Millimeter Wave Wireless Communications at 19 GHz, 28 GHz, and 38 GHz Bands

Ahmed M. Al-samman , Tharek Abd Rahman , and Marwan Hadri Azmi

*Department Wireless Communication Centre, Faculty of Electrical Engineering, Universiti Teknologi Malaysia, 81310 Johor, Malaysia*

Correspondence should be addressed to Ahmed M. Al-samman; [ahmedsecure99@gmail.com](mailto:ahmedsecure99@gmail.com) and Tharek Abd Rahman; [tharek@fke.utm.my](mailto:tharek@fke.utm.my)

Received 16 September 2017; Revised 16 January 2018; Accepted 23 January 2018; Published 8 March 2018

Academic Editor: Dajana Cassioli

Copyright © 2018 Ahmed M. Al-samman et al. This is an open access article distributed under the Creative Commons Attribution License, which permits unrestricted use, distribution, and reproduction in any medium, provided the original work is properly cited.

This paper presents millimeter wave (mmWave) measurements in an indoor environment. The high demands for the future applications in the 5G system require more capacity. In the microwave band below 6 GHz, most of the available bands are occupied; hence, the microwave band above 6 GHz and mmWave band can be used for the 5G system to cover the bandwidth required for all 5G applications. In this paper, the propagation characteristics at three different bands above 6 GHz (19, 28, and 38 GHz) are investigated in an indoor corridor environment for line of sight (LOS) and non-LOS (NLOS) scenarios. Five different path loss models are studied for this environment, namely, close-in (CI) free space path loss, floating-intercept (FI), frequency attenuation (FA) path loss, alpha-beta-gamma (ABG), and close-in free space reference distance with frequency weighting (CIF) models. Important statistical properties, such as power delay profile (PDP), root mean square (RMS) delay spread, and azimuth angle spread, are obtained and compared for different bands. The results for the path loss model found that the path loss exponent (PLE) and line slope values for all models are less than the free space path loss exponent of 2. The RMS delay spread for all bands is low for the LOS scenario, and only the directed path is contributed in some spatial locations. For the NLOS scenario, the angle of arrival (AOA) is extensively investigated, and the results indicated that the channel propagation for 5G using high directional antenna should be used in the beamforming technique to receive the signal and collect all multipath components from different angles in a particular mobile location.

## 1. Introduction

The ever-growing data rate demand as well as the shortage of current frequency resources are the main challenges for the upcoming fifth generation (5G) of mobile communications [1–4]. The congestion of the current frequency band (below 6 GHz) and the narrowness of the wireless bandwidth are key problems for fifth generation wireless networks. Exploitation of the unused microwave and millimeter wave (mmWave) spectrum (spectrum between 6 and 300 GHz) is an efficient solution to overcome the 5G network's enormous data demand. With the huge bandwidth available in the millimeter wave band, mmWave communications have been proposed as an important part of the 5G mobile network that can provide multi-gigabit communication services such

as ultrahigh definition video (UHDV) and high definition television (HDTV) [5]. As with any wireless communication, the study of signal propagation is important for designing and modeling mmWave systems. Thus, characterization and modeling of such channel propagation in urban environments are some of the most important tasks in developing novel 5G mobile access networks. Recently, most research has focused on the 28 GHz band, the 38 GHz band, and the E-band (71–76 GHz and 81–86 GHz) [6]. In the past two decades, measurement campaigns were conducted in 28 GHz and 38 GHz mmWave bands for Local Multipoint Distribution Service (LMDS) [7, 8]. In addition, wideband NLOS measurements were performed by Violette et al. at the 9.6, 28.8, and 57.6 GHz bands in downtown Denver, where the results showed significant signal attenuation due

to obstruction by large buildings [9]. Propagation through a canopy of orchard trees was measured using continuous wave (CW) signals at 9.6, 28.8, and 57.6 GHz [10].

Several channel measurements have been conducted at some mmWave bands such as 6, 10, 11, 15, 18, 19, 26, 28, 32, and 38 GHz bands. In [11], the propagation characteristics of mmWaves were investigated in an indoor corridor environment for the line of sight (LOS) scenario at 6.5, 10.5, 15, 19, 28, and 38 GHz bands. In [12], frequency domain measurements were conducted at 28 GHz in a laboratory using a vector network analyzer (VNA) with 1 GHz bandwidth and 1 ns time resolution to estimate the channel parameters for multipath components (MPCs). The path loss, shadowing, polarization properties, and root mean square (RMS) delay spread were obtained. Some measurements have been conducted by New York University (NYU) in the 28 GHz and 73 GHz frequency bands in a typical indoor office environment [13–16]. Three large-scale propagation path loss models for use over the entire microwave and mmWave radio spectrum, namely, the alpha-beta-gamma (ABG) model, the close-in (CI) free space reference distance model, and the CI model with a frequency-weighted path loss exponent (CIF), were studied and compared for the bands from 2 to 73 GHz with different frequency bands [13]. Moreover, indoor measurements for wireless and backhaul communications have been conducted in the frequency band of 72 GHz [17, 18]. At Finland's Aalto University, mmWave measurements have been conducted in the 60 GHz and 70 GHz frequency bands [19, 20]. Measurement in mmWave has also attracted research interest by corporations, for example, Samsung, Ericsson, Qualcomm, and Huawei [21, 22]. Hur et al. have conducted measurements in the 28 GHz band in the indoor environment [23]. Moreover, different academic researchers have conducted other measurements for several types of indoor environments at the 28 GHz band [12, 24]. Wang et al. [25] have conducted wideband channel measurement at 26 GHz in an open office LOS environment.

In all of the previously conducted mmWave measurements related to the 5G vision, the candidate frequencies for 5G wireless communications were still under research. In addition, investigation of the time and angle dispersion spread parameters was limited in most previous 5G mmWave measurements. The focus of ongoing research related to mmWave communications is the study of propagation characteristics, channel modeling, beamforming, and medium access control design. Extensive research is still required to enable deployment of mmWave communications in cellular systems.

In this paper, characterization of an extensive indoor propagation channel is performed for three different mmWave bands above 6 GHz. The channel characteristics are investigated based on five path loss models. The power, time, and angle dispersion are analyzed for line of sight (LOS) and non-LOS (NLOS) scenarios. These parameters are studied based on the root mean square delay and angle spread, excess delay, and angle of arrival (AOA).

The rest of the paper is organized as follows. The measurement equipment and environment are described in Section 2. Section 3 discusses the channel model and postprocessing.

The path loss, time, and angular dispersion parameters are described in Section 4. The path loss model results and analysis are presented in Section 5. Section 6 provides an analysis of the power, time, and angle dispersion parameters. Finally, the conclusion is drawn in Section 7.

## 2. Measurement Setup

For sounding signal acquisition, the measurement setup for this work is described in detail as follows. The transmitter side of the wideband channel sounder consisted of an arbitrary waveform generator (AWG) M8190A, up-converter E8267D, and rubidium clock 6689. The M8190A AWG was used to generate wideband differential baseband in-phase quadrature (IQ); it could also output direct intermediate frequency (IF) signals with channel sounding. The baseband arbitrary waveform signal provided 1-ns multipath resolution from a pseudorandom binary sequence (PRBS). The E8267D up-converter could up-convert this differential baseband IQ into a radio frequency (RF) carrier (up to 40 GHz) with wide modulation bandwidth and could adjust the output power with its Automatic Line Controller (ALC) circuit. Two 6689 Pendulum clock units (one for Tx and one for Rx) were used in the channel sounder system for synchronization between transmitter and receiver; they could provide a high precision 10 MHz reference signal to all of the instruments with  $\leq 1e - 11$  accuracy and  $\leq 3e - 11$  stability. The trigger signals could be derived from a rubidium clock or 33522B Function Generation system. At the receiver side of the wideband channel sounder, a down-converter M9362AD01 was used to down-convert RF frequencies (up to 40 GHz) to IF, a hybrid amplifier/attenuator M9352A was used to amplify the IF signal, and finally, a 12-bit high speed digitizer M9703A of 1 GHz bandwidth (interleaving mode) was used to acquire the IF signal. An N5173B was used as the local oscillator (LO) for the down-converter M9362AD01. An M9300A was the Frequency Reference module that took in an external 10 MHz and output 10 MHz and 100 MHz standard references; all of the equipment could keep the relative phase stable (phase locked). Similar to a Tx 6689, an Rx 6689 Pendulum clock unit also provided a standard 10 MHz reference for all of the instruments. The Rx trigger signal was loaded by a function generator 33522B. The arbitrary waveform channel sounding (AWCS) signal and frequency settings of the Tx and Rx are provided in Table 1. Using this setup with a 1-ns multipath resolution, an extensive set of mmWave propagation measurements was conducted at 19, 28, and 38 GHz center frequencies. Figure 1 shows the photograph of the Tx and Rx apparatuses.

The measurements were conducted along a corridor on the second floor of the Menara Tun Razak Building in the Universiti Teknologi Malaysia (UTM) campus, Kuala Lumpur, Malaysia. The Menara Tun Razak Building is a 17-story building with discussion rooms and faculty offices. The size of the corridor is 1.80 m  $\times$  67 m and the ceiling height is 3 m. The corridor has plywood and glass doors, and the walls are constructed from concrete, glass, and gypsum board. The floor ground is covered with glazed ceramic tiles, and the corridor ceiling is composed of fiberglass

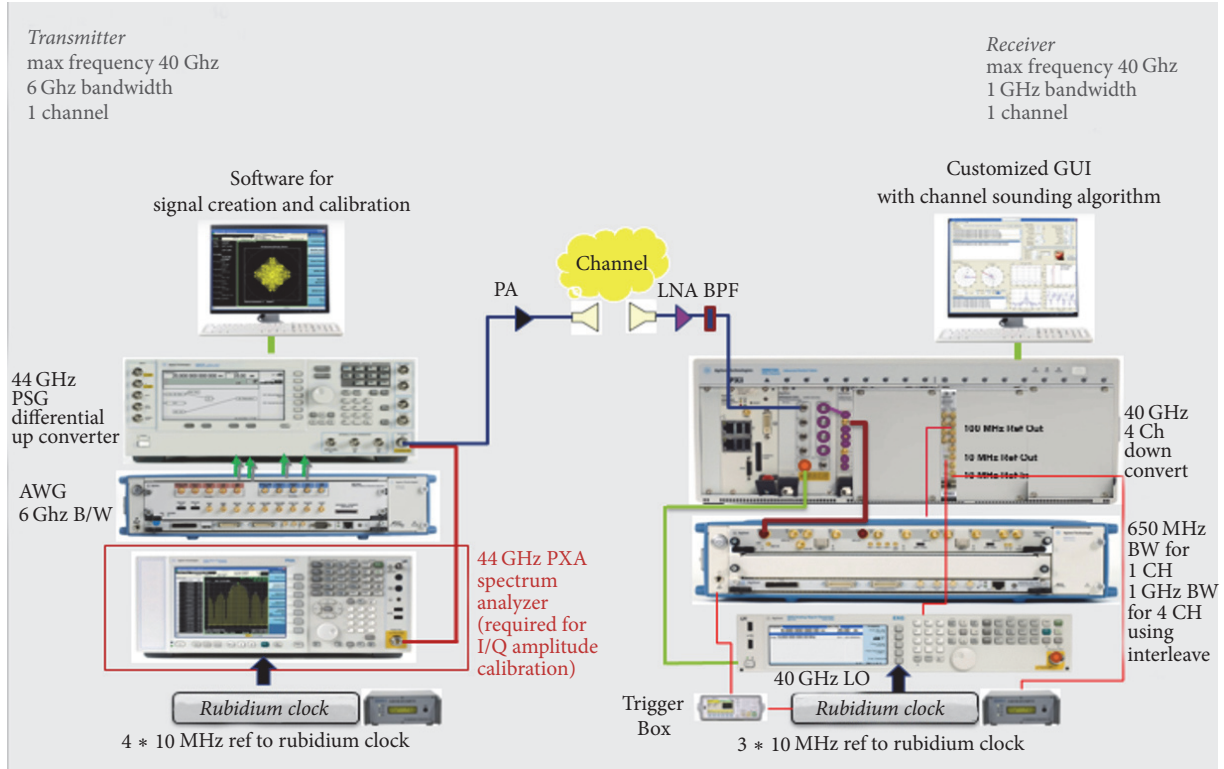


FIGURE 1: Photograph of the Tx and Rx apparatuses for the 5G channel sounder.

TABLE 1: Measurement setup parameters.

Carrier frequency (GHz)	19	28	38
AWCS signal	10th order PRBS (length = 1024)		
AWCS chip rate (Mcps)	1000		
AWCS chip duration (ns)	1		
Digitizer sampling rate (Gbps)	3.2		
PDP update rate (PDPs/second)	100		
RF BW (GHz)	1		
Rx LO power (dBm)	10		
Rx sensitivity	-120 dBm		
Tx power (dBm)	0		
Tx and Rx antenna gain (dBi)	11.6	11.6	15.2
HPBW (degrees)	46.4	44.8	28.3
Tx antenna height (m)	1.7		
Rx antenna height (m)	1.5		
Tx, Rx polarization	Vertical		

materials. Figure 2 shows the floor plan and description of the measurement environment. During the measurements, the Tx part is stationary and the Rx part is moved along a corridor, as depicted in Figure 2. The Tx antenna was placed 1.7 m above the floor to emulate an indoor hotspot in the wall, and the Rx antenna was placed 1.5 m above the floor (typical handset level heights). The measurement was started with

the Rx antenna located 1 m away from transmitter, and the received signal is recorded while keeping the Rx stationary at that position. Next, the Rx was moved 1 m farther away from its starting location, and the stationary measurements were repeated. The process was repeated likewise at 63 different locations of the Rx for the LOS scenario, each 1 m away from the previous adjacent location.

For the NLOS scenario, at the Tx-Rx separation distance of 18 m for the LOS scenario, the Rx antenna was moved by 3 m perpendicular to the LOS path, where the wall blocks the Tx from the Rx, and then the Rx was moved by 1 m up to 6 m, as shown in Figure 2. The Rx antenna was rotated by different angles at each NLOS location for all measured frequencies. With the zero degree (0°) rotation referring to the alignment of the Rx antenna with the Tx path, the Rx antenna was rotated, as shown in Figure 2. Based on these measurements, an extensive indoor channel characterization for mmWave bands is investigated as shown in Figure 2.

### 3. Data Processing and Channel Model

First, the influence of the measurement system was excluded from the recorded channel datasets using the system calibration procedure described in [26]. Next, the data were subjected to postprocessing using SystemVue software [27] and MATLAB Toolbox. The CIR was extracted by cross correlation between the received waveform and the transmitted arbitrary waveform signal. The Space-Alternating Generalized Expectation-maximization (SAGE) algorithm [28–30]

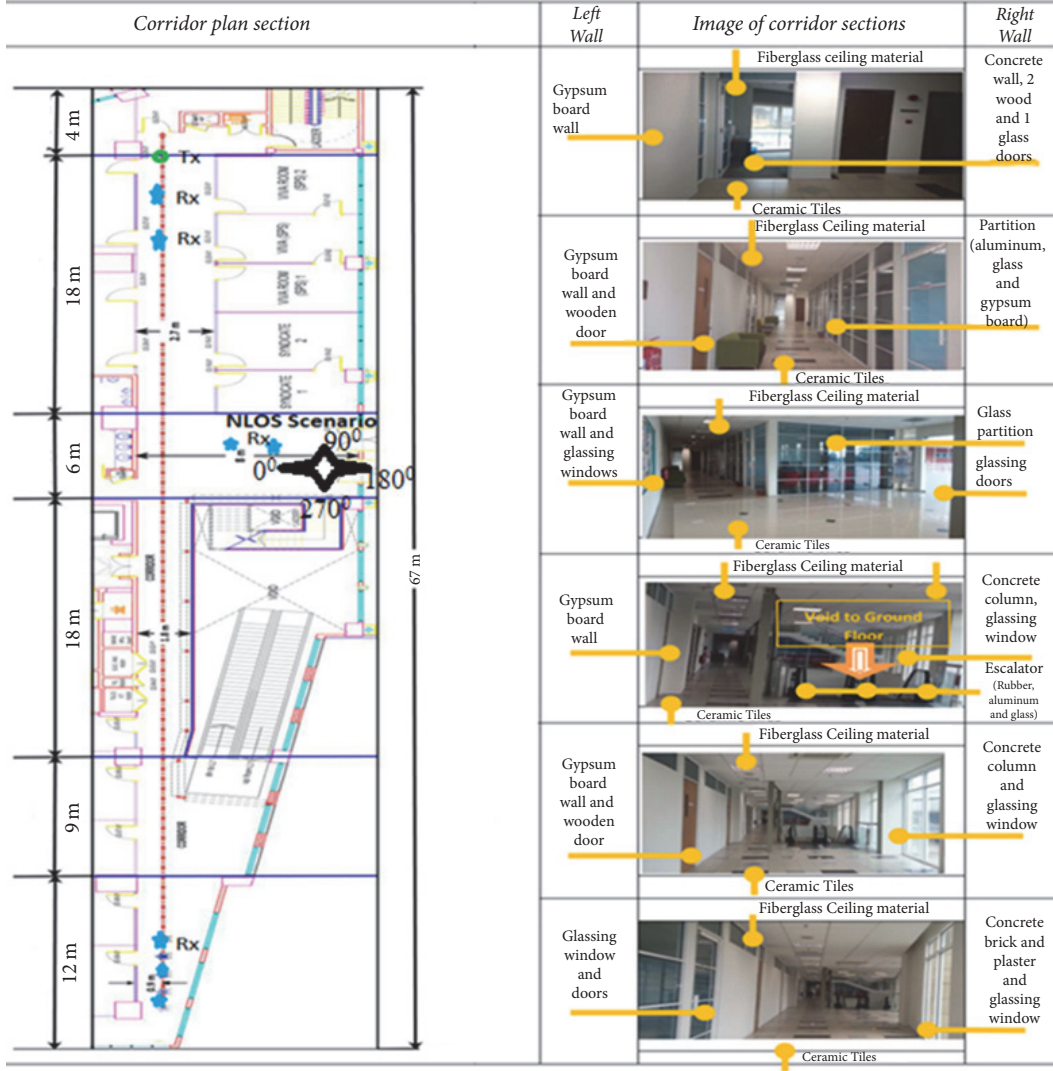


FIGURE 2: Floor plan and description of the environment.

was used to extract the parameters of MPCs, including path delay and path gain. The SAGE algorithm allowed an iterative determination of the maximum-likelihood estimation. The SAGE algorithm resolved the MPCs by an interference-cancellation, where the MPCs already estimated were subtracted from the considered signal.

The channel is excited by a transmitted pulse leading the receiver part to generate a summation of modified pulses with different attenuation factors and different time delays that represent the received waveform. The received waveform is called a multipath profile. The individual pulses arrived at the receiver through different paths, which are referred to as MPCs. The real CIR can be represented as a superposition of these paths, as in (1), that is, assuming no dispersion within the individual pulse [31].

$$h(\tau) = \sum_{i=1}^L a_i \delta(\tau - m_i), \quad (1)$$

where  $a_i$  and  $m_i$  are the  $i$ th path gain and delay, respectively.

For time-varying channels, (1) can be modified as [31]

$$h(t, \tau) = \sum_{i=1}^L a_i(t) \delta(\tau - m_i(t)), \quad (2)$$

where  $t$  is either the time or the spatial location. Assuming that the transmitter moves at a constant velocity away from the receiver, we can convert between the time and spatial location.

Denoting by  $q(\tau)$  the pulse transmissions waveform sent by the transmitter, the delayed received waveforms  $r(\tau)$  after propagating through the channel of (1) become

$$r(\tau) = q(\tau) \otimes h(\tau) = \sum_i \alpha_i q(\tau - m_i). \quad (3)$$

Based on the above equation, the power delay profile (PDP) can be expressed as

$$P(\tau) = \sum_i \alpha_i^2 q^2(\tau - m_i). \quad (4)$$

The path loss and time and angular dispersion parameters are derived from (4) as follows.

#### 4. Path Loss, Time, and Angular Dispersion Parameters

The path loss represents the fundamental quantities characterizing the wireless propagation channel and influencing the performance of any communication system. It is the inverse of the path gain, which is the amount of the signal power received. In a narrowband system, the path loss is defined as the amount of decay in the received power at a certain (carrier) frequency. For wideband and UWB radio, the path loss can be derived from the power of MPCs, which includes the joint effects of attenuation and time dispersion. The received signal energy can be calculated from the measured multipath profile as [32, 33]

$$P = \sum_i \alpha_i^2. \quad (5)$$

Denoting the average of the received signal energy at distance  $d$  using  $\bar{P}(d)$  and at reference distance  $d_0$  using  $\bar{P}(d_0)$ , the logarithmic value of the path loss can be computed using

$$\text{PL}(d) = -10 \log_{10} \left[ \frac{\bar{P}(d)}{\bar{P}(d_0)} \right]. \quad (6)$$

The time dispersion and angular dispersion play a key role in modern cellular systems [34]. The PDP of the received signal provides a good indication of the dispersion of the transmitted power over various paths. The time dispersion characteristics show the distribution of the power relative to the first arriving MPC. The time dispersion characteristics are usually quantified in terms of the mean excess delay and the RMS delay spread. To obtain these parameters, the PDP is normalized and all signals below a specific threshold  $x$  dB relative to the maximum are considered zero for the analysis [5, 35]. The required time for the energy of the received waveform to fall  $x$  dB relative to the maximum is defined as the maximum excess delay of the PDP. The RMS delay spread is computed as [36]

$$\tau_{\text{rms}} = \sqrt{\frac{\sum_i p_i \cdot (m_i - m_1 - \tau_m)^2}{\sum_i p_i}}, \quad (7)$$

where  $\tau_{\text{rms}}$  is the RMS delay spread that is defined by the square root of the second central moment of a power delay profile,  $p_i$  is the power for the  $i$ th path,  $m_i$  is the arrival time of the  $i$ th MPC,  $m_1$  is the first path arrival time, and  $\tau_m$  is the mean excess delay that can be represented by the first moment of the PDP as

$$\tau_m = \frac{\sum_i p_i \cdot (m_i - m_1)}{\sum_i p_i}. \quad (8)$$

In addition to the time dispersion, wireless propagation channels also show angular dispersion and determine the interaction between antennas and channels. In the wireless

channel model, the RMS angular spread of arrival (ASA) plays an important role and is calculated as follow [37]:

$$\Lambda_{\text{ASA}} = \sqrt{\frac{\sum_i p_i \cdot (\varphi_i - \mu_{\text{ASA}})^2}{\sum_i p_i}}, \quad (9)$$

where  $p_i$  is the power for  $l$ th path,  $\varphi_i$  is the angle of arrival (AOA), and  $\mu_{\text{ASA}}$  is the mean of the angle and is defined as

$$\mu_{\text{ASA}} = \frac{\sum_i p_i \cdot \varphi_i}{\sum_i p_i}. \quad (10)$$

#### 5. Path Loss Models, Results, and Analysis

In this paper, different path loss models are used to investigate the path loss in three different candidate bands for the 5G system. The close-in (CI) free space path loss model is a physically based model that uses the free space path loss (FSPL) at 1 m as the reference point (anchor-point) to estimate the path loss at different distances and spatial locations. In this work, we used the measured path loss at the anchor-point as the reference. The CI model can be calculated as [38]

$$P_L^{\text{CI}}(f, d) [\text{dB}] = P_L(f, d_0) + 10n \log_{10} \left( \frac{d}{d_0} \right) + X_\sigma, \quad (11)$$

where  $P_L(f, d)$  is the path loss at different frequencies with various Tx-Rx separation distance,  $n$  is the path loss exponent (PLE),  $P_L(f, d_0)$  is the path loss in dB at a close-in (CI) distance,  $d_0$ , of 1 m, and  $X_\sigma$  is a zero-mean Gaussian-distributed random variable with standard deviation  $\sigma$  dB (shadowing effect) [39].

Figure 3 shows the scatter plots of the path loss and the best fit CI model for the LOS scenario at 19, 28, and 38 GHz. It can be shown that the path loss increases as the separation distance and frequency are increased, where the highest path loss occurred at 38 GHz. The PLE values are 0.6, 0.6 and 1.3 for 19, 28, and 38 GHz, respectively. The PLE values for all frequencies are found to be less than those of the theoretical free space PLE ( $n = 2$ ), indicating that the MPCs added up constructively from both side walls along the corridor (i.e., a wave-guiding effect). The signal degradation at the 38 GHz band of 13 dB/decade is twice the degradation of the signal at 19 and 28 GHz. The standard deviation values  $\sigma$  at the 19 and 38 GHz bands are identical (2.4 dB). At the 28 GHz band, the standard deviation value is 3.3 dB.

Another popular path loss model is the floating-intercept (FI) model, which is used in the WINNER II and 3GPP standards [13]. This model is not a physically based model; however, it is suitable for some bands and environments, where the floating-intercept ( $\alpha$ ) parameter is close to the FSPL at 1 m and the slope line ( $\beta$ ) is comparable to the PLE. The FI model is defined as [11, 38]

$$P_L^{\text{FI}}(d) [\text{dB}] = \alpha + 10\beta \log_{10}(d) + X_\sigma^{\text{FI}}, \quad (12)$$

where  $X_\sigma^{\text{FI}}$  is the zero-mean Gaussian random variable dB with a standard deviation of  $\sigma$  dB.

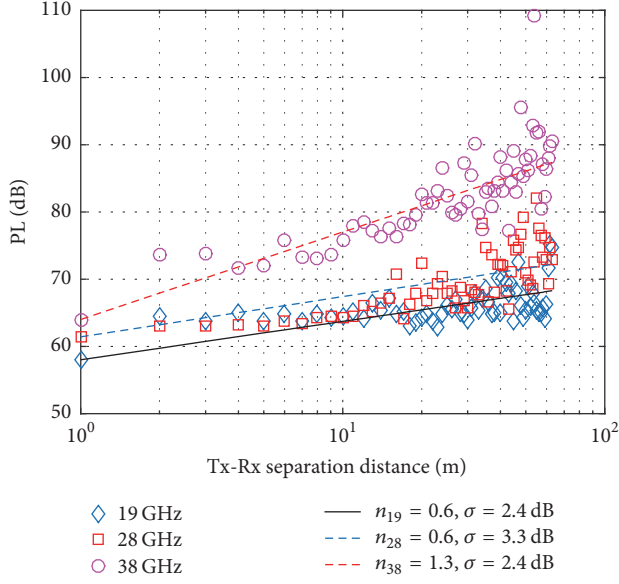
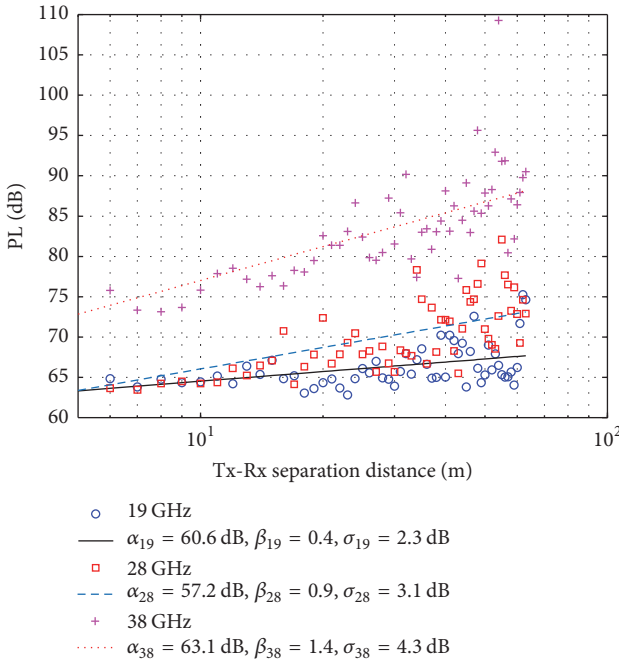
FIGURE 3: CI ( $d_0 = 1$  m) path loss model for the LOS scenario.

FIGURE 4: FI path loss model for the LOS scenario.

The FI path loss model at all measured bands is shown in Figure 4. The floating-intercept ( $\alpha$ ) values are 60.6 dB, 57.2 dB, and 63.1 dB for 19, 28, and 38 GHz, respectively. The  $\alpha$  values deviate from FSPL at 1 m by 2.6 dB, 4.2 dB, and 0.9 dB for 19, 28, and 38 GHz, respectively. The slope line ( $\beta$ ) values are 0.4, 0.9, and 1.4 for 19, 28, and 38 GHz, respectively. The  $\beta$  values are comparable with PLEs for the CI path loss model and the deviation of  $\alpha$  values from FSPL at 1 m is reasonable for all bands. This implies that the FI path loss model, which is mostly used in the 3GPP for frequency bands below 6 GHz,

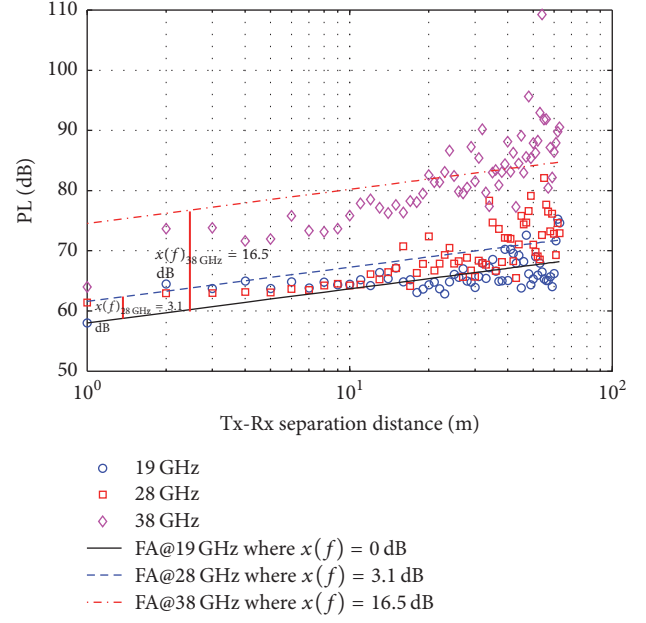


FIGURE 5: FA path loss model for the LOS scenario.

can be used with a suitable performance in mmWave bands for 5G systems. The standard deviation  $\sigma$  values for the FI model are 2.3 dB, 3.1 dB, and 4.3 dB for 19, 28, and 38 GHz, respectively.

To investigate the path loss with high frequency, the frequency attenuation (FA) path loss model is used, where the lowest measured frequency in a particular scenario is used as the reference frequency. The FA path loss model is defined as [11]

$$P_L^{FA}(f, d) [\text{dB}] = P_L(f_{\text{ref}}, d_0) + 10n_{\text{ref}} \log_{10} \left( \frac{d}{d_0} \right) + XF(f) + X_{\sigma}^{\text{FA}}, \quad (13)$$

where  $P_L(f_{\text{ref}}, d_0)$  is the path loss in dB at the close-in distance  $d_0$  of 1 m and the reference frequency  $f_{\text{ref}}$ . The  $f_{\text{ref}}$  in this model is defined as the lowest measured frequency using the same calibration environment;  $n_{\text{ref}}$  represents PLE at  $f_{\text{ref}}$ . The factor  $XF(f)$  is the frequency attenuation factor in dB, which represents the signal drop with frequency, and  $X_{\sigma}^{\text{FA}}$  is the shadow fading term with a standard deviation of  $\sigma$  dB. The FA path loss model is a physical-based model and is simple, as the CI model. The reference frequency  $f_{\text{ref}}$  is 19 GHz and the PLE ( $n_{\text{ref}}$ ) is 0.6.

The FA path loss model is shown in Figure 5. The  $XF(f)$  attenuation values of the FA model are 3.1 dB and 16.5 dB for 28 and 38 GHz, respectively. Because 19 GHz is the reference frequency, the  $XF(f)$  factor is 0 dB in this band. At the 28 GHz band, the signal degradation is low compared to the 19 GHz based on the  $XF(f)$  attenuation factor. The standard deviation  $\sigma$  values for the FA model are 2.4 dB, 3.1 dB, and 4.5 dB for 19, 28, and 38 GHz, respectively.

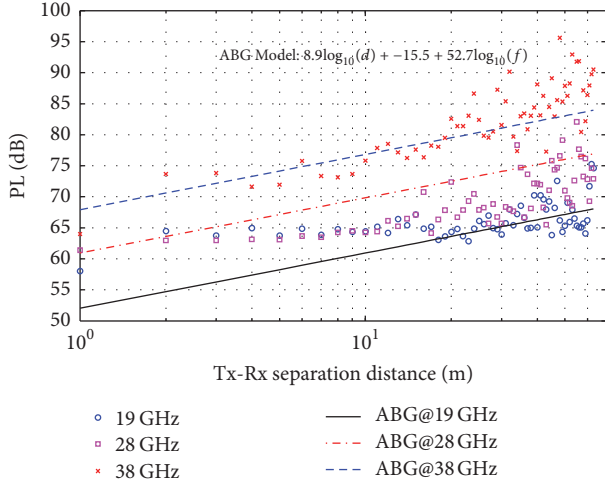


FIGURE 6: ABG multifrequency path loss model for the LOS scenario.

Because the path loss is measured at different bands, the multifrequency path loss models can be used to investigate the path loss for these bands. Here, the alpha-beta-gamma (ABG) and close-in free space reference distance with frequency weighting (CIF) path loss models are used for multifrequency path loss investigation. The ABG model includes a frequency dependent and distance-dependent term to describe path loss at various frequencies and is calculated as

$$\begin{aligned}
 P_L^{\text{ABG}}(f, d) [\text{dB}] &= 10\alpha \log_{10}\left(\frac{d}{d_0}\right) + \beta \\
 &+ 10\gamma \log_{10}\left(\frac{f}{1} \text{ GHz}\right) \\
 &+ X_{\sigma}^{\text{ABG}}, \quad d_0 = 1 \text{ m},
 \end{aligned} \quad (14)$$

where  $\alpha$  is the distance-dependent factor of path loss,  $\gamma$  is the frequency dependent factor,  $\beta$  is an optimized offset, and  $X_{\sigma}^{\text{ABG}}$  is the shadow fading term.

Figure 6 shows the ABG path loss model for all studied bands. The signal drop is found to be 8.9 dB/decade based on the distant-dependence factor ( $\alpha = 0.89$ ). The optimized offset  $\beta$  and frequency dependent factor  $\gamma$  values are  $-15.5$  dB and  $5.27$ , respectively.

The CIF model is a frequency-weighted model that employs the same FSPL anchor at 1 m as that of the CI model and is defined as

$$\begin{aligned}
 P_L^{\text{CIF}}(f, d) [\text{dB}] &= \text{FSPL}(f, d_{\text{ref}}) \\
 &+ 10n \left( 1 + b \left( \frac{f - f_0}{f_0} \right) \right) \log_{10}(d) + \chi_{\sigma}^{\text{CIF}},
 \end{aligned} \quad (15)$$

where  $n$  denotes the distance dependence of path loss and  $b$  is a linear frequency dependent factor of path loss over all considered frequencies. The parameter  $f_0$  is the weighted

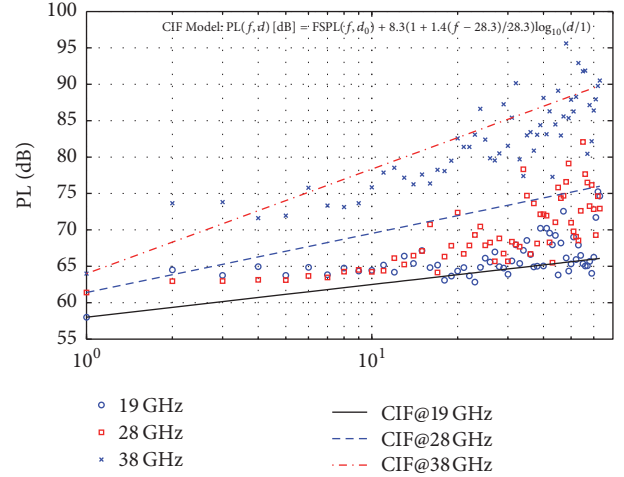


FIGURE 7: CIF multifrequency path loss model for the LOS scenario.

frequency average of all measurements for each specific environment and scenario, found by summing, over all frequencies the number of measurements at a particular frequency and scenario, multiplied by the corresponding frequency, and dividing that sum by the entire number of measurements taken over all frequencies for that specific environment and scenario. Based on the particular environment and scenario and the number of measurements at a particular frequency in this work,  $f_0 = 28.3$  GHz. The slope parameter is  $n = 0.8$  with the linear frequency dependent factor  $b = 1.4$  as depicted in Figure 7. It can be shown that with  $n = 0.8$ , the CIF path loss model can fit the measured data at all studied frequencies in this particular scenario.

## 6. Power, Delay, and Angle Dispersion Results and Analysis

The received power with different delay along the Tx-Rx separation distance in the 19 GHz band is shown in Figure 8. For all spatial locations along the corridor most of the received power arrived at the early excess delay (less than 10 ns). Furthermore, the maximum excess delay is less than 50 ns for all received paths with received power greater than  $-120$  dBm (noise floor). The received power between  $-70$  and  $-60$  dBm appears in the directed path (LOS path) that represents the first path in the LOS scenario. This implies that when the high directional antenna is used, most power falls in the LOS path. For the MPCs with an excess delay of less than 5 ns, the received power is in the range of  $-80$  to  $-70$  dBm, which is degraded by 10 dBm compared to the range of directed paths, as shown in Figure 8. The MPCs have received power of  $-90$  to  $-80$  dBm with an excess delay of less than 10 ns. Few paths with power less than  $-100$  dBm fall in the excess delay of more than 20 ns. It can be concluded that the power with a value greater than the noise floor by 10 dBm can be received at 19 GHz with 63 m Tx-Rx separation distance within a delay of less than 20 ns.

For the 28 GHz band, the power with different delays along the Tx-Rx separation distance is shown in Figure 9.

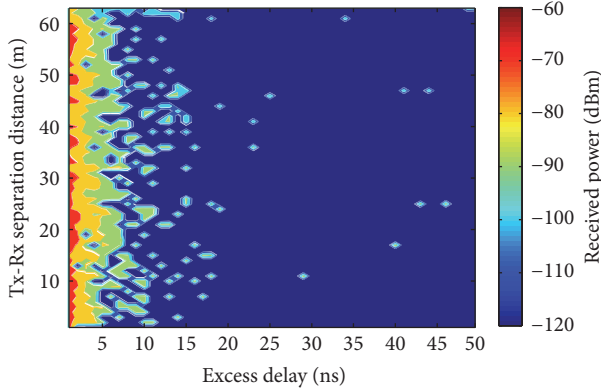


FIGURE 8: Received power at different delays for 19 GHz in all Tx-Rx separation distances considered for the LOS scenario.

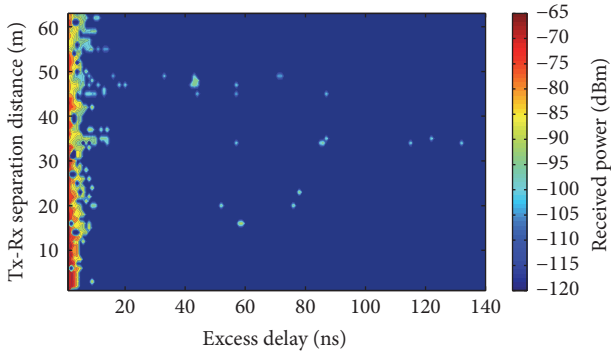


FIGURE 9: Received power at different delays for 28 GHz in all the considered Tx-Rx separation distances for the LOS scenario.

For this band, most of the received power is less than 10 ns; that is, most of the MPCs are received early. However, in some spatial locations, some MPC components are received at an excess delay greater than 100 ns and less than 140 ns, as shown in Figure 9. The received power with different delays along the Tx-Rx separation distance in the 38 GHz band is shown in Figure 10. In this band, only at the first 3 meters Tx-Rx separation distance is the received power greater than  $-75$  dBm with almost no delay (LOS path only). For the Tx-Rx separation distance of less than 15 m, the received power varies between  $-85$  and  $-80$  dBm, with a delay of less than 4 ns. In this band, no MPCs have a delay greater than 15 ns.

The RMS delay spread versus Tx-Rx separation distance for LOS scenario is shown in Figure 11. The maximum delay spread is found to be less than 35 ns for all studied bands. Moreover, the delay spread is the lowest at the 38 GHz band, and the delay spread decreases as the frequency increases. This implies that, with increased directivity of the antenna (lower HPBW), most power is concentrated in the directed path and no more MPCs are contributed in the received signal. The maximum delay spread values are 32.3 ns, 25.3 ns, and 2.6 ns at the spatial locations of 47 m, 34 m, and 32 m for 19, 28, and 38 GHz, respectively. The mean delay spread values are 5.7 ns, 2.3 ns, and 1.1 ns for 19, 28, and 38 GHz, respectively. This implies that most MPCs fall in the early bins.

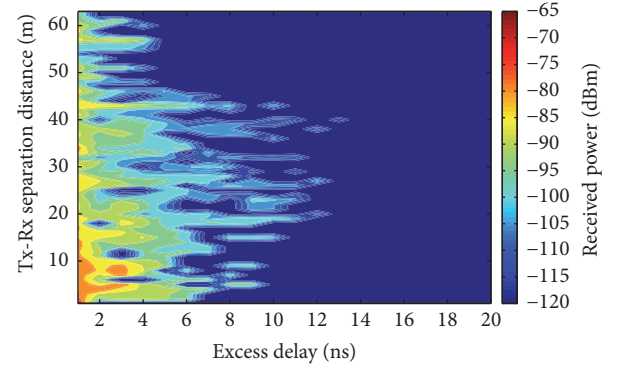


FIGURE 10: Received power at different delays for 38 GHz in all the considered Tx-Rx separation distances for the LOS scenario.

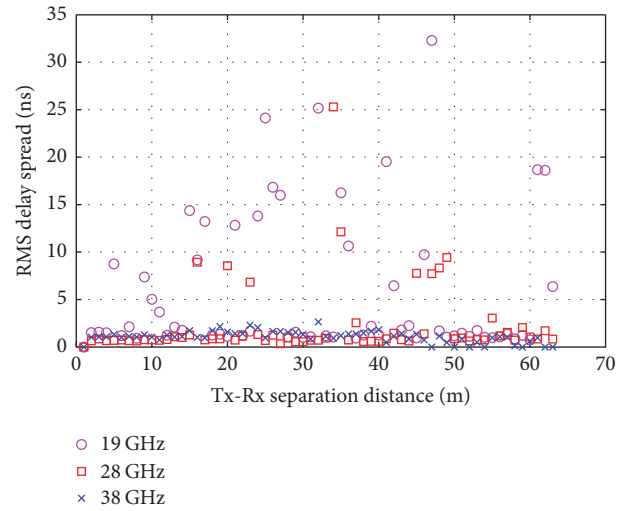


FIGURE 11: RMS delay spread versus Tx-Rx separation distance at all measured frequencies for the LOS scenario.

Figure 12 shows the CDF for the RMS delay spread in the NLOS scenario for all combined AOA at all measured bands. A total of 90% of the RMS delay spread is found to be less than 70 ns, 60 ns, and 90 ns for 19, 28, and 38 GHz, respectively. For the NLOS scenario, the delay spread is larger than the LOS scenario because no directed path is received and only the MPCs are captured.

The impact of the angle of arrival (AOA) on the propagation received power is investigated based on the conducted measurements in the NLOS scenario. Here, we set the  $-120$  dBm equipment sensitivity parameter as the noise floor; hence, signals with received powers below this value are considered to be very weak or nonexistent. The received signal powers during the measurement at  $0^\circ$  to  $330^\circ$  AOA with an interval of  $30^\circ$  in four different spatial locations of 3 m, 4 m, 5 m, and 6 m for the NLOS scenario are shown in Figure 13. The received signal power at four different spatial locations is found to vary with the AOA. In general, the variation occurs more for signals at higher frequency. The results in Figure 13 show that the signals can be received from all measured AOA at the lower band of 19 GHz for all

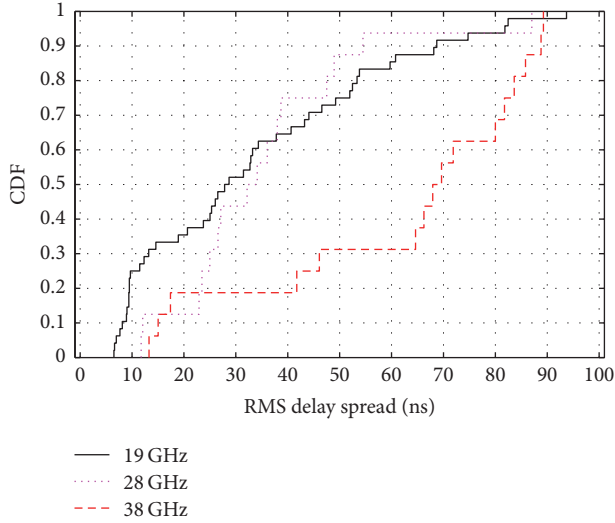


FIGURE 12: CDF for RMS delay spread at all measured frequencies for the NLOS scenario.

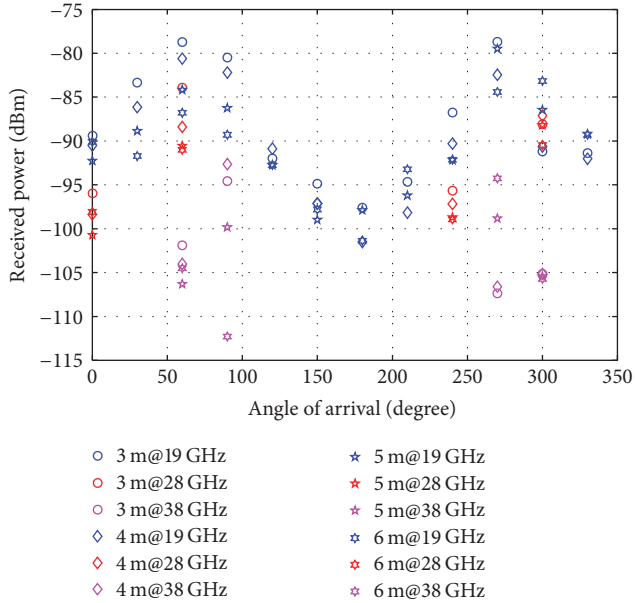


FIGURE 13: Received power versus AOA for all measured bands at different distances in the NLOS scenario.

4 different spatial locations. This, however, does not occur during measurement at the higher mmWave of 28 GHz and 38 GHz. Another notable observation from Figure 13 is that the variation of received signal power occurs at different AOAs and occurs at different spatial locations. The variation of the received signal power at different spatial locations is found to be greater at high frequency. The result in Figure 13 shows that, at an AOA of  $90^\circ$ , the received signal power decreased more than 10 dB for 1 m changes (from 5 m to 6 m) at 38 GHz, whereas the variation is only approximately 3 dB at 19 GHz within the same separation distance change. Another observation from the results in Figure 13 is that the received signal power is less at the shortest distance than at

TABLE 2: Angular spread parameters.

Parameter	28 GHz		38 GHz	
	3 m	6 m	3 m	6 m
$\Lambda_{ASA}$ [degree]	57.9	100.5	13.4	21
$\mu_{ASA}$ [degree]	74.8	247.7	90.6	268

the largest distance, that is, at an AOA of  $270^\circ$ , the received signal power at 5 m is approximately 4 dB less than that that at 6 m at 38 GHz. It is accordingly clear that this trend is not monotonic with distance, angle, and frequency because of the MPC constructive and destructive phenomena.

Figures 14(a) and 14(b) show the normalized power versus time of arrival (TOA) at different AOAs for the 28 GHz NLOS measurement at 3 m and 6 m distances, respectively. Here, Figure 14 presents the results for only 4 AOAs with the highest received signal power. The figure shows the impact of the signal arriving at different AOAs within the same propagation time delay. The figure also shows that the MPCs are dense for measurement with an NLOS distance of 3 m, whereas they are sparse at 6 m, as shown in Figure 14(b). Interesting observations are made when comparing the MPCs recorded during measurement at AOAs of  $0^\circ$  and  $300^\circ$  for measurement at  $0^\circ$  AOA is perpendicular to the propagation path from the LOS measurement, making it the shortest NLOS path. In Figure 14(a), the NLOS measurement at 28 GHz, however, showed that the signal at  $0^\circ$  AOA measurement has a higher time of arrival value when compared to the signal at  $300^\circ$  AOA. This observation illustrates the severe constructive and destructive interference that occurs when using a higher mmWave band for communications. Our results further showed the increased impact of the constructive and destructive interference scenario during higher propagation measurement of the 38 GHz band, as illustrated in Figure 15, where there are no received signals detected during  $0^\circ$  AOA measurement, even though it corresponds to the shortest NLOS path between the transmitter and receiver. The first 38 GHz signal to arrive at the receiver occurs at an AOA of  $90^\circ$  in Figure 15(a) and  $300^\circ$  in Figure 15(b) for a measurement conducted at the NLOS distances of 3 m and 6 m, respectively.

The AOA measurement results for the NLOS scenario in Figures 13, 14, and 15 indicate the significant impact of constructive and destructive interference for propagating signals at mmWave. This phenomenon can be exploited to improve signal reception using a receiver equipped with advanced signal processing and beamforming technology to substantially increase the signal-to-noise ratio (SNR) at the desired user by using the adaptive antenna system and diversity combining.

The angular spread parameters for 28 GHz and 38 GHz are estimated at 3 m and 6 m based on (9) and (10). The angular spread parameters are listed in Table 2. Note that the RMS angular spread and mean angle at 6 m are greater than that those at 3 m for both measured frequencies. This implies that the channel at 6 m can be effectively used to provide rich diversity for a multiple antenna system.

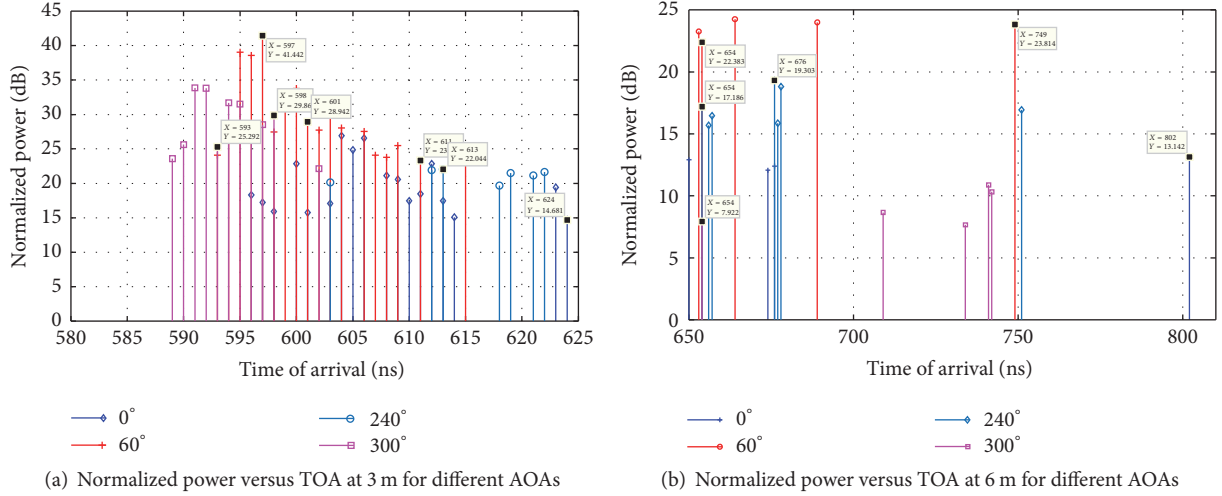


FIGURE 14: Example of some MPCs in a snapshot of CIR at 28 GHz for the NLOS scenario (a) at 3 m and (b) at 6 m.

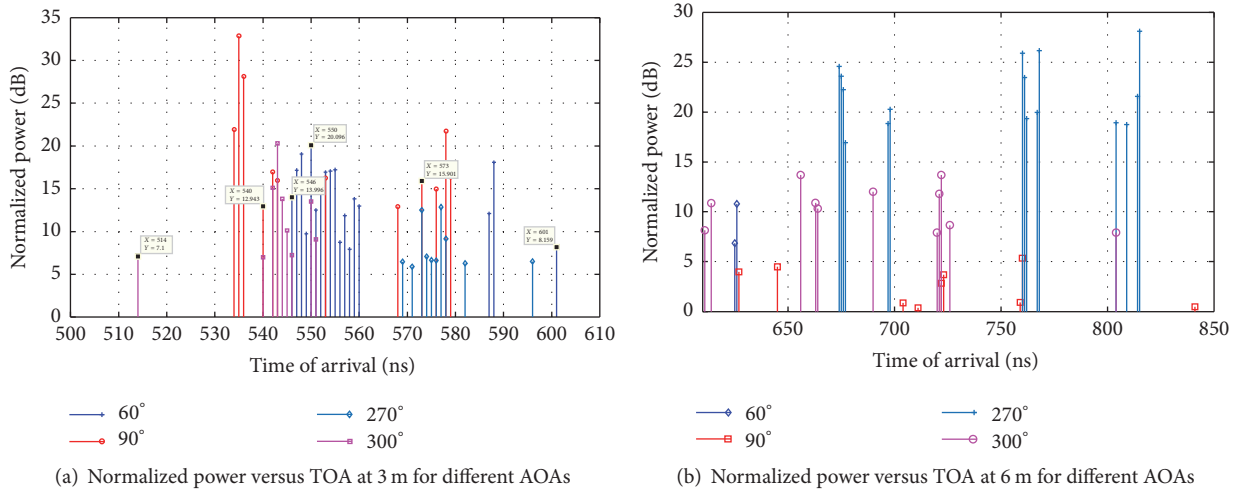


FIGURE 15: Example of some MPCs in a snapshot of CIR at 38 GHz for the NLOS scenario (a) at 3 m and (b) at 6 m.

## 7. Conclusion

This paper presented the channel propagation characteristics for three different frequency bands: 19 GHz, 28 GHz, and 38 GHz. The wideband measurements were conducted by using a 5G channel sounder with a high chip rate of 1000 Mcps. The measurement data were processed to obtain the channel impulse response (CIR) via the SAGE algorithm utilizing SystemVue software and MATLAB Toolbox. The path loss, angular spread, and RMS delay spread parameter for the three investigated frequency bands were then computed and analyzed. The CI, FI, FA, ABG, and CIF models were applied to investigate the path loss behavior for the three frequency bands in an indoor LOS environment. The path loss exponents for the LOS scenario were found to vary in the range of 0.6 to 1.3 for all models at the measured frequencies. These values are lower than the free space path loss exponent of 2 because of the wave-guiding effect from

both wall sides of the corridor. Our analysis on the time dispersion parameters showed that RMS delay spread values were low for the LOS scenario and that the highest energy arrived with the earliest MPCs. The RMS angular spread varies from  $13.4^\circ$  to  $100.5^\circ$  in the NLOS scenario. Finally, the impact of the angle of arrival (AOA) to the propagation received power was investigated based on the conducted measurement in the NLOS scenario. We found that the received signal power at the higher frequency band is more sensitive to the AOA variation. It is shown that, within a 1-m receiver movement, the received signal power decreases by up to 11 dB when using the 38 GHz band, and the signal only decreased approximately 3 dB for the 19 GHz band. In future work, to estimate the technology gap between 5G and 4G, it is useful to compare the performance of communicating using 28 GHz and 38 GHz with the LTE frequency band, that is, 2.6 GHz.

## Conflicts of Interest

The authors declare that there are no conflicts of interest regarding the publication of this paper.

## Acknowledgments

The authors would like to thank the Research Management Centre (RMC) at Universiti Teknologi Malaysia for funding this work under Grant no. Q.J130000.21A2.03E69. In addition, the authors would like to acknowledge the Universiti Teknologi Malaysia (UTM) Research Grant (Vot 4J218).

## References

- [1] F. B. Tesema, A. Awada, I. Viering, M. Simsek, and G. P. Fettweis, "Multiconnectivity for mobility robustness in standalone 5G ultra dense networks with intrafrequency cloud radio access," *Wireless Communications and Mobile Computing*, vol. 2017, Article ID 2038078, 17 pages, 2017.
- [2] M. Matalatala, M. Deruyck, E. Tanghe, L. Martens, and W. Joseph, "Performance evaluation of 5G millimeter-wave cellular access networks using a capacity-based network deployment tool," *Mobile Information Systems*, vol. 2017, Article ID 3406074, 11 pages, 2017.
- [3] A. Gupta and R. K. Jha, "A survey of 5G network: architecture and emerging technologies," *IEEE Access*, vol. 3, pp. 1206–1232, 2015.
- [4] S. Rangan, T. S. Rappaport, and E. Erkip, "Millimeter-wave cellular wireless networks: potentials and challenges," *Proceedings of the IEEE*, vol. 102, no. 3, pp. 366–385, 2014.
- [5] T. S. Rappaport, G. R. MacCartney, M. K. Samimi, and S. Sun, "Wideband millimeter-wave propagation measurements and channel models for future wireless communication system design," *IEEE Transactions on Communications*, vol. 63, no. 9, pp. 3029–3056, 2015.
- [6] Y. Niu, Y. Li, D. Jin, L. Su, and A. V. Vasilakos, "A survey of millimeter wave communications (mmWave) for 5G: opportunities and challenges," *Wireless Networks*, vol. 21, no. 8, pp. 2657–2676, 2015.
- [7] A. F. Elrefaie and M. Shakouri, "Propagation measurements at 28 GHz for coverage evaluation of local multipoint distribution service," in *Proceedings of the Wireless Communications Conference*, pp. 12–17, IEEE, Colorado, Colo, USA, 1997.
- [8] H. Xu, T. S. Rappaport, R. J. Boyle, and J. H. Schaffner, "38 GHz wideband point-to-multipoint radio wave propagation study for a campus environment," in *Proceedings of the IEEE 49th Vehicular Technology Conference. Moving Into a New Millennium*, pp. 1575–1579, IEEE, Texas, Tex, USA, 1999.
- [9] E. J. Violette, R. H. Espeland, R. O. DeBolt, and F. Schwing, "Millimeter-wave propagation at street level in an urban environment," *IEEE Transactions on Geoscience and Remote Sensing*, vol. 26, no. 3, pp. 368–380, 1988.
- [10] F. K. Schwing, E. J. Violette, and R. H. Espeland, "Millimeter-wave propagation in vegetation: experiments and theory," *IEEE Transactions on Geoscience and Remote Sensing*, vol. 26, no. 3, pp. 355–367, 1988.
- [11] A. M. Al-Samman, T. A. Rahman, M. H. Azmi et al., "Statistical modelling and characterization of experimental mm-wave indoor channels for future 5G wireless communication networks," *PLoS ONE*, vol. 11, no. 9, pp. 1–29, 2016.
- [12] X. Wu, Y. Zhang, C. Wang, G. Goussetis, M. Aggoune, and M. M. Alwakeel, "28 GHz indoor channel measurements and modelling in laboratory environment using directional antennas," in *Proceedings of the 2015 9th European Conference, Antennas Propag (EuCAP)*, pp. 1–5, 2015.
- [13] S. Sun, T. S. Rappaport, T. A. Thomas et al., "Investigation of prediction accuracy, sensitivity, and parameter stability of large-scale propagation path loss models for 5G wireless communications," *IEEE Transactions on Vehicular Technology*, vol. 65, no. 5, pp. 2843–2860, 2016.
- [14] G. R. MacCartney, M. K. Samimi, and T. S. Rappaport, "Omnidirectional path loss models in New York City at 28 GHz and 73 GHz," in *Proceedings of the 2014 25th IEEE Annual International Symposium on Personal, Indoor, and Mobile Radio Communication, IEEE PIMRC 2014*, pp. 227–231, IEEE, Washington, Wash, USA, September 2014.
- [15] S. Deng, M. K. Samimi, and T. S. Rappaport, "28 GHz and 73 GHz millimeter-wave indoor propagation measurements and path loss models," in *Proceedings of the IEEE International Conference on Communication Workshop, ICCW '15*, pp. 1244–1250, London, UK, June 2015.
- [16] G. R. MacCartney, S. Deng, and T. S. Rappaport, "Indoor office plan environment and layout-based mmWave path loss models for 28 GHz and 73 GHz," in *Proceedings of the 2016 IEEE 83rd Vehicular Technology Conference (VTC Spring)*, pp. 1–6, IEEE, Nanjing, China, May 2016.
- [17] S. Nie, G. R. MacCartney, S. Sun, and T. S. Rappaport, "72 GHz millimeter wave indoor measurements for wireless and backhaul communications," in *Proceedings of the IEEE 24th Annual International Symposium on Personal, Indoor, and Mobile Radio Communications (PIMRC '13)*, pp. 2429–2433, IEEE, London, UK, September 2013.
- [18] N. Zhang, X. Yin, S. X. Lu, M. Du, and X. Cai, "Measurement-based angular characterization for 72 GHz propagation channels in indoor environments," in *Proceedings of the 2014 IEEE Globecom Workshops, GC Wkshps 2014*, pp. 370–376, Texas, Tex, USA, December 2014.
- [19] S. Geng and P. Vainikainen, "Millimeter-wave propagation in indoor corridors," *IEEE Antennas and Wireless Propagation Letters*, vol. 8, pp. 1242–1245, 2009.
- [20] M. Kyrö, K. Haneda, J. Simola et al., "Measurement based path loss and delay spread modeling in hospital environments at 60 GHz," *IEEE Transactions on Wireless Communications*, vol. 10, no. 8, pp. 2423–2427, 2011.
- [21] W. Roh, J.-Y. Seol, J. Park et al., "Millimeter-wave beamforming as an enabling technology for 5G cellular communications: theoretical feasibility and prototype results," *IEEE Communications Magazine*, vol. 52, no. 2, pp. 106–113, 2014.
- [22] K. Haneda, L. Tan, Y. Zheng et al., "5G 3GPP-like channel models for outdoor urban microcellular and macrocellular environments," in *Proceedings of the 2016 IEEE 83rd Vehicular Technology Conference (VTC Spring)*, pp. 1–7, IEEE, Nanjing, China, May 2016.
- [23] S. Hur, Y.-J. Cho, J. Lee, N.-G. Kang, J. Park, and H. Benn, "Synchronous channel sounder using horn antenna and indoor measurements on 28 GHz," in *Proceedings of the IEEE International Black Sea Conference on Communications and Networking (BlackSeaCom '14)*, pp. 83–87, IEEE, Odessa, Ukraine, May 2014.
- [24] M. Lei, J. Zhang, T. Lei, and D. Du, "28 GHz indoor channel measurements and analysis of propagation characteristics," in *Proceedings of the 2014 25th IEEE Annual International Symposium on Personal, Indoor, and Mobile Radio Communication*,

- IEEE PIMRC '14*, pp. 208–212, IEEE, Washington, Wash, USA, September 2014.
- [25] Q. Wang, S. Li, X. Zhao, M. Wang, and S. Sun, “Wideband millimeter-wave channel characterization based on los measurements in an open office at 26 GHz,” in *Proceedings of the 2016 IEEE 83rd Vehicular Technology Conference (VTC Spring)*, pp. 1–5, IEEE, Nanjing, China, May 2016.
- [26] S. Brochure, “Keysight Technologies 5G Channel Sounding,” <http://about.keysight.com/en/newsroom/pr/2015/30jul-em15109.shtml>.
- [27] “SystemVue Software, 2217697, 2015,” <http://www.keysight.com/main/software.jsp?cc=MY&lc=eng&ckey=2217697&nid=-34264.804607.02&id=2217697&cmpid=zzfindeesof-Systemvue-Latest-Downloads>.
- [28] M. Kyrö, V.-M. Kolmonen, and P. Vainikainen, “Experimental propagation channel characterization of mm-wave radio links in urban scenarios,” *IEEE Antennas and Wireless Propagation Letters*, vol. 11, pp. 865–868, 2012.
- [29] X. Yin, Y. He, Z. Song, M.-D. Kim, and H. K. Chung, “A sliding-correlator-based SAGE algorithm for Mm-wave wideband channel parameter estimation,” in *Proceedings of the 8th European Conference on Antennas and Propagation, EuCAP '14*, pp. 625–629, IEEE, The Hague, Netherlands, April 2014.
- [30] J. A. Fessler and A. O. Hero, “Space-alternating generalized expectation-maximization algorithm,” *IEEE Transactions on Signal Processing*, vol. 42, no. 10, pp. 2664–2677, 1994.
- [31] A. M. Al-Samman, M. H. Azmi, T. A. Rahman, I. Khan, M. N. Hindia, and A. Fattouh, “Window-based channel impulse response prediction for time-varying ultra-wideband channels,” *PLoS ONE*, vol. 11, no. 12, Article ID e0164944, 2016.
- [32] A. Muqaibel, A. Safaai-Jazi, S. Riad, A. Attiya, and B. Woerner, “Path-loss and time dispersion parameters for indoor UWB propagation,” *IEEE Transactions on Wireless Communications*, vol. 5, no. 3, pp. 550–559, 2006.
- [33] C. W. Kim, X. Sun, L. C. Chiam, B. Kannan, F. P. S. Chin, and H. K. Garg, “Characterization of ultra-wideband channels for outdoor office environment,” in *Proceedings of the 2005 IEEE Wireless Communications and Networking Conference, WCNC '05: Broadband Wireless for the Masses - Ready for Take-off*, pp. 950–955, IEEE, Louisiana, La, USA, March 2005.
- [34] A. F. Molisch and F. Tufvesson, “Propagation channel models for next-generation wireless communications systems,” *IEICE Transactions on Communications*, vol. E97.B, no. 10, pp. 2022–2034, 2014.
- [35] A. M. Al-Samman, T. A. Rahman, M. Hadri, I. Khan, and T. H. Chua, “Experimental UWB indoor channel characterization in stationary and mobility scheme,” *Measurement*, vol. 111, pp. 333–339, 2017.
- [36] A. M. Al-Samman and T. A. Rahman, “Experimental characterization of multipath channels for ultra-wideband systems in indoor environment based on time dispersion parameters,” *Wireless Personal Communications*, vol. 95, no. 2, pp. 1713–1724, 2017.
- [37] T. Jiang, L. Tian, P. Tang, Z. Hu, and J. Zhang, “Basestation 3-dimensional spatial propagation characteristics in urban microcell at 28 GHz,” in *Proceedings of the 11th European Conference on Antennas and Propagation, EUCAP '17*, pp. 3167–3171, IEEE, Paris, France, March 2017.
- [38] G. R. MacCartney, T. S. Rappaport, S. Sun, and S. Deng, “Indoor office wideband millimeter-wave propagation measurements and channel models at 28 and 73 GHz for ultra-dense 5G wireless networks,” *IEEE Access*, vol. 3, pp. 2388–2424, 2015.
- [39] T. S. Rappaport, *Wireless Communications Principles and Practice*, 2nd edition, 2002.

## Research Article

# A Stochastic Geometry Approach to Full-Duplex MIMO Relay Network

Mhd Nour Hindia <sup>1</sup>, Moubachir Madani Fadoul,<sup>1</sup>  
Tharek Abdul Rahman,<sup>1</sup> and Iraj Sadegh Amiri <sup>2,3</sup>

<sup>1</sup>Wireless Communication Centre, Universiti Teknologi Malaysia, Skudai, Johor Bahru, Malaysia

<sup>2</sup>Computational Optics Research Group, Ton Duc Thang University, Ho Chi Minh City, Vietnam

<sup>3</sup>Faculty of Applied Sciences, Ton Duc Thang University, Ho Chi Minh City, Vietnam

Correspondence should be addressed to Iraj Sadegh Amiri; [irajsadeghamiri@tdt.edu.vn](mailto:irajsadeghamiri@tdt.edu.vn)

Received 24 June 2017; Revised 26 August 2017; Accepted 10 September 2017; Published 3 January 2018

Academic Editor: Patrick Seeling

Copyright © 2018 Mhd Nour Hindia et al. This is an open access article distributed under the Creative Commons Attribution License, which permits unrestricted use, distribution, and reproduction in any medium, provided the original work is properly cited.

Cellular networks are extensively modeled by placing the base stations on a grid, with relays and destinations being placed deterministically. These networks are idealized for not considering the interferences when evaluating the coverage/outage and capacity. Realistic models that can overcome such limitation are desirable. Specifically, in a cellular downlink environment, the full-duplex (FD) relaying and destination are prone to interferences from unintended sources and relays. However, this paper considered two-hop cellular network in which the mobile nodes aid the sources by relaying the signal to the dead zone. Further, we model the locations of the sources, relays, and destination nodes as a point process on the plane and analyze the performance of two different hops in the downlink. Then, we obtain the success probability and the ergodic capacity of the two-hop MIMO relay scheme, accounting for the interference from all other adjacent cells. We deploy stochastic geometry and point process theory to rigorously analyze the two-hop scheme with/without interference cancellation. These attained expressions are amenable to numerical evaluation and are corroborated by simulation results.

## 1. Introduction

Currently, the demand for the high capacity and low latency is dramatically increasing, corresponding to advancements in communication devices such as smartphones. It is expected that the wireless traffic volume of these communication devices will have a 1000-fold increase over the next decade which will be driven by the expected billions of connected devices by 2020 to access and share data anywhere and anytime [1]. The bottom line is that the technology has to move to higher frequency bands of millimeter wave to adapt the 5G future mobile communications, where a very large bandwidth in frequency band is available. With rapid increase in the number of connected devices, some challenges appear such as the capacity shortage, cost, and cochannel, and intercell interference especially at high dense network is rapidly increased [2]. Hence, the fifth-generation (5G) wireless systems should be able to support the ultradense

networks to adopt the exponential growth in mobile users and high data demand. To satisfy the quality of service (QoS), it is expected that the 5G network deployment will be much denser compared to that of 4G. However, as the network density increases, the interference will degrade the system's performance especially at cell edges (dead zone). One of these efficient solutions that allow the 5G network to meet its QoS requirements is to use relay to improve the ultradense network performance (capacity enhancement and coverage extension). Cooperative communication is an alternative way to achieve spatial diversity and multiplexing gain through Multiple-Input Multiple-Output (MIMO). MIMO attracted a lot of attention due to its potential for interference mitigation and capacity increase. FD relaying equipped with MIMO is able to perform spatial self-interference suppression [2–5]. The FD relaying looks to be an alternative solution to satisfy the high capacity demands of these wireless systems. The FD communication has attracted considerable attention

of many researchers and it is expected to be integrated into the 5G wireless systems. Most used cooperative protocols are the amplify-and-forward (AF) and the decode-and-forward (DF); the DF cooperative protocols can operate in either a half-duplex (HD) or full-duplex (FD) mode. Multiplexing loss occurred when implementing the HD mode in the DF protocol; this is attributed to the fact that, in the first time/frequency slot, the relay has to wait for the source's message and then forward the message in the next time slot to the destination. However, FD cooperative protocols can overcome the HD spectral loss via simultaneous transmission from source to relay and from relay to destination; this enables frequency reuse, higher throughput, and lower transmission delay [6]. However, there are two main issues hardening the implementation of FD system in cellular network: (1) the self-interference, that is, the relay's signal leakage from its transmit and receive antennas, and (2) the fact that the simultaneous transmission creates intercell interference [7].

However, cellular networks are usually modeled by placing the sources on a grid (with a regular shape) or arranging them on a line or circle as in the Wyner model with the relay and destination being either deterministically or randomly placed across the network to determine the signal-to-interference-and-noise ratio (SINR). The resulting SINR is complex and depends on multiple random variables. Hence, this fails to account for the randomness in the cellular network distribution [8] and the intercell interference [9]. Such models, however, are highly idealized and not tractable; hence, complex system level simulation is used to evaluate the outage/success probability and ergodic capacity. In order to reduce the dependence on simulations, the closed-form SINR was derived using stochastic geometry [10].

Since characterizing the SINR by the grid model and Wyner model is obviously not practicable, recently stochastic geometry has emerged as a powerful tool to model and quantify the capacity, interference, and success probability in cellular networks that are verified to be approximate to the actual networks [11]. The use of the Poisson point processes (PPP) model simplified the analysis and provided insight into the operation of the network in the form of scaling laws. Base station, relay, and destination parameters (e.g., path-loss exponent and transmit power) become the sign of the node in the PPP. Recently, under homogeneity condition, it was shown that the source positions are agnostic to the radio propagation; this makes the received power at the relay from any population of sources as if it generated from PPP, distributed sources [12, 13]. This justifies the modeling assumption of PPP sources and allows computing some metrics performance such as the success probability and Ergodic capacity [14, 15], while [16] derived an upper bound for the success probability. Obtaining full diversity order using distributed space-time codes is detailed in [17, 18], but a distributed space-time code requires precise signaling and very tight coordination among the relays, which increases the complexity and overhead in the system. This paper is motivated by the benefit of MIMO two-hop system, such as performance benefits and reducing implementation complexity.

Researchers have dealt with the interference in many different ways. For instance, an active method known as

analog cancellation, to cancel the interfering signal at the receiving antenna, utilizes additional radio frequency (RF) chains; and there is another active cancellation method known as digital cancellation, where the RSI is removed in the base-band level after the analog-to-digital converter [19]; another simple passive method is known as antenna separation, where the RSI is attenuated due to the path-loss between the transmitting and receiving antennas on the FD node. Further, reducing the FD interference using directional antennas is analyzed in [20]. References [21, 22] quantify the impact of self-interference of a heterogeneous network consisting of FD and HD nodes. They conclude that the capacity can be maximized by operating all nodes in either HD or FD compared to their mixtures, whereas [23] considers a single-cell setting and [22, 24] consider multicell setting. A cellular system comprising an FD source and HD destination has been illustrated in which the throughput gain is analyzed via extensive simulation [25]. In [26], the numbers of base station antennas and users antennas are increasing with a fixed ratio, while the capacity grows by the number of users and SNR. In this paper, however, we use a stochastic geometry tool to characterize the randomly distributed performance of FD MIMO relay nodes and derive bounds for the probability of successful transmission and ergodic capacity with/without interference cancellation. Finally, numerical results corroborate the theoretical findings with baseline scheme.

Next, in Section 2, the network system model is described. The SINR characterization is derived in Section 2.3; the success probability and the ergodic capacity are given in Section 2.4 and Section 2.5, respectively. Section 4 depicts the numerical results, and Section 5 offers the conclusion.

Throughout this paper, boldface lowercase letters (e.g.,  $\mathbf{x}$ ) represent vectors, and boldface uppercase letters (e.g.,  $\mathbf{X}$ ) represent matrices.  $\|\cdot\|_F$  is the Frobenius norm.  $\{\cdot\}^H$  stands for conjugate transpose, and  $\mathbb{E}[\cdot]$  denotes the expectation operator, while  $|\cdot|$  denotes the magnitude and the trace of a matrix is denoted by  $\text{tr}\{\cdot\}$ ;  $\det(\cdot)$  is the determinant;  $\text{diag}(x_1, \dots, x_n)$  is the diagonal matrix with diagonal components  $x_1, \dots, x_n$ ;  $\mathbf{I}_{N \times N}$  is the  $N$ -by- $N$  identity matrix;  $\mathbf{X}_{M \times N}$  is the  $M$ -by- $N$  zero matrix.

## 2. System Model

*2.1. System Setup.* In a downlink relay-assisted cellular network, consider a multiple independent FD dual-hop relaying system. The  $j$ th source  $S_j$  with message  $\mathbf{x}_{S_j}$ , equipped with  $M_s$  antennas communicates with  $N_d$  destinations  $D_j$  receiving antennas through relay set  $R_j$ , with messages  $\mathbf{x}_{R_j}$ , equipped with  $M_r$  and  $N_r$  transmitting and receiving antennas, respectively, as in Figure 1. The relay uses DF protocol; hence,  $R_j$  decodes the message from  $S_j$  and then reencodes the message before sending it to  $D_j$ . The relays are equipped with FD capabilities, where the reception and transmission of relay signal happen simultaneously. The main challenge is that relay's transmitted signal is coupled with its receiver chain, causing relay self-interference (RSI) via  $\mathbf{H}_{R_j}$  channel and source causes interference to other relay known as source-relay interference (SRI) via  $\mathbf{H}_{S,R_j}$  channel in addition to

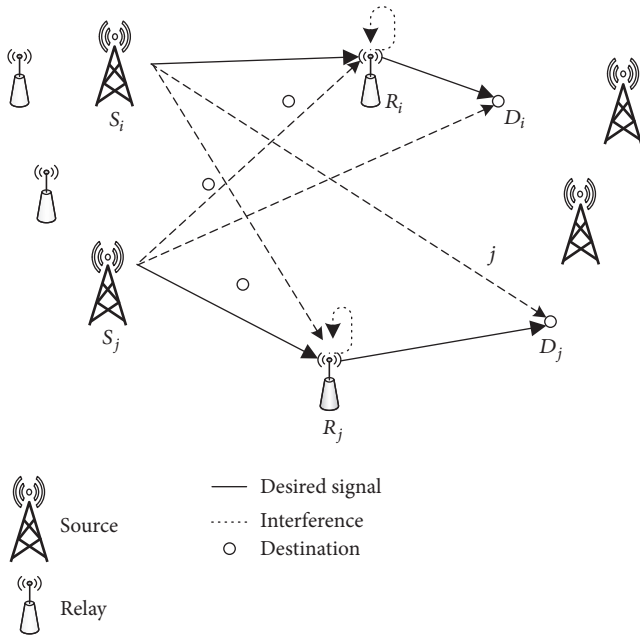


FIGURE 1: System model depicting cellular network, in which the source ( $S$ ) is having  $M_s$  transmitting antennas, willing to communicate with  $N_d$  receiving antennas, at the destination ( $D$ ), with the help of relay ( $R$ ), equipped with  $M_r$  and  $N_r$  transmitting and receiving antennas, respectively. The solid lines show desired signal, and the dashed lines show possible interferences such as RSI, IRI, SDI, and SRI.

the interference from the sources to the destinations causing source-destination interference (SDI) via  $\mathbf{H}_{S_i D_j}$ . Space division multiplexing is applied so that the two hops are separated.

The locations of sources, relays, and destinations are assumed to be stationary independently marked PPP with intensity  $\lambda_s$ ,  $\lambda_R$ , and  $\lambda_D$  on  $\mathbb{R}^2 \times \mathbb{R}^2 \times \mathbb{R}^2$ , respectively. In order to investigate the performance of a random access wireless network, consider a classical receiver located at the origin. Conditioning on the node's event lying at the origin does not affect the statistics of the rest of the process as an outcome from Palm probabilities of a Poisson process. Furthermore, the statistics of received signal at the intended receiver are observable by any receiver due to the stationarity of Poisson process [10].

**2.2. Channel Model.** The downlink cellular network is comprised of sources  $S_i$  and  $S_j$ , relays  $R_i$  and  $R_j$ , and destinations  $D_i$  and  $D_j$ . Previous studies on cellular networks assumed that the sources and relays are positioned regularly as grid model. However, in practice, this is not true and there are some random characteristics. We applied homogeneous PPP to the spatial distribution of the sources and relays to remedy the model as in [11, 15]. Each destination is served by the nearest relay or destination. This means that the cell area of each source or relay constitutes a Voronoi tessellation [27] as in Figure 2, whereas, in grid model in Figure 3, the sources are located on the centers of hexagonal model, while the relays and destinations are distributed in each cell uniformly. This

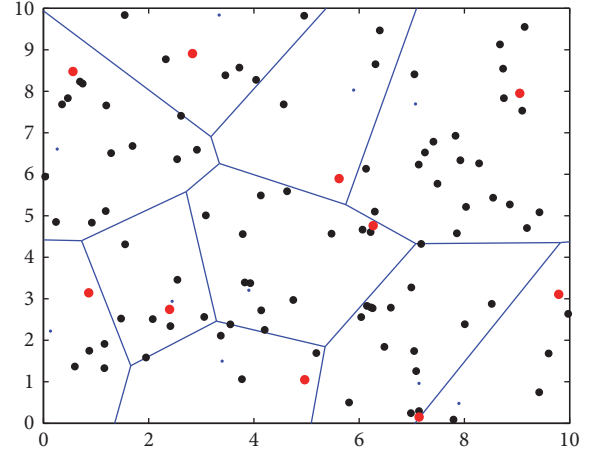


FIGURE 2: The cellular network topology, in which each Voronoi cell is the coverage area of a source and relay distributed as PPP; the cell area of each source and relay forms a Voronoi tessellation, where the red circle represents source, blue dot represents relay, and the black circle represents the destination.

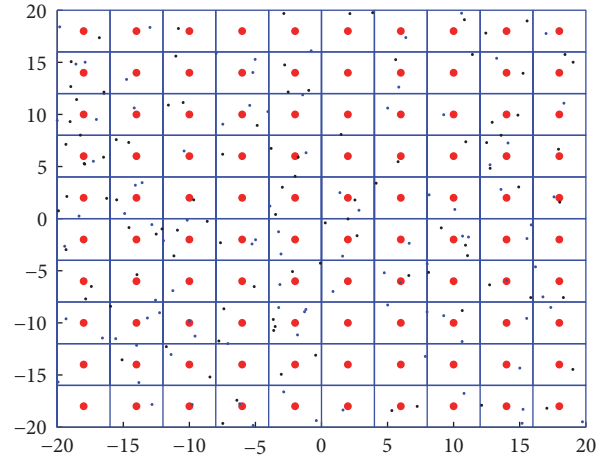


FIGURE 3: The grid cellular network topology, in which each Voronoi cell is the coverage area of a source distributed as PPP, where the red circle represents sources, blue dot represents relay, and the black circle represents the destination.

model does not lead to a tractable model; thus, it is evaluated via Monte Carlo simulations. When a destination attempts to access the sources, it chooses to connect directly or through relay in the Voronoi cell. Let the source  $S_j$  transmit the message  $\mathbf{x}_{S_j}$  to the  $j$ th relay  $R_j$ ;  $R_j$  receives and transmits simultaneously on the same frequency causing RSI through the channel  $\mathbf{H}_{R_j}$  if  $R_j \in \Phi$  for the same  $j$ th relay  $R_j$  and receives IRI through the channel  $\mathbf{H}_{R_i R_j}$  if  $R_i R_j \in \Phi$  from the other  $i$ th relay  $R_i$ , in addition to interference from other source  $S_i$ .  $\mathbf{x}_{S_j} \in \mathbb{C}^{M_s \times 1}$  and  $\mathbf{x}_{R_j} \in \mathbb{C}^{M_r \times 1}$  are transmitted signals from  $S_j$  and  $R_j$  nodes respectively.

The propagation through two-hop wireless channel is subject to path-loss attenuation modeled as  $\tilde{R}^{-\alpha}$  and  $\hat{R}^{-\alpha} \forall x \in \Phi$  for distances  $\tilde{R}$  and  $\hat{R}_j$ , respectively, with path-loss exponent  $\alpha > 2$ . The sources and relays transmit with power  $\tilde{p}$  and power  $\hat{p}$ . For such channel, the sources cover large areas,

while relays cover small areas with separation distances  $\tilde{R}_j$  and  $\hat{R}_j$  ( $\tilde{R}_j \gg \hat{R}_j$ ) given  $\tilde{\rho}\mathbf{H}_{S_j R_j} \tilde{R}_j^{-\alpha}$  if  $S_j R_j \in \Phi$  and  $\hat{\rho}\mathbf{H}_{R_j D_j} \hat{R}_j^{-\alpha}$  if  $R_j D_j \in \Phi$ . The interfering relays constitute the marked process  $\Phi = \{(X_i, \mathbf{H}_{R_i R_j}, \mathbf{H}_{R_j})\}$ , with  $X_i$  denoting the location of the transmitting relay node. Hence, the relay receives interference power from itself,  $\tilde{\rho}\mathbf{H}_{R_j}$ , and from the  $i$ th interfering relay and source as  $\tilde{\rho}\mathbf{H}_{R_i R_j} |X_i|^{-\alpha}$  and  $\tilde{\rho}\mathbf{H}_{S_i R_j} |X_i|^{-\alpha}$ , respectively. The channels  $\mathbf{H}_{S_j R_j} \in \mathbb{C}^{N_r \times M_s}$ ,  $\mathbf{H}_{R_j} \in \mathbb{C}^{N_r \times M_r}$ ,  $\mathbf{H}_{R_i R_j} \in \mathbb{C}^{N_r \times M_r}$ ,  $\mathbf{H}_{R_j D_j} \in \mathbb{C}^{N_d \times M_r}$ , and  $\mathbf{H}_{S_i D_j} \in \mathbb{C}^{M_s \times N_d}$  are the channel gain matrices from source-to-relay, relay itself, interrelay, relay-to-destination, and source-to-destination, respectively. The power constraints on transmit signals are  $\mathbb{E}\{|\mathbf{x}_{S_j}|^2\} = 1$ ,  $\mathbb{E}\{|\mathbf{x}_{R_j}|^2\} = 1$ , and  $\mathbb{E}\{|\mathbf{x}_{R_i R_j}|^2\} = 1$ .  $\mathbf{y}_{R_j} \in \mathbb{C}^{N_r \times 1}$  and  $\mathbf{y}_{D_j} \in \mathbb{C}^{N_d \times 1}$  are received signals at  $R_j$  and  $D_j$  nodes. All channels experience Rayleigh fading with parameter  $\mu \sim \text{Exp}(\mu)$ . The entries of each matrix are independent and identically distributed (i.i.d.) complex Gaussian variables with zero mean and variance  $\sigma^2$ .  $\mathbf{n}_R$  and  $\mathbf{n}_D$  are independent circularly symmetric complex Gaussian noise vectors with probability distributions  $\mathcal{N}(0, \mathbf{I})$  and  $\mathcal{N}(0, \mathbf{I}_D)$ , respectively, and are uncorrelated to  $\mathbf{x}_S$  and  $\mathbf{x}_R$ .

**2.3. SINR Characterization.** In this section, we formulate the signal-to-interference-plus-noise ratio (SINR), which is needed in the next section to analyze the probability of successful transmission. In doing so, we study the SINR of the SR hop and the SINR of the RD hop.

**2.3.1. SR Hop.** Consider the  $j$ th source node  $S_j$  located at the origin and, according to the stationarity of  $\Phi$  and building on Slivnyak's theorem [10, Ch. 8.5], we hence express the statistics of relay-received signal  $l(R_j, x) = |X_x|^{-\alpha}$ , with  $|X_x|$  being the distance of  $x$  from the origin. Therefore the received signal at the  $j$ th relay node contains the desired signal plus interference and noise ratio, RSI, and SRI, as given as follows:

$$\mathbf{y}_{R_j} \triangleq \underbrace{\left( \sqrt{\tilde{\rho}\tilde{R}_j^{-\alpha/2}} \mathbf{H}_{S_j R_j} \mathbf{x}_{S_j} + \mathbf{n}_{R_j} \right)}_{\text{desired signal plus noise}} + \underbrace{\sqrt{\tilde{\rho}\mathbf{H}_{R_j}} \tilde{\mathbf{x}}_{S_j}}_{\text{RSI}} + \underbrace{\sqrt{\tilde{\rho}\tilde{R}_j^{-\alpha/2}} \mathbf{H}_{S_i R_j} \tilde{\mathbf{x}}_{S_i}}_{\text{SRI}}. \quad (1)$$

The resulting SINR at the relay is obtained as

$$\text{SINR}_{R_j} \triangleq \frac{\tilde{\rho}\tilde{R}_j^{-\alpha} |\mathbf{H}_{S_j R_j}|^2}{I_{R_j} + \sigma_{R_j}^2}, \quad (2)$$

where  $I_{R_j}$  is the overall interference (RSI and SRI) at  $j$ th relay; that is,

$$I_{R_j} \triangleq \sum_{\{i,j\} \in \Phi} \left( \tilde{\rho}\tilde{R}_j^{-\alpha} |\mathbf{H}_{S_i R_j}|^2 \right) + \left( \tilde{\rho} |\mathbf{H}_{R_j}|^2 \right). \quad (3)$$

For simplicity, we assume that this hop is interference-limited and, therefore,  $I_{R_j} \gg \sigma_{R_j}^2$ .

**2.3.2. RD Hop.** Consider the  $j$ th relay node  $S_j$  located at the origin and, according to the stationarity of  $\Phi$  and building on Slivnyak's theorem, we express  $l(D_j, x) = |X_x|^{-\alpha}$ , with  $|X_x|$  being the distance of  $x$  from the origin. Therefore the received signal at the  $j$ th destination node contains the desired signal plus interference and noise ratio, as shown as follows:

$$\mathbf{y}_{D_j} \triangleq \underbrace{\sqrt{\tilde{\rho}\hat{R}_j^{-\alpha/2}} \mathbf{H}_{R_j D_j} \tilde{\mathbf{x}}_{S_j} + \mathbf{n}_{D_j}}_{\text{desired signal plus noise}} + \underbrace{\sqrt{\tilde{\rho}\tilde{R}_i^{-\alpha/2}} \mathbf{H}_{S_i D_j} \tilde{\mathbf{x}}_{D_i}}_{\text{SDI}} \quad (4)$$

The resulting SINR at the destination is

$$\text{SINR}_{D_j} \triangleq \frac{\tilde{\rho}\hat{R}_j^{-\alpha} |\mathbf{H}_{R_j D_j}|^2}{I_{D_j} + \sigma_{D_j}^2}, \quad (5)$$

where  $I_{D_j}$  captures the interference from other source to destination for the RD hop:

$$I_{D_j} \triangleq \sum_{\{i,j\} \in \Phi} \left( \tilde{\rho}\tilde{R}_j^{-\alpha} |\mathbf{H}_{S_i D_j}|^2 \right). \quad (6)$$

For simplicity, we assume that this hop also is interference-limited and therefore  $I_{D_j} \gg \sigma_{D_j}^2$ . Furthermore, the mean link distance of  $I_{S_i R_j}$  and  $I_{R_i R_j}$  is  $\mathbb{E}[I_{S_i R_j}] = \tilde{\rho}\tilde{R}^{-\alpha}$  and  $\mathbb{E}[I_{R_i R_j}] = \tilde{\rho}\tilde{R}_j^{-\alpha}$ , respectively, such that  $\mathbb{E}[I_{S_i R_j}] \gg \mathbb{E}[I_{R_i R_j}]$ .

**2.4. Success Probability.** One of our performance measures is the success probability, which, defined as the success probability of message transmission from the source to destination over the two hops, is given by a joint complementary cumulative distribution function (CCDF) of  $\text{SINR}_{R_j}$  and  $\text{SINR}_{D_j}$ . We formulate it by  $P_{\text{suc}} \triangleq \mathbb{P}(\text{SINR}_{R_j} \geq \theta_R, \text{SINR}_{D_j} \geq \theta_D)$ , where  $\theta$  is the given SINR threshold. Due to independent sampling of a point process, there is no correlation between the two hops.

$$P_{\text{suc}} = P_{\text{suc}}^{(\text{SR})} P_{\text{suc}}^{(\text{RD})}, \quad (7)$$

where  $P_{\text{suc}}^{(\text{SR})} \triangleq \mathbb{P}(\text{SINR}_{R_j} \geq \theta_R)$  and  $P_{\text{suc}}^{(\text{RD})} \triangleq \mathbb{P}(\text{SINR}_{D_j} \geq \theta_D)$ .

**2.4.1. SR Hop.** Successful SR hop transmission occurs if

$$\frac{\tilde{\rho}\tilde{R}_j^{-\alpha} |\mathbf{H}_{S_j R_j}|^2}{I_{R_j}} \geq \theta_R; \quad (8)$$

the given threshold  $\theta$  satisfied a target SINR; the probability of successful transmission for a relay is

$$\begin{aligned}
\mathbb{P}\left(\text{SINR}_{R_j} \geq \theta\right) &= \mathbb{P}\left(\frac{\tilde{\rho}\tilde{R}_j^{-\alpha} \left|\mathbf{H}_{S_j R_j}\right|^2}{I_{R_j}} \geq \theta_R\right) \\
&= \mathbb{P}\left(\left|\mathbf{H}_{S_j R_j}\right|^2 \geq \theta_R \tilde{\rho}^{-1} \tilde{R}_j^\alpha I_{R_j}\right) \\
&= \int_0^\infty \mathbb{P}\left(\left|\mathbf{H}_{S_j R_j}\right|^2 \geq s \theta_R \tilde{\rho}^{-1} \tilde{R}_j^\alpha\right) f_{I_{R_j}}(s) ds \\
&= \int_0^\infty F_{\text{SR}}^c\left(s \theta_R \tilde{\rho}^{-1} \tilde{R}_j^\alpha\right) f_{I_{R_j}}(s) ds,
\end{aligned} \tag{9}$$

where (9) is obtained by conditioning  $s$  and its complementary cumulative distribution function is denoted by  $F^c(\cdot)$ . Next, we provide the success probability analysis of the SR hop.

**Theorem 1.** *Let the interfering relays transmitters form a Poisson process of intensity  $\lambda_R$  around relay receivers. The success probability of the SR hop is*

$$P_{\text{suc}}^{(\text{SR})} \triangleq \sum_{n=0}^{N_r-1} \left[ \frac{(-s)^n}{n!} \frac{d^n}{ds^n} \mathcal{L}_{I_{R_j}}(s) \right]_{s=\theta_R \tilde{\rho}^{-1} \tilde{R}_j^\alpha}, \tag{10}$$

where  $\mathcal{L}_{I_{R_j}}$  is the Laplace transform of the interferences  $I_{R_j}$ .

$$\mathcal{L}_{I_{R_j}}(s) \triangleq \frac{1}{(1+s\tilde{\rho})} \exp(-\lambda_S \Upsilon(s)) \tag{11}$$

$$\Upsilon(s) \triangleq \int_0^\infty \left(2\pi - \frac{1}{1+s\tilde{\rho}r^{-\alpha}} \Psi(s, r)\right) r dr \tag{12}$$

with

$$\Psi(s, r) \triangleq \int_0^{2\pi} \frac{d\varphi}{1+s\tilde{\rho}(\tilde{R}_j^2 + r^2 + 2\tilde{R}_j r \cos \varphi)^{-\alpha/2}}. \tag{13}$$

*Proof.* Refer to Appendix B.  $\square$

The result in Theorem 1 provides a fundamental limit on the SR hop and its performance in an interference-limited scenario.

**2.4.2. RD Hop.** Successful RD hop transmission occurs if

$$\begin{aligned}
\mathbb{P}\left(\text{SINR}_{D_j} \geq \theta_D\right) &= \mathbb{P}\left(\frac{\tilde{\rho}\tilde{R}_j^{-\alpha} \left|\mathbf{H}_{R_j D_j}\right|^2}{I_{D_j}} \geq \theta_D\right) \\
&= \mathbb{P}\left(\left|\mathbf{H}_{R_j D_j}\right|^2 \geq \theta_D \tilde{\rho}^{-1} \tilde{R}_j^\alpha I_{D_j}\right).
\end{aligned} \tag{14}$$

Next, we provide the success probability analysis of the RD hop.

**Theorem 2.** *Let the relays transmission form a Poisson process of intensity  $\lambda_D$  around destinations. The success probability of the RD hop is*

$$P_{\text{suc}}^{(\text{RD})} \triangleq \sum_{n=0}^{N_d-1} \left[ \frac{(-s)^n}{n!} \frac{d^n}{ds^n} \mathcal{L}_{I_{D_j}}(s) \right]_{s=\theta_D \tilde{\rho}^{-1} \tilde{R}_j^\alpha}, \tag{15}$$

where  $\mathcal{L}_{I_{D_j}}$  is the Laplace transform of the interference  $I_{D_j}$ :

$$\mathcal{L}_{I_{D_j}}(s) \triangleq \Psi(s, \tilde{R}_j) \exp(-\lambda_D \Upsilon(s)), \tag{16}$$

where  $\Psi(s, r)$  and  $\Upsilon(s)$  are already defined in (13) and (12), respectively.

*Proof.* Refer to Appendix C.  $\square$

**Corollary 3.** *The Laplace transform in (16) is bounded by  $\mathcal{L}_{I_{D_j}}(s) \in [\mathcal{L}_{I_{D_j}}^{\text{min}}(s), \mathcal{L}_{I_{D_j}}^{\text{max}}(s)]$ , where*

$$\begin{aligned}
\mathcal{L}_{I_{D_j}}^{(\text{min})}(s) &\triangleq \frac{1}{1+s\hat{\rho}(\tilde{R}_j - \hat{R}_j)^{-1}} \exp(-\lambda \Upsilon^{(\text{max})}(s)), \\
\mathcal{L}_{I_{D_j}}^{(\text{max})}(s) &\triangleq \frac{1}{1+s\hat{\rho}(\tilde{R}_j + \hat{R}_j)^{-1}} \exp(-\lambda \Upsilon^{(\text{min})}(s)),
\end{aligned} \tag{17}$$

with  $\Upsilon^{(\text{min})}(s)$  and  $\Upsilon^{(\text{max})}(s)$  already being given in [21, 28] as follows:

$$\begin{aligned}
\Upsilon^{(\text{max})}(s) &\triangleq 2(\tilde{\rho} + \hat{\rho}) \frac{\pi^2 s^{2/\alpha}}{\alpha \sin(2\pi/\alpha)}, \\
\Upsilon^{(\text{min})}(s) &\triangleq \left(1 + \frac{2}{\alpha}\right) (\hat{\rho} + \tilde{\rho}) \frac{\pi^2 s^{2/\alpha}}{\alpha \sin(2\pi/\alpha)}.
\end{aligned} \tag{18}$$

This corollary will help us in proving the interference bound of success probability  $P_{\text{suc}}^{\text{RD}}$  of RD hop; this can be done by substituting  $\mathcal{L}_{I_{D_j}}(s) \in [\mathcal{L}_{I_{D_j}}^{\text{min}}(s), \mathcal{L}_{I_{D_j}}^{\text{max}}(s)]$  in (15).

**2.5. Ergodic Capacity.** The other performance measure is the ergodic capacity; the goal of FD relay is to increase the network capacity; for the relay served by source, the following theorems give the outage probability (CDF of SINR) and the SR hop capacity.

**Theorem 4.** *The probability that  $\text{SINR}_{R_j}$  falls below a given target level  $\theta_R$  is known as outage probability, which is the CDF of  $\text{SINR}_{R_j}$  of the SR hop denoted by  $Z_j(\theta_R) = \mathbb{P}\{\text{SINR}_{R_j} \leq \theta_R\}$  and given by*

$$Z_{R_j}(\theta_R) = 1 - \exp(-2\pi\lambda_S), \tag{19}$$

and similarly for the RD hop

$$Z_{R_j}(\theta_D) = 1 - \exp(-2\pi\lambda_R). \tag{20}$$

Hence, the SR hop capacity can be shown as

$$C_{S_j R_j} \triangleq \sum_{j=1}^{N_r} \log(1 + \theta_R) P_{\text{suc}}^{(\text{SR})} \tag{21}$$

and the RD hop capacity is

$$C_{R_j D_j} \triangleq \sum_{j=1}^{N_d} \log(1 + \theta_D) P_{\text{suc}}^{(\text{RD})}. \tag{22}$$

The total channel capacity is denoted by

$$C = \min \left( (C_{S_j R_j}), (C_{R_j D_j}) \right). \quad (23)$$

*Proof.* Refer to Appendix A.  $\square$

For the single-antenna case, the following corollary shows that the FD relay outperforms the HD relay in terms of capacity.

**Corollary 5.** Consider the SR hop where relay and destination nodes are having only single antenna  $N_r = N_d = 1$ . Letting  $s = \theta_R \bar{\rho}^{-1} \bar{R}^\alpha$ , the FD relay capacity is lower-bounded by

$$C_{S_j R_j} \triangleq \frac{2}{(1 + s\bar{\rho})} \exp(-\lambda_S Y^{(max)}(s)) \sum_{j=1}^{N_r} \log(1 + \theta_R); \quad (24)$$

on the other hand, the HD relay capacity is upper-bounded by

$$C_{S_j R_j}^{HD} \triangleq \exp\left(-\lambda_S \bar{\rho} \frac{2\pi^2 s^{2/\alpha}}{\alpha \sin(2\pi/\alpha)}\right) \sum_{j=1}^{N_r} \log(1 + \theta_R); \quad (25)$$

therefore,  $C_{S_j R_j} \geq C_{S_j R_j}^{HD}$  as long as the following condition holds:

$$\lambda_S \leq \frac{\alpha \sin(2\pi/\alpha)}{2\pi^2 s^{2/\alpha}} \log_2 \left( \frac{2}{1 + s} \right). \quad (26)$$

*Proof.* The proof is obtained by combining Corollary 3 and Theorem 2.  $\square$

It is evident that increasing the density  $\lambda_S$  beyond the threshold does not compensate for the additional RSI, even if we use twice the FD capacity; this is due to FD simultaneous transmission and reception. Hence, the HD relay is optimal in this case.

**2.6. Minimum Throughput Gain.** We demonstrate the feasibility of FD relay over its counterpart, the HD relay, for the SR hop capacity only, but similar approach can be applied to the RD hop as well since the total capacity follows (23). We define a performance metric called the minimum throughput gain, which shows the worst case FD relay performance over HD relay in terms of capacity as follows:

$$TG^{\min} \triangleq \frac{C_{S_j R_j}}{C_{S_j R_j}^{HD}}. \quad (27)$$

when  $TG > 1$ , the FD relay outperforms the HD relay.

### 3. Interference Cancellation

This section considers the interference cancellation at the MIMO receiving nodes, that is, for SR hop at the relay and for RD hop at the destination. We present a low complexity spatial interference cancellation scheme known as partial zero forcing (PZF) [29, 30]. During the SR hop and RD hop, PZF can be applied at the relay and destination to cancel  $K \leq N_r - 1$  and  $L \leq N_d - 1$  interferences, respectively, while using the remaining degree of freedom to boost the intended received signal.

**3.1. SR Hop: Canceling RSI and SRI.** It is beneficial to increase the capacity by canceling the interference (RSI and SRI) from nearby nodes in an interference-limited scenario. Let us denote the points of  $\{i, j\} \in \Phi$ , in an increasing order from the source, that is,  $\{\bar{R}_i \leq \bar{R}_{i+1}\}_{i=1}^{\infty}$ ; the relay applies PZF to cancel its  $K$  interference. From (3), the overall interference can be rewritten as

$$I_{R_j}(K) \triangleq \sum_{\substack{j \in \Phi \\ j > K}} \left( \bar{\rho} \bar{R}_j^{-\alpha} |\mathbf{H}_{S_j D_j}|^2 \right) + \left( \bar{\rho} |\mathbf{H}_{R_j}|^2 \right). \quad (28)$$

For the SR hop, with PZF at the relay, the success probability is given next.

**Theorem 6.** The success probability of the SR hop with PZF at the relay is

$$P_{suc}^{(SR)} \triangleq \sum_{n=0}^{N_r - K - 1} \left[ \frac{(-s)^n}{n!} \frac{d^n}{ds^n} \mathcal{L}_{I_{R_j}(K)}(s) \right]_{s=\theta_R \bar{\rho}^{-1} \bar{R}_j^\alpha}, \quad (29)$$

where  $\mathcal{L}_{I_{R_j}(K)}(s)$  is the Laplace transform of the interferences:

$$\mathcal{L}_{I_{R_j}(K)}(s) \triangleq \frac{1}{(1 + s\bar{\rho})} \mathbb{E}_{\Phi} \left[ \prod_{\substack{j \in \Phi \\ j \leq K}} \frac{1}{1 + s\bar{\rho} r^{-\alpha}} \right]. \quad (30)$$

*Proof.* See Appendix A and follow similar steps to those in [30].  $\square$

**3.2. RD Hop: Canceling SDI.** It is beneficial to increase the capacity by canceling the interference (SDI) from nearby nodes in an interference limited scenario. Let us denote the points of  $\{i, j\} \in \Phi$ , in an increasing order from the source, that is,  $\{\hat{R}_i \leq \hat{R}_{i+1}\}_{i=1}^{\infty}$ ; the destination applies PZF to cancel its  $L$  interference. From (6), the overall interference can be rewritten as

$$I_{D_j}(L) \triangleq \sum_{\substack{j \in \Phi \\ j > L}} \left( \hat{\rho} \hat{R}_j^{-\alpha} |\mathbf{H}_{S_j D_j}|^2 \right) \quad (31)$$

and its corresponding success probability is given below.

**Theorem 7.** The success probability of the RD hop with PZF at the destination is

$$P_{suc}^{(RD)} \triangleq \sum_{n=0}^{N_d - L - 1} \left[ \frac{(-s)^n}{n!} \frac{d^n}{ds^n} \mathcal{L}_{I_{D_j}(L)}(s) \right]_{s=\theta_D \hat{\rho}^{-1} \hat{R}_j^\alpha}, \quad (32)$$

where  $\mathcal{L}_{I_{D_j}(L)}(s)$  is the Laplace transform of the interferences:

$$\mathcal{L}_{I_{D_j}(L)}(s) \triangleq \frac{1}{(1 + s\hat{\rho})} \mathbb{E}_{\Phi} \left[ \prod_{\substack{j \in \Phi \\ j \leq L}} \frac{1}{1 + s\hat{\rho} r^{-\alpha}} \right]. \quad (33)$$

*Proof.* See Appendix A and follow similar steps as those in [30].  $\square$

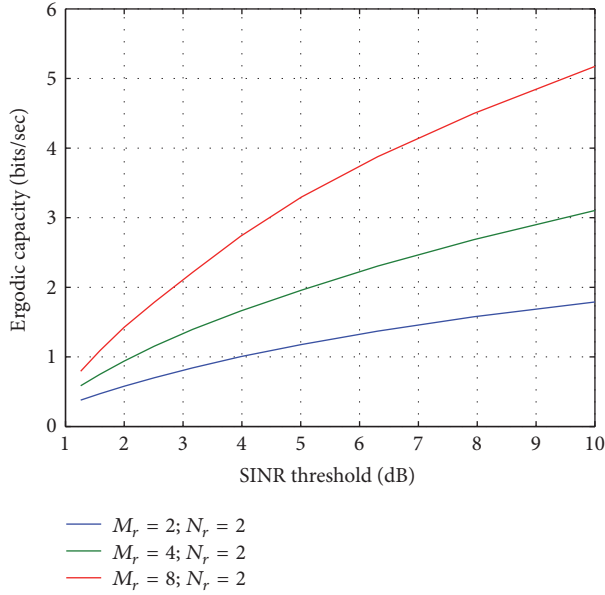


FIGURE 4: Ergodic capacity versus SINR threshold for different relay and destination transmitted and received antennas, respectively.

#### 4. Numerical Results

Several Monte Carlo simulations are presented to validate the proposed scheme and averaged over 10000 number of channel realizations. Rayleigh fading assumption results in a convenient coverage probability form in terms of the Laplace transform of the interference, which is easier to characterize than the probability density function of the interference [10]. The sources and relays are transmitting with  $\bar{p} = 1$  W and  $\hat{p} = 0.5$  W with their corresponding distances  $\bar{R} = 5$  m and  $\hat{R} = 0.5$  m, respectively. The SINR threshold is  $\theta = 0$  dB and the path-loss exponent is  $\alpha = 2.3$ , with 100 destination nodes, 100 source nodes, and 100 relay nodes, with  $N = 8$  interfering source and relay nodes. We assume that, in this open-access case, destinations (users) are able to connect to any source (base station). Open access requirements often are not satisfied, particularly deploying Wi-Fi in the multi-RAT (radio access technology) femtocells network [31].

Figure 4 shows the ergodic capacity in (23) of  $M_s = N_r = 2$ ,  $M_r = N_d = 2$  and  $M_s = N_r = 2$ ,  $M_r = N_d = 4$  and  $M_s = N_r = 2$ ,  $M_r = N_d = 8$ , antenna configurations. From (21) and (22) it is obvious that increasing the number of antennas employed at the relay and destination adds a positive term to the ergodic capacity; however, the total capacity is limited by the weakest hop (23). It can be observed that the ergodic capacity scales linearly with the number of antennas.

Figure 5 shows that the success probability in (7) increases with increasing the number of transmitting antennas at the source across the whole SINR. Deploying multiple antennas at the relay allows reducing the effect of interference, hence obtaining a substantial SINR gain. Figure 6 indicates that the success probability decreases with an increase in the SINR threshold. It compares the traditional grid model constituted by a Voronoi tessellation (see Figure 3) to the random PPP source model. Considering  $N = 8$  and  $N = 24$ , it can be

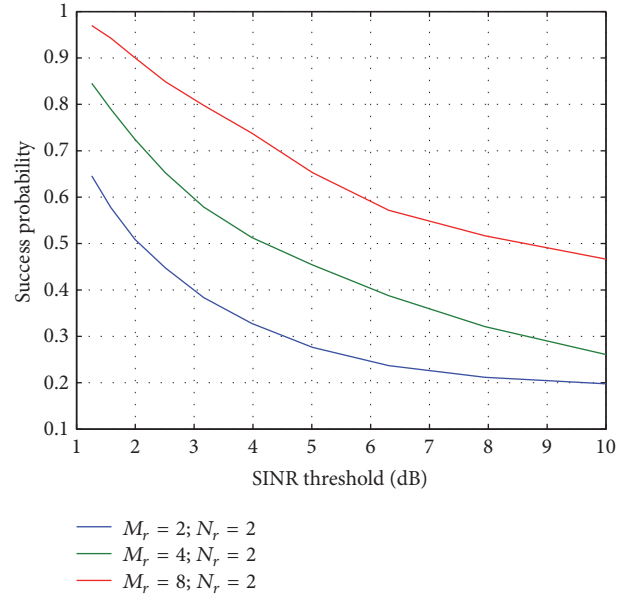


FIGURE 5: Success probability versus SINR threshold.

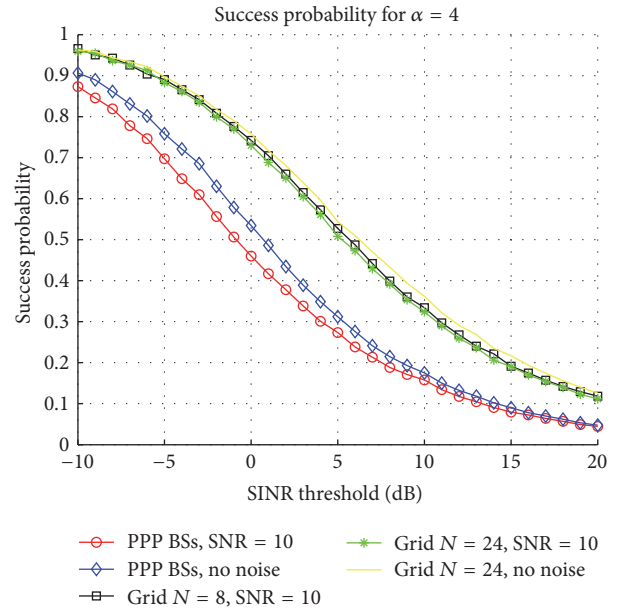


FIGURE 6: Success probability comparison between our proposed PPP source model and grid model with  $N = 8$  and  $N = 24$  and  $\alpha = 4$ . No noise assumption is quite correct, and it can be observed that the case with  $N = 24$  is slightly lower than  $N = 8$ .

observed that the case of  $N = 8$  is almost overlapped with  $N = 24$ , for  $\alpha = 4$ . As expected, the grid model provides high coverage area across the whole SINR. A small gap has been observed when considering the SNR = 10 and SNR  $\rightarrow \infty$ , due to the noise effect in dense cellular networks, which are known to be interference-limited. This validates the assumption that the noise can be ignored in interference-limited scenario.

Figure 7 presents a crucial issue in FD relay communications by evaluating the performance of multiple receive

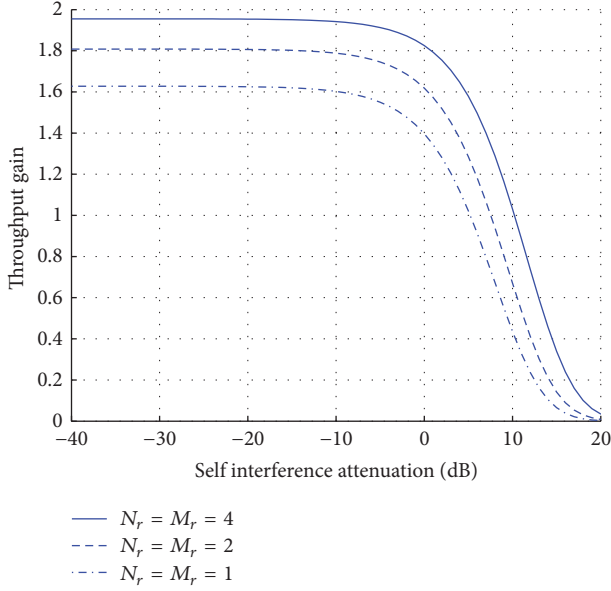


FIGURE 7: Comparison between FD and HD relay in the SR hop: minimum throughput gain for different values of self-interference attenuation with  $\lambda = 10^{-3}$  and  $\theta = 0$  dB.

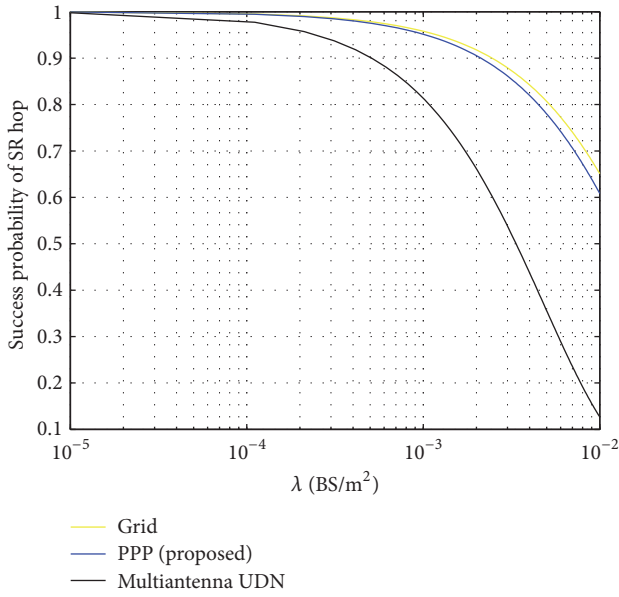


FIGURE 8: Success probability of the SR hop with interference cancellation versus the density  $\lambda$  with  $M_s = N_r = M_r = 2$  and SINR threshold  $\theta = 0$  dB for different schemes.

antennas in canceling the self-interference. The capacity gain is plotted against the self-interference attenuation with  $\theta = 0$  dB and  $\lambda = 10^{-3}$ . We observed that  $TG^{\min} > 1$ , even for moderate self-interference attenuation values  $\leq 4$ ,  $\leq 8$ , and  $\leq 10$  dBs for  $N_r = M_r = 1$ ,  $N_r = M_r = 2$ , and  $N_r = M_r = 4$ , respectively.

For the SR hop, the relays are equipped with two receive antennas  $N_r = 2$  and deploy PZF to cancel either the RSI or the SRI. Figure 8 shows the success probability of the SR hop

against the density  $\lambda$  and compares it with the multiantenna UDN model [30] and the grid model. Note that the grid model is best suited for higher densities, whereas our proposed model performs slightly better than the multiantenna UDN model, due to the use of both antennas at source and relay for array gain to exploit the MIMO capability in boosting the intended received signal.

## 5. Conclusion

In a MIMO relay cellular network, RSI, SRI, and SDI will likely be the main obstacle reducing the capacity. This paper, however, developed a tractable model to analyze the success probability and ergodic capacity expressions for the random nodes, using tools from stochastic geometry. It is more realistic than the grid-based models and requires an extensive comparison with real base station deployments to validate its accuracy. We showed the effect of PZF in mitigating the interferences including the self-interference to demonstrate the feasibility of FD technology even for moderate values of self-interference attenuation. Future work probably uses this model extensively due to the interference modeling from neighboring nodes.

## Appendix

### A.

Assume that the typical source is located at the origin  $\mathbf{o}$ , since the relay always chooses its nearest source to access; the cumulative density function (CDF) of  $\tilde{R}_j$  is obtained by

$$\mathbb{P}\{\tilde{R}_j > \bar{R}_j\} = 1 - \mathbb{P}\{\text{no source closer than } \bar{R}_j\} = 1 - e^{-\lambda_s \pi \bar{R}_j^2}. \quad (\text{A.1})$$

Then, the probability density function (PDF) of  $\tilde{R}_j$  is  $f(\tilde{R}_j) = e^{-\lambda_s \pi \tilde{R}_j^2} 2\pi \lambda_s \tilde{R}_j$  as obtained SINR in (2). The CDF of SINR regarding  $I_{R_j}$  is given by

$$\begin{aligned} Z_{R_j}(\theta) &= 1 - \mathbb{E}\left[\mathbb{P}\{\text{SINR}_{R_j} > \theta_R\}\right] \\ &= 1 - \int_0^\infty 2\pi \lambda_s \tilde{R}_j e^{-\pi \lambda_s \tilde{R}_j^2} \mathbb{P}\left\{\frac{\tilde{\rho} \tilde{R}_j^{-\alpha} |\mathbf{H}_{S_j R_j}|^2}{I_{R_j} + \sigma_j^2} > \theta_R\right\} d\tilde{R}_j \\ &= 1 - \int_0^\infty 2\pi \lambda_s \tilde{R}_j e^{-\pi \lambda_s \tilde{R}_j^2} \mathbb{P}\left\{|\mathbf{H}_{S_j R_j}|^2 > \frac{\theta_R \tilde{R}_j^\alpha}{\tilde{\rho}} (I_{R_j} + \sigma_j^2)\right\} d\tilde{R}_j. \end{aligned} \quad (\text{A.2})$$

Using the fact that  $|\mathbf{H}_{S_j R_j}|^2 = \sum_{j=1}^{M_s} |h_{S_j R_j}|^2$  with  $h \sim \exp(1)$  simplifies to

$$\begin{aligned} &= 1 - \int_0^\infty 2\pi\lambda_s \tilde{R}_j e^{-\pi\lambda_s \tilde{R}_j^2} \mathbb{E} \left\{ e^{-(\theta \tilde{R}_j^{-\alpha} / \tilde{\rho})(I_{R_j} + \sigma_{R_j}^2)} \right\} d\tilde{R}_j \\ &= 1 - \int_0^\infty 2\pi\lambda_s \tilde{R}_j e^{-\pi\lambda_s \tilde{R}_j^2 - (\theta \tilde{R}_j^{-\alpha} \sigma_{R_j}^2 / \tilde{\rho})} \mathcal{L}_{R_j} \left( \frac{\theta \tilde{R}_j^{-\alpha}}{\tilde{\rho}} \right) d\tilde{R}_j. \end{aligned} \quad (\text{A.3})$$

Now, Let us evaluate the Laplace transform for the interference  $\mathcal{L}_{R_j}(s)$  building on the fact that the typical relay is served by the nearest source with distance  $\tilde{R}_j$ . Firstly, the Laplace transform of the interference of relay can be obtained by following the same steps as in [10, Page 125]:

$$\mathcal{L}_{I_{R_j}}(s) = \mathbb{E} \left\{ \exp \left( -s \frac{\hat{\rho}}{N_r} \sum_{i \in \Phi \setminus \{j\}} |\mathbf{H}_{R_j}|^2 \right) \right\}. \quad (\text{A.4})$$

Using the fact that  $|\mathbf{H}_{R_j}|^2 = \sum_{j=1}^{M_r} |h_{R_j}|^2$  with  $h \sim \exp(1)$  simplifies to

$$\begin{aligned} &= \mathbb{E} \left( \prod_{\{i\} \in \Phi \setminus \{j\}} \mathbb{E}_{g_j} \left\{ \exp \left( -s \frac{\rho}{N_r} g_j \right) \right\} \right) \\ &= \mathbb{E} \left( \prod_{\{i\} \in \Phi \setminus \{j\}} \frac{1}{1 + (s(\hat{\rho}/N_r))} \right). \end{aligned} \quad (\text{A.5})$$

Applying the probability generating functional of PPP  $\Phi$  with intensity  $\lambda$  for function  $v(x)$  [32]:

$$\mathbb{E} [\prod_{x \in \Phi} v(x)] = \exp \left( -\lambda \int_{\mathbb{R}^2} (1 - v(x)) dx \right). \quad (\text{A.6})$$

Applying the probability generating function to  $\mathcal{L}_{I_{R_j}}$  yields

$$= \exp \left( -2\pi\lambda_s \int_{\tilde{R}}^\infty \left( 1 - \frac{1}{1 + (sx)} \right) x dx \right) \quad (\text{A.7})$$

$$\begin{aligned} \mathcal{L}_{I_{R_j}} &= \exp \left( -2\pi\lambda_s \int_{\tilde{R}}^\infty \left( 1 - \frac{1}{1 + ((\theta \tilde{R}_j^{-\alpha} / \tilde{\rho}) x)} \right) \right. \\ &\quad \left. \cdot x dx \right) \end{aligned} \quad (\text{A.8})$$

$$\begin{aligned} \mathcal{L}_{I_{D_j}} &= \exp - \left( 2\pi\lambda_r \int_{\hat{R}}^\infty \left( 1 - \frac{1}{1 + ((\theta \hat{R}_j^{-\alpha} / \hat{\rho}) x)} \right) \right. \\ &\quad \left. \cdot x dx \right). \end{aligned} \quad (\text{A.9})$$

Plugging (A.8) into (A.3) and assuming that the distance between  $\tilde{R}_j$  and  $\hat{R}_j$  is fixed, (19) and (20) are proven.

## B.

Let us define  $f_{I_{R_j}}(t) = d\mathbb{P}(I_{R_j} \leq t)$  as the PDF of  $I_{R_j}$ . The integration of  $f_{I_{R_j}}(t)$  using the CCDF  $F_{SR}^c(t)$  transforms it as

$$g(s) = \int_0^\infty F_{SR}^c(st) f_{I_{R_j}}(t) dt. \quad (\text{B.1})$$

Note that the power of desired signal is distributed as  $|\mathbf{H}_{S_j R_j}|^2 \sim \chi_{2N_r}^2$ ; the probability of success is given by

$$\begin{aligned} \mathbb{P}(\text{SINR}_{R_j} \geq \theta_R) &= \mathbb{P} \left( |\mathbf{H}_{S_j R_j}|^2 \geq \theta_R \tilde{\rho}^{-1} \tilde{R}^\alpha I_{R_j} \right) \\ &= \int_0^\infty F_{SR}^c(st) f_{I_{R_j}}(t) dt \\ &= g(s) \Big|_{s=\theta_R \tilde{\rho}^{-1} \tilde{R}^\alpha}. \end{aligned} \quad (\text{B.2})$$

Assume that  $F_{SR}^c(t) = e^{-t}$  and, using Laplace transform, the success probability can be expressed using the transformation of  $f_{I_{R_j}}(t)$ :

$$\begin{aligned} g(s) &= \int_0^\infty F_{SR}^c(st) f_{I_{R_j}}(t) dt = \mathcal{L} \left\{ f_{I_{R_j}}(t) \right\} (s) \\ &= \mathcal{L}_{I_{R_j}}(s). \end{aligned} \quad (\text{B.3})$$

Finally, using the CCDF  $F_{SR}^c(t) = \sum_n e^{-nt} \sum_j a_n t^j$ , the transformation of  $f_{I_{R_j}}(t)$  is given by

$$g(s) = \int_0^\infty F_{SR}^c(st) f_{I_{R_j}}(t) dt \quad (\text{B.4})$$

$$= \int_0^\infty \left( \sum_n e^{-nst} \sum_j a_{nj} (st)^j \right) f_{I_{R_j}}(t) dt$$

$$= \sum_n \sum_j a_{nj} s^j \left( \int_0^\infty e^{-nt} t^j f_{I_{R_j}}(t) dt \right) \quad (\text{B.5})$$

$$= \sum_n \sum_j a_{nj} s^j \mathcal{L} \left\{ t^j f_{I_{R_j}}(t) \right\} (ns) \quad (\text{B.6})$$

$$= \sum_n \sum_j \left[ a_{nj} (-s)^j \frac{d^j}{d(ns)^j} \mathcal{L}_{I_{R_j}}(ns) \right] \quad (\text{B.7})$$

$$= \sum_n \sum_j \left[ a_{nj} \left( -\frac{s}{n} \right)^j \frac{d^j}{d(ns)^j} \mathcal{L}_{I_{R_j}}(ns) \right]_{ns=n\theta \tilde{\rho}^{-1} \tilde{R}^\alpha}, \quad (\text{B.8})$$

where (B.6) is obtained by using Laplace transform property  $t^n f(t) \longleftrightarrow (-1)^n (d^n/ds^n) \mathcal{L}\{f(t)\}(s)$ . Apply the moment-generating function of  $x_2$  and Gamma distribution to [211, Theorem 1] to reach (11).

## C.

The success probability of the RD hop is shown as follows:

$$\mathbb{P}(\text{SINR}_{D_j} \geq \theta_D) = \mathbb{P} \left( |\mathbf{H}_{R_j D_j}|^2 \geq \theta_D \hat{\rho}^{-1} \hat{R}_j^\alpha I_{D_j} \right), \quad (\text{C.1})$$

where  $I_{D_j}$  is defined in (6). The desired signal is distributed as  $|\mathbf{H}_{R_j D_j}|^2 \sim \chi_{2M_r}^2$ ; the proof of (15) is similar to Theorem 1. On the other hand, again we use the moment-generating function of  $\chi_2^2$  distribution to provide the Laplace transform of  $I_{D_j}$  [10, Page 125] and resort to

$$\begin{aligned} \mathcal{L}_{I_{D_j}}(s) &= \mathbb{E} \left( \prod_{(i,j) \in \Phi} \mathbb{E} \left\{ \exp \left( -s \frac{\hat{P}}{N_d} \hat{R}^{-\alpha} |\mathbf{H}_{R_j D_j}|^2 \right) \right\} \right). \end{aligned} \quad (\text{C.2})$$

Hence, we prove (16).

## Conflicts of Interest

The authors declare that they have no conflicts of interest.

## References

- [1] C.-X. Wang, F. Haider, X. Gao et al., "Cellular architecture and key technologies for 5G wireless communication networks," *IEEE Communications Magazine*, vol. 52, no. 2, pp. 122–130, 2014.
- [2] T. S. Rappaport, R. W. Heath Jr., R. C. Daniels, and J. N. Murdock, *Millimeter Wave Wireless Communications*, Pearson Education, London, UK, 2014.
- [3] Y. Hua, "An overview of beamforming and power allocation for MIMO relays," in *Proceedings of the IEEE Military Communications Conference (MILCOM '10)*, pp. 375–380, San Jose, Calif, USA, November 2010.
- [4] T. Riihonen, S. Werner, and R. Wichman, "Residual self-interference in full-duplex MIMO relays after null-space projection and cancellation," in *Proceedings of the 44th Asilomar Conference on Signals, Systems and Computers (Asilomar 10)*, pp. 653–657, Pacific Grove, Calif, USA, November 2010.
- [5] D. W. Bliss, P. A. Parker, and A. R. Margetts, "Simultaneous transmission and reception for improved wireless network performance," in *Proceedings of the IEEE/SP 14th WorkShoP on Statistical Signal Processing (SSP '07)*, pp. 478–482, Madison, Wis, USA, August 2007.
- [6] Z. Zhou and X. Zhang, "Directional antenna-based single channel full duplex," *IET Communications*, vol. 9, no. 16, pp. 1999–2006, 2015.
- [7] G. C. Alexandropoulos, M. Kountouris, and I. Atzeni, "User scheduling and optimal power allocation for full-duplex cellular networks," in *Proceedings of the 17th IEEE International Workshop on Signal Processing Advances in Wireless Communications (SPAWC '16)*, Edinburgh, UK, July 2016.
- [8] J. Xu, J. Zhang, and J. G. Andrews, "On the accuracy of the wyner model in cellular networks," *IEEE Transactions on Wireless Communications*, vol. 10, no. 9, pp. 3098–3109, 2011.
- [9] R. Bhagavatula and J. Heath, "Adaptive bit partitioning for multicell intercell interference nulling with delayed limited feedback," *IEEE Transactions on Signal Processing*, vol. 59, no. 8, pp. 3824–3836, 2011.
- [10] M. Haenggi, *Stochastic Geometry for Wireless Networks*, Cambridge University Press, Cambridge, UK, 2012.
- [11] J. G. Andrews, F. Baccelli, and R. K. Ganti, "A tractable approach to coverage and rate in cellular networks," *IEEE Transactions on Communications*, vol. 59, no. 11, pp. 3122–3134, 2011.
- [12] B. Błaszczyszyn, M. K. Karray, and H. P. Keeler, "Wireless networks appear poissonian due to strong shadowing," *IEEE Transactions on Wireless Communications*, vol. 14, no. 8, pp. 4379–4390, 2015.
- [13] H. P. Keeler, N. Ross, and A. Xia, "When do wireless network signals appear poisson?" <https://arxiv.org/abs/1411.3757>.
- [14] H. S. Dhillon, R. K. Ganti, and J. G. Andrews, "A tractable framework for coverage and outage in heterogeneous cellular networks," in *Proceedings of the Information Theory and Applications Workshop (ITA '11)*, pp. 361–366, La Jolla, Calif, USA, February 2011.
- [15] H. S. Dhillon, R. K. Ganti, F. Baccelli, and J. G. Andrews, "Modeling and analysis of K-tier downlink heterogeneous cellular networks," *IEEE Journal on Selected Areas in Communications*, vol. 30, no. 3, pp. 550–560, 2012.
- [16] H. S. Dhillon, M. Kountouris, and J. G. Andrews, "Downlink coverage probability in MIMO HetNets," in *Proceedings of the 46th Asilomar Conference on Signals, Systems and Computers (ASILOMAR '12)*, pp. 683–687, Pacific Grove, Calif, USA, November 2012.
- [17] J. N. Laneman, D. N. Tse, and G. Wornell, "Cooperative diversity in wireless networks: efficient protocols and outage behavior," *IEEE Transactions on Information Theory*, vol. 50, no. 12, pp. 3062–3080, 2004.
- [18] J. N. Laneman and G. W. Wornell, "Distributed space-time coded protocols for exploiting cooperative diversity in wireless networks," *IEEE Transactions on Information Theory*, vol. 49, no. 10, pp. 2415–2425, 2003.
- [19] M. Duarte, C. Dick, and A. Sabharwal, "Experiment-driven characterization of full-duplex wireless systems," *IEEE Transactions on Wireless Communications*, vol. 11, no. 12, pp. 4296–4307, 2012.
- [20] C. Psomas, M. Mohammadi, I. Krikidis, and H. A. Suraweera, "Impact of directionality on interference mitigation in full-duplex cellular networks," *IEEE Transactions on Wireless Communications*, vol. 16, no. 1, pp. 487–502, 2017.
- [21] Z. Tong and M. Haenggi, "Throughput analysis for wireless networks with full-duplex radios," in *Proceedings of the IEEE Wireless Communications and Networking Conference (WCNC '15)*, pp. 717–722, New Orleans, La, USA, March 2015.
- [22] J. Lee and T. Q. S. Quek, "Hybrid full-/half-duplex system analysis in heterogeneous wireless networks," *IEEE Transactions on Wireless Communications*, vol. 14, no. 5, pp. 2883–2895, 2015.
- [23] M. Mohammadi, H. A. Suraweera, Y. Cao, I. Krikidis, and C. Tellambura, "Full-duplex radio for uplink/downlink wireless access with spatially random nodes," *IEEE Transactions on Communications*, vol. 63, no. 12, pp. 5250–5266, 2015.
- [24] D. Gesbert, S. Hanly, H. Huang, S. Shamai Shitz, O. Simeone, and W. Yu, "Multi-cell MIMO cooperative networks: a new look at interference," *IEEE Journal on Selected Areas in Communications*, vol. 28, no. 9, pp. 1380–1408, 2010.
- [25] S. Goyal, P. Liu, S. Hua, and S. Panwar, "Analyzing a full-duplex cellular system," in *Proceedings of the 47th Annual Conference on Information Sciences and Systems (CISS '13)*, pp. 1–6, IEEE, Baltimore, Md, USA, March 2013.
- [26] H. Huang and S. Venkatesan, "Asymptotic downlink capacity of coordinated cellular networks," in *Proceedings of the Conference Record of the Thirty-Eighth Asilomar Conference on Signals, Systems and Computers*, pp. 850–855, Pacific Grove, Calif, USA, November 2004.

- [27] T. D. Novlan, H. S. Dhillon, and J. G. Andrews, "Analytical modeling of uplink cellular networks," *IEEE Transactions on Wireless Communications*, vol. 12, no. 6, pp. 2669–2679, 2013.
- [28] Z. Gong and M. Haenggi, "Interference and outage in mobile random networks: expectation, distribution, and correlation," *IEEE Transactions on Mobile Computing*, vol. 13, no. 2, pp. 337–349, 2014.
- [29] N. Jindal, J. G. Andrews, and S. Weber, "Rethinking MIMO for wireless networks: Linear throughput increases with multiple receive antennas," in *Proceedings of the IEEE International Conference on Communications (ICC '09)*, Dresden, Germany, June 2009.
- [30] I. Atzeni and M. Kountouris, "Performance analysis of partial interference cancellation in multi-antenna UDNs," in *Proceedings of the 50th Asilomar Conference on Signals, Systems and Computers (ACSSC '16)*, pp. 699–703, Pacific Grove, Calif, USA, November 2016.
- [31] S. Singh, H. S. Dhillon, and J. G. Andrews, "Offloading in heterogeneous networks: modeling, analysis, and design insights," *IEEE Transactions on Wireless Communications*, vol. 12, no. 5, pp. 2484–2497, 2013.
- [32] S. N. Chiu, D. Stoyan, W. S. Kendall, and J. Mecke, *Stochastic Geometry and Its Applications*, John Wiley & Sons, Hoboken, NJ, USA, 2013.

## Research Article

# Combined Sector and Channel Hopping Schemes for Efficient Rendezvous in Directional Antenna Cognitive Radio Networks

AbdulMajid M. Al-Mqdashi,<sup>1</sup> A. Sali,<sup>1</sup> Nor K. Noordin,<sup>1</sup>  
Shaiful J. Hashim,<sup>1</sup> and Rosdiadee Nordin<sup>2</sup>

<sup>1</sup>Wireless and Photonic Networks Research Centre of Excellence (WiPNet), Department of Computer and Communication Systems Engineering, Faculty of Engineering, Universiti Putra Malaysia, 43400 Serdang, Selangor, Malaysia

<sup>2</sup>Department of Electrical, Electronic, and Systems Engineering, Universiti Kebangsaan Malaysia, 43600 Bangi, Selangor, Malaysia

Correspondence should be addressed to AbdulMajid M. Al-Mqdashi; [abdulmajid.almqdashi@gmail.com](mailto:abdulmajid.almqdashi@gmail.com)

Received 27 August 2017; Accepted 24 October 2017; Published 12 December 2017

Academic Editor: Ahmed M. Al-Samman

Copyright © 2017 AbdulMajid M. Al-Mqdashi et al. This is an open access article distributed under the Creative Commons Attribution License, which permits unrestricted use, distribution, and reproduction in any medium, provided the original work is properly cited.

Rendezvous is a prerequisite and important process for secondary users (SUs) to establish data communications in cognitive radio networks (CRNs). Recently, there has been a proliferation of different channel hopping- (CH-) based schemes that can provide rendezvous without relying on any predetermined common control channel. However, the existing CH schemes were designed with omnidirectional antennas which can degrade their rendezvous performance when applied in CRNs that are highly crowded with primary users (PUs). In such networks, the large number of PUs may lead to the inexistence of any common available channel between neighboring SUs which result in a failure of their rendezvous process. In this paper, we consider the utilization of directional antennas in CRNs for tackling the issue. Firstly, we propose two coprimality-based sector hopping (SH) schemes that can provide efficient pairwise sector rendezvous in directional antenna CRNs (DIR-CRNs). Then, we propose an efficient CH scheme that can be combined within the SH schemes for providing a simultaneous sector and channel rendezvous. The guaranteed rendezvous of our schemes are proven by deriving the theoretical upper bounds of their rendezvous delay metrics. Furthermore, extensive simulation comparisons with other related rendezvous schemes are conducted to illustrate the significant outperformance of our schemes.

## 1. Introduction

The inefficiency of radio spectrum utilization due to the fixed assignment of spectrum bands, coupled with the huge increase in the number of wireless devices recently, leads to the emerging of cognitive radios (CRs). CRs have been introduced as an efficient solution for the spectrum scarcity issue. They allow unlicensed users, also known as secondary users (SUs), to opportunistically use licensed bands as long as this use does not create any interference to the bands licensed users, that is, primary users (PUs). In distributed CRNs, SUs need to meet each other on a common channel and exchange control messages in order to set up their data transmissions [1]. This operation is called *rendezvous*, which is a fundamental and a vital process for initiating the connection of the SUs data communications.

The use of a dedicated common control channel (CCC) is one widely adopted rendezvous approach in the literature [2–6]. Although this approach can simplify the rendezvous process, it has many drawbacks such as the CCC susceptibility to long-time blocking by PUs, early saturation by SUs, or jamming by attackers [7, 8]. Moreover, the spectrum heterogeneity among SUs, caused by the spatial and temporal variations of the spectrum opportunities (influenced by neighboring PU activities), makes this approach not practical. Therefore, channel hopping (CH) has been proposed as an alternative approach for rendezvous without the need for any predefined CCC. The existing CH-based rendezvous schemes were designed with omnidirectional antenna according to different mathematical structures (e.g., [9–18]) in order to provide a successful channel rendezvous between a pair of single-hop SUs. In the CH approach, each SU generates its CH sequence

based on the available channels that are sensed to be idle from any PU activities within its omnidirectional range. Then, the SU keeps hopping over the channels according to the generated CH sequence for achieving channel rendezvous. The rendezvous occurs between a pair of communicating SUs when they hop during the same time slot over a channel that is commonly available for both of them. The existence of common available channels (at least one) between the pair of communicating SUs is a common and essential assumption made by all the existing CH schemes. Their designs rely mainly on this assumption to take place for ensuring the success of the rendezvous operation. However, none of the existing CH rendezvous designs were tailored for high-density PU networks, where the number of active PUs in the network is larger than the number of the channels. In such networks, the channel availabilities may vary dramatically among the SUs within the single-hop rendezvous region itself. This can lead to the inexistence of any common available channel between a pair of SUs and hence the failure of the rendezvous process.

One approach to overcome this serious rendezvous problem is using directional antennas instead of the conventionally used omnidirectional ones [19]. Directional antennas have been utilized in emerging wireless networks such as the millimeter-wave (MMW) networks for providing highly reliable transmission and multi-Gigabit data rates. This is mainly due to their capabilities in enlarging the transmission range and limiting the interference [20, 21]. However, in CRNs, equipping SUs with directional antennas for channel rendezvous can bring about many advantages. First of all, it allows SUs to transmit their rendezvous messages towards specific directions which can reduce the amount of interference to the PUs in the network as compared with the omnidirectional antennas. This is because the transmission of the SU that is equipped with directional antenna is directed to a particular region which can only cause interference to those PUs that are within this region. On the contrary, when using the omnidirectional antennas, the transmission of the SU is scattered towards all the directions. Thus, it can cause interference to all the surrounding PUs within the SU transmission range. Second, as related to the interference restriction imposed by the CR concept, SUs can use only the channels that are idle from any PU activities within their transmission range. According to that and due to its directed transmission range, using directional antenna will increase the number of available channels that can be utilized by the SU in each of its transmission sectors. As a consequence, the probability for any pair of neighbouring SUs to have at least a common available channel within their crossed sectors is high regardless of the number of PUs in the CRN. Note that, in omnidirectional antennas, this probability could be less than 0.1 for some scenarios when the number of PUs is larger than the network channels [19]. Increasing the probability of existing common available channel between the SUs will significantly enhance the probability of successful channel rendezvous. Therefore, in this paper, we study the rendezvous problem in directional antenna CRNs where SUs are equipped with directional antennas.

While the use of directional antennas for channel rendezvous in CRNs can bring about the above-mentioned advantages, it also imposes some unique challenges. Among these challenges is the sector rendezvous which must be achieved in advance between the pair of communicating SUs before they can achieve channel rendezvous. Specifically, the SUs need to steer their antennas towards each other in order to communicate over their commonly available channels. This necessitates the design of a deterministic sector hopping (SH) scheme that can guarantee that any pair of neighbouring SUs will steer their antennas to the proper directions (i.e., towards each other) at a certain time instance. So, when the SH scheme is combined with a suitable and deterministic CH scheme, SUs can achieve successful sector and channel rendezvous simultaneously within a bounded time. However, since the SUs do not know the relative locations of each other as well as the available channels before they rendezvous, the combined sector and channel hopping (SCH) scheme should be designed in fully distributed manner without any prior information or synchronization. Designing such combined SCH schemes for achieving rendezvous in DIR-CRNs is intuitively more challenging as compared with the traditional omnidirectional antenna paradigm.

In spite of the existing research in the literature, there have been some papers that addressed the utilization of directional antennas in CRNs. However, most of the proposed works investigated issues other than the rendezvous issue such as sensing [22, 23], routing [24, 25], and connectivity [26, 27]. To the best of our knowledge, the works in [19, 28] are the only proposals that tackle the sector and channel rendezvous issue in DIR-CRNs. In [19], an efficient framework for beamforming was proposed to provide a pairwise sector and channel rendezvous in DIR-CRNs. However, the SH scheme in [19] is not a blind design, where it assumes that the receiver must have prior knowledge of the sender number of sectors in order to achieve a successful sector rendezvous. This is not practical, since SUs do not know any information about each other before they rendezvous. On the other hand, Li and Xie in [28] proposed a blind prime-based SH scheme, where the number of sectors is adjusted to primes for achieving a guaranteed sector rendezvous. However, since the scheme relies on the coprimality between prime numbers only, the authors added an initiating rotated SH sequence on the sender side. This is in order to ensure a successful rendezvous with the receiver when the sender and the receiver construct their sequences with the same prime. Accordingly, the extra sequence overhead incurs extensively long sector rendezvous latency and hence a long time-to-rendezvous (TTR) will result when the SH is combined with a CH sequence. Furthermore, the SH schemes in [19, 28] are designed only for asymmetric-role environment, where SUs have preassigned role (i.e., SU is either a sender or receiver). However, this design limits the applications of the schemes; for example, SUs cannot work as a forwarder (i.e., receive packets from one SU and then forward them to another SU) due to the permanent role assignment [29]. Another drawback of these works is their limitations to provide a complete solution for combining the SH scheme with a suitable and efficient CH scheme which consider the unique traits of DIR-CRNs.

They claimed that their SH schemes can work on top of any existing deterministic CH schemes which were designed for the omnidirectional antennas paradigm. However, the combined CH scheme must be designed appropriately by taking into account the unique traits of DIR-CRNs such as the channels' qualities in the different sectors.

In this paper, we propose efficient schemes for achieving rendezvous in DIR-CRNs. The main contributions of this paper are summarized as follows:

- (i) We propose two asymmetric- and symmetric-role coprimality-based SH schemes, called PES-SH and IPES-SH, for pairwise sector rendezvous in DIR-CRNs.
- (ii) We combined our SH schemes with an efficient grid-quorum-based CH scheme, where the CH sequences are generated based on the best-quality channels in the sectors. The combined SCH schemes will provide guaranteed sector and channel rendezvous between the pair of SUs.
- (iii) We derive the upper bound of the rendezvous delay metrics for all of our schemes. Also, we conduct extensive simulations to study their performance under various network settings and compare them with the related existing works in [19, 28, 30].

The rest of this paper is organized as follows. The system model and problem formulation are presented in Section 2. The design and theoretical analysis of the proposed SH schemes are presented in Sections 3 and 4. In Section 5, we present the combined sector and channel hopping schemes. Using simulations, in Section 6, we evaluate the performance of our proposed schemes and compare their performance with other comparable schemes. Finally, we conclude the paper in Section 7.

## 2. Models and Problem Definition

In this section, we present the system model and rendezvous problem definition in DIR-CRNs.

*2.1. System Model.* We consider a CRN consisting of  $K$  SUs that coexist with several PUs in an  $w \times w$  area. There are totally  $L$  primary channels which can be accessed opportunistically by the SUs in order to communicate with each other. Each SU  $i \in K$  is equipped with a directional antenna with beamwidth  $\theta_i$  ( $0 < \theta_i < 2\pi$ ). Accordingly, the  $2\pi$  communication range of the SU  $i$  is divided into  $N_i = (2\pi/\theta_i)$  nonoverlapping sectors that are indexed from 1 to  $N_i$ . However, the number of sectors and the orientation of the sector indexing (i.e., either clockwise or anticlockwise) by each SU may be different from the others (see Figure 1). This is a very practical issue because each SU will configure its sectors based only on its own view to the surrounding environment. Each SU can transmit over any of its transmission sectors as long as it does not make any interference to any active PU transmission. Accordingly, we assume that the transmission sectors are also used as sensing sectors by which every SU can sense the appearance of the active PUs within them. Thus, the SU can obtain the channel

availability information per each sector. We consider a time-slotted communication, where time is divided into discrete slots that have fixed and equal durations. During each time slot, we assume that a SU can only transmit in one sector over a single channel.

*2.2. Definitions of Sector and Channel Rendezvous.* In this paper, we mainly focus on the pairwise sector and channel rendezvous between any pair of SUs in a DIR-CRN. Firstly, we define the sector rendezvous problem as follows.

*2.2.1. The Sector Rendezvous Problem.* For any two neighbour SUs (say  $SU_i$  and  $SU_j$ ) that are equipped with directional antennas and want to communicate with each other, assume that  $SU_i$  is located in the sector  $h_j \in [1, N_j]$  of  $SU_j$  and  $SU_j$  is situated in the sector  $h_i \in [1, N_i]$  of  $SU_i$ . The pair of the sectors  $(h_i, h_j)$  is called the sector rendezvous pair. SUs are said to achieve a successful sector rendezvous if and only if they steer their antennas towards each other, where their transmission sectors can cover each other. Formally, let  $S_i = \{S_i^0, S_i^1, \dots, S_i^{T_i}\}$  and  $S_j = \{S_j^0, S_j^1, \dots, S_j^{T_j}\}$  denote the sector hopping sequences for  $SU_i$  and  $SU_j$ , with periods  $T_i$  and  $T_j$ , respectively. Also let  $\delta$  denote the clock drift between  $SU_i$  and  $SU_j$  in the asynchronous scenario. The sector rendezvous problem can be formulated as follows:

If  $\forall \delta, \forall N_i, N_j, \exists t \in [0, T_i T_j - 1]$ , s.t.  $(S_i^t = h_i$  and  $S_j^{t+\delta} = h_j)$ , then the sector rendezvous is achieved over the sector rendezvous pair  $(h_i, h_j)$ .

*2.2.2. The Sector and Channel Rendezvous Problem.* When a SU steers its directional antenna to each sector of its transmission sectors, it performs CH over the available channels within the sector according to a CH sequence. This is in order to attempt channel rendezvous with another SU over a commonly available channel between them. The combined CH scheme should be designed in such a way that guarantees a successful channel rendezvous within bounded time whenever the communicating SUs already achieved a successful sector rendezvous. During the current sector, if the SU does not achieve channel rendezvous with its intended communicating SU within the bounded time slots, it then steers its antenna to the next sector of its SH sequence and executes the CH scheme based on the available channels within this sector.

One approach to view the problem is to look at it in a hierarchical way, in which time is divided into frames, where the SU tunes its antenna to one sector during each frame. In other words, the SH is implemented on the frame scale. Then, each frame is divided into number of time slots, where the combined CH sequence is executed (i.e., the CH is implemented on the time slot scale). The main goal of this paper is to design deterministic combined SCH scheme so as to tackle the sector and channel rendezvous problem.

*2.2.3. Metrics.* The proposed SH schemes as well as the combined SCH schemes will be evaluated according to the following metrics:

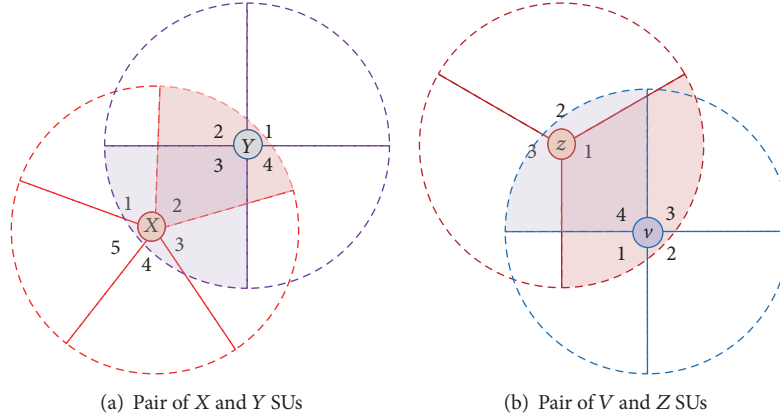


FIGURE 1: Examples of directional antenna configurations in two pairs of communicating SUs: (a)  $SU_X$  and  $SU_Y$  divide their transmission range into  $N_X = 5$  and  $N_Y = 4$  sectors; the rendezvous sector pair is (2, 3). (b)  $SU_V$  and  $SU_Z$  divide range into  $N_V = 4$  and  $N_Z = 3$  sectors; the rendezvous sector pair is (4, 1).

- (i) Sector rendezvous latency (SRL): it is defined as the required latency (in number of sector frames) for a pair of SUs to achieve sector rendezvous. We consider the maximum and average latency (MSRL/ASRL). MSRL is defined as the upper bound of the SRL between the SUs for all the possible clock drifts between them
- (ii) Time-to-rendezvous (TTR): it is defined as the required time (in number of time slots) for a pair of SUs to achieve sector and channel rendezvous simultaneously. Maximum and average time-to-rendezvous (MTTR/ATTR) are considered. MTTR means the required time for a guaranteed rendezvous even in the worst case.

### 3. Prime- and Even-Based Sequences Sector Hopping (PES-SH) Scheme

In this section, we propose an asymmetric-role SH scheme, called prime- and even-based sequences sector hopping (PES-SH) scheme, and then we analyze its theoretical performance.

**3.1. Scheme Design.** For ensuring a successful sector rendezvous between a pair of communicating SUs, the key for the deterministic design of our PES-SH scheme is to construct two SH sequences based on two coprime numbers. However, the coprimality is maintained between a pair of prime and even numbers that are relatively prime (i.e., coprime). In our PES-SH scheme, we assume that  $N_{\max}$  is a global variable known by all SUs, which indicates the maximum number of sectors by which any SU is allowed to divide its omnidirectional  $2\pi$  transmission range. The value of  $N_{\max}$  is obtained based on the number of channels in the network; for example, for  $L$  number of channels, the value of  $N_{\max}$  could be  $2 \times L$ . Accordingly, we consider two avoided sets:

- (1) The Avoided Prime Set (APS) which contains the primes  $\{2, 3\}$

- (2) The Avoided Even Set (AES) which contains any even number in the range  $[2, P_{\max}]$ , such that this even number is dividable by any prime number in the range  $[5, P_{\max}]$ .  $P_{\max}$  is the smallest prime not less than  $N_{\max}$ . For example, if  $N_{\max} = 20$ , then  $P_{\max} = 23$  and hence  $\text{AES} = \{10, 14, 20, 22\}$

The APS and AES sets are avoided by the sender and receiver, respectively, when they construct their SH sequences. Without loss of generality, assume that sender and receiver have  $N_s$  and  $N_r$  antenna sectors, respectively, where  $N_s, N_r \in [1, N_{\max}]$ . The main idea for the rendezvous of our PES-SH scheme is to let one SU (sender) adjust the number of its sectors to be the smallest prime number greater than  $N_s$ . On the other hand, the other SU (receiver) adjusts the number of its sectors to the smallest even number which is not smaller than  $N_r$  and not in the AES. Accordingly, the adjusted prime number of sectors for the sender and the adjusted even number of sectors for the receiver are guaranteed to be relatively prime.

Algorithms 1 and 2 are used by the sender and receiver, respectively, to construct each round of their SH sequences. The generating steps of the PES-SH sequences are as follows.

**3.1.1. Sender Sequence in PES-SH.** When a SU has data to transmit, it serves as a sender and hence generates a prime-based (PS-SH) sequence as follows. First, given the sector set  $S = \{1, \dots, N_s\}$ , randomly select a starting sector index  $i \in [1, N_s]$  and rotate  $S$  circularly starting from  $i$  as  $S = \text{rotate}(S, i - 1)$ . Second, adjust  $N_s$  to be the smallest prime number  $P_s$  which is not smaller than  $N_s$  and is not in the APS set (i.e.,  $P_s$  should be 5 when  $N_s < 5$ ). Third, construct each round of the PS sequence which has a length equal to  $P_s$  as follows: the  $k_{\text{th}}$  sector index of the PS round is  $S(k)$  if  $k \leq N_s$ ; otherwise the  $k_{\text{th}}$  sector is selected randomly form  $S$  when  $k > N_s$ . The sender will keep steering its antenna according to the PS sequence until it achieves sector rendezvous with its intended receiver.

Consider the cases for the sender SUs  $X$  and  $V$  in Figure 1;  $SU_X$  in Figure 1(a) has a prime number of sectors  $N_X = 5$ ,

**Input:**  $N_s, S_s$ .  
**Output:** a round  $\omega$  of the PS sequence for the sender  $s$ .  
(1) Find the smallest prime ( $P_s > 3$ ) that is not smaller than  $N_s$ .  
(2) **for**  $t = 0 : P_s - 1$  **do**  
(3)   **if**  $((t \bmod P_s) < N_s)$  **then**  
(4)      $\omega_s(t) = S_s(t + 1)$ .  
(5)   **else**  
(6)      $r$  is a random number  $\in [1, N_s]$   
(7)      $\omega_s(t) = S_s(r)$ .  
(8)   **end if**  
(9) **end for**  
(10) **return**  $\omega_s$ .

ALGORITHM 1: The sender SH generation algorithm (PS-SH).

**Input:**  $N_r, S_r, \text{AES}$ .  
**Output:** a round  $\gamma$  of the ES-SH sequence for the receiver  $r$ .  
(1) Find ( $E_r : E_r \notin \text{AES}$ ) as the smallest even number that is not smaller than  $N_r$ .  
(2) **for**  $t = 0 : E_r - 1$  **do**  
(3)   **if**  $((t \bmod E_r) < N_r)$  **then**  
(4)      $\gamma_r(t) = S_r(t + 1)$ .  
(5)   **else**  
(6)      $r$  is a random number  $\in [1, N_r]$   
(7)      $\gamma_r(t) = S_r(r)$ .  
(8)   **end if**  
(9) **end for**  
(10) **return**  $\gamma_r$ .

ALGORITHM 2: The receiver SH generation algorithm (ES-SH).

where  $S_x = \{1, 2, \dots, 5\}$  is not rotated. Then the first round of the PS<sub>X</sub> SH sequence with a length 5 is [1 2 3 4 5]. This round is repeated many times, where SU<sub>X</sub> continues steering its directional antenna into its sectors as shown in Figure 2(a) to achieve sector rendezvous with its receiver SU<sub>Y</sub>. On the other hand, the sender SU<sub>V</sub> in Figure 1(b) has  $N_V = 4$  number of sectors, so it selects  $P_V = 5$  as the smallest prime which is larger than  $N_V$ .  $S_V$  is rotated to start from 3 and hence  $S_V = \{3, 4, 2, 1\}$ . Then the first round of the PS<sub>V</sub> SH sequence which has adjusted length equal to  $P_V = 5$  is [3 4 2 1  $r$ ], where  $r$  indicates a randomly selected sector from  $S_V$ . The PS<sub>V</sub> SH sequence is constructed as many rounds as shown in Figure 2(b), where SU<sub>V</sub> keeps hopping on its sectors to achieve sector rendezvous with the receiver SU<sub>Z</sub>.

**3.1.2. Receiver Sequence in PES-SH.** If a SU has nothing to transmit, it serves as a receiver and generates an even-based (ES-SH) sequence as follows. First, randomly select a starting sector index  $j \in [1, N_r]$  and circularly rotate the sector set  $S = \{1, \dots, N_r\}$  starting from  $j$  as  $S = \text{rotate}(S, j - 1)$ . Second, adjust  $N_r$  to be the smallest even number  $E_r$  which is not smaller than  $N_r$  and is not in the Avoided Even Set (AES). Finally, construct each round of the ES sequence which has a

length equal to  $E_r$  as follows: the  $k_{\text{th}}$  sector index of the ES-SH round is  $S(k)$  if  $k \leq N_r$ ; otherwise the  $k_{\text{th}}$  sector is selected randomly from  $S$ .

Consider the receiver SU<sub>Y</sub> in Figure 1(a) which has an even number of sectors  $N_Y = 4$  which is not in AES and does not rotate its  $S_Y$  set. The round of the ES<sub>Y</sub> SH sequence with a length 4 is [1 2 3 4]. This round is repeated many times by SU<sub>Y</sub> in order to be paired by a sender as shown in Figure 2(a). On the other hand, the receiver SU<sub>Z</sub> in Figure 1(b) has  $N_Z = 3$  sectors; hence it finds  $E_Z = 4$  as the smallest even number larger than  $N_Z$  and not in AES. SU<sub>Z</sub> rotates its  $S_Z$  to start from sector 2 and hence  $S_Z = \{2, 3, 1\}$ . Accordingly, a round of the ES<sub>Z</sub> SH sequence with a length adjusted to  $E_Z = 4$  is [2 3 1  $r$ ], where  $r$  is a randomly selected sector from  $S_Z$ . The ES<sub>Z</sub> SH sequence is constructed in rounds as shown in Figure 2(b).

**3.2. Scheme Analysis.** In this subsection, we study the theoretical performance of the PES-SH, where the MSRL between any two arbitrary SUs performing the PES-SH is derived.

**Theorem 1.** *The MSRL under the PES-SH scheme is  $(P_s E_r)$ , where  $P_s$  and  $E_r$  denote the adjusted prime and even numbers of the sectors for the sender and receiver SUs, respectively.*

*Proof.* Suppose that the sector rendezvous pair is  $(h_s, h_r) \in \{1, 2, \dots, N_s\} \times \{1, 2, \dots, N_r\}$ , where  $\times$  here indicates the Cartesian product of the two SUs sectors sets. Without loss of generality, we assume that  $P_s < E_r$ . Also, we assume that the receiver SU<sub>r</sub> starts its SH sequence with  $\delta$  sector slots earlier than the start of the sender SU<sub>s</sub>. Accordingly, in each PS-SH period of SU<sub>s</sub>, the ES-SH sequence of SU<sub>r</sub> is  $\text{rotate}(ES_r, \delta)$ . In the first round of the SH, when the sender SU<sub>s</sub> is on its  $h_s$  sector, the receiver SU<sub>r</sub> is on the  $(u_1 = u_0 \bmod E_r + 1)$  sector, where  $1 \leq u_0 \leq N_r$ . During the subsequent  $E_r - 1$  rounds, while the sender SU is on its  $h_s$  sector, the receiver SU<sub>r</sub> must be sequentially on  $u_2 = ((u_0 + P_s) \bmod E_r + 1)$ ,  $u_3 = ((u_0 + 2P_s) \bmod E_r + 1), \dots, u_{E_r} = ((u_0 + (E_r - 1)P_s) \bmod E_r + 1)$ . As  $P_s$  and  $E_r$  are relatively prime, it can be easily proven with the help of the Chinese Remainder Theorem [31] that these  $u_1, u_2, \dots, u_{E_r}$  sectors where the receiver resides in the  $E_r$  rounds are all different. Hence, there must exist a sector among them which is equal to  $h_r$ . According to that and since every round of the PS-SH contains  $P_s$  sector hops, the SRL required to guarantee a sector rendezvous is upper bound by  $P_s E_r$ .  $\square$

## 4. Interleaved Prime- and Even-Based Sequences Sector Hopping (IPES-SH) Scheme

In the previous section, the PES-SH scheme was designed using the asymmetric approach which requires that each SU have a preassigned role as either a sender or a receiver. In this section, we introduce our interleaved prime- and even-based sequences (IPES-SH) scheme, which is symmetric (i.e., no preassigned role assumption).

**4.1. Scheme Design.** In our symmetric IPES-SH scheme, every SU generates its SH sequence with the help of a binary

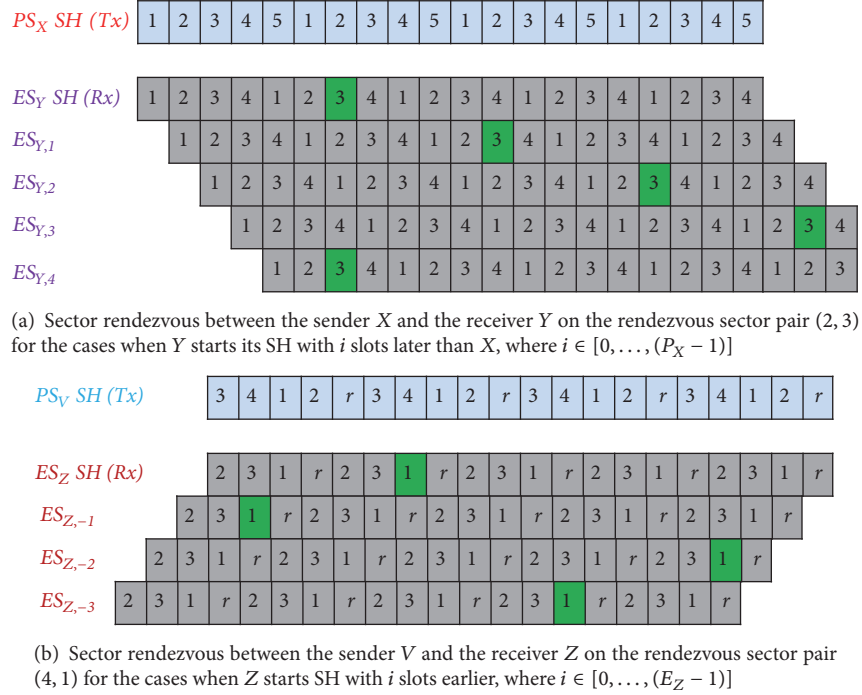


FIGURE 2: Successful synchronous and asynchronous sector rendezvous for the two pairs of communicating SUs in Figure 1.

bit sequence such as its globally unique ID. The SH sequence is constructed as an interleaved sequence of several PS and ES SH sequences through a two-step approach. Firstly, each SU transforms its unique ID according to a certain design into another ID sequence so that it is cyclically unique; that is, the resulting ID sequences of any two SUs are cyclically rotationally distinct to each other. Secondly, the SU replaces any bit of 1 (or 0) in its new ID sequence with a PS-based (or ES-based) SH sequence. Accordingly, for any pair of SUs, the cyclic uniqueness property will guarantee the existence of some time instances, where the two SUs are playing different roles. Hence, the sector rendezvous is achieved when one SU is hopping according to its PS sequence while the other SU is hopping based on its ES sequence and vice versa.

Several methods have been proposed in the literature to transform the unique ID into another cyclically unique binary sequence. In [32], a method was proposed to expand the  $m$ -bit ID into another  $3m$ -bit extended ID that is cyclically unique. The unique  $m$ -bit ID in that method is expanded by appending  $m$ -bit consecutive 0's into the beginning of the ID and other  $m$ -bit consecutive 1's at the end of the ID. Another method for generating cyclically unique IDs that are used for the construction of symmetric role SH sequences has been proposed in [30]. The method appends the original  $m$ -bit ID with other  $(m + 1)$ -bits of consecutive 0's and 1's, which results in  $(2m + 1)$ -bits expanded ID sequence. However, the extended ID sequences generated by these methods are relatively long, especially for the former method. This results in long rendezvous delay when they are used for constructing symmetric role sequences. Therefore, we propose an alternative method for constructing

cyclic rotationally distinct sequences, which provides shorter extended ID lengths than the methods in [30, 32]. So, it provides shorter sector rendezvous delay when it is used for constructing symmetric role sequences in our IPES-SH scheme.

*4.1.1. Constructing the Cyclic Unique ID Sequences.* In our method, each  $m$ -bit ID is extended by appending only  $m$ -bits of 1's and 0's in the beginning and in the end of the ID.

**Lemma 2.** *Given any two  $m$ -bit ID sequences  $\alpha = \{\alpha_1, \dots, \alpha_m\}$  and  $\beta = \{\beta_1, \dots, \beta_m\}$ , let  $\mathbf{a}$  and  $\mathbf{b}$  be two  $2m$ -bit expanded ID sequences generated from  $\alpha$  and  $\beta$  as follows:*

$$\mathbf{a} \stackrel{\text{def}}{=} \mathbf{1}(\lceil m/2 \rceil) \parallel \alpha \parallel \mathbf{0}(\lfloor m/2 \rfloor) \text{ and } \mathbf{b} \stackrel{\text{def}}{=} \mathbf{1}(\lceil m/2 \rceil) \parallel \beta \parallel \mathbf{0}(\lfloor m/2 \rfloor),$$

where  $\mathbf{1}(\cdot)$  is a bit sequence composed of only 1's and  $\mathbf{0}(\cdot)$  is a bit sequence composed of only 0's. Then  $\mathbf{a}$  and  $\mathbf{b}$  are cyclic rotationally distinct from each other, which means that

$$\text{If } \mathbf{a} \neq \mathbf{b} \implies \mathbf{a} \neq \text{rotate}(\mathbf{b}, k), \quad \forall k \in (0, 2m - 1]. \quad (1)$$

*Proof.* To prove the above lemma, we consider all the possible cases that may happen when sequence  $\mathbf{b}$  is rotated with  $(k \in (0, 2m - 1))$ . We show in each case that bits in sequence  $\mathbf{a}$  and other bits in sequence  $\mathbf{b}' = \text{rotate}(\mathbf{b}, k)$  have different values, even though these bits are in the same positions. Considering the five cases in Figure 3, it is sufficient to prove that  $\mathbf{a}$  and  $\mathbf{b}' = \text{rotate}(\mathbf{b}, k)$  are cyclic rotationally distinct to each other.  $\square$

*Case 1* ( $k \in (0, \lceil m/2 \rceil]$ ). As indicated by the red arrow in Figure 3, it holds that  $a_{2m} = 0$  and  $b'_{2m} = 1$ .

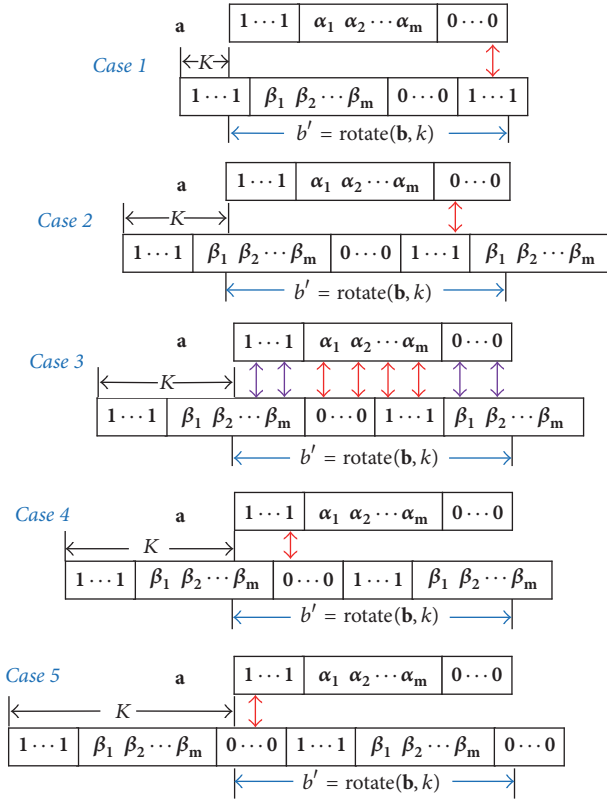


FIGURE 3: Illustration of the five cases in the proof of Lemma 2.

*Case 2* ( $k \in (\lceil m/2 \rceil, m)$ ). As indicated by the red arrow in Figure 3, it holds that  $a_{\lceil m/2 \rceil + m + 1} = 0$  and  $b'_{\lceil m/2 \rceil + m + 1} = 1$ .

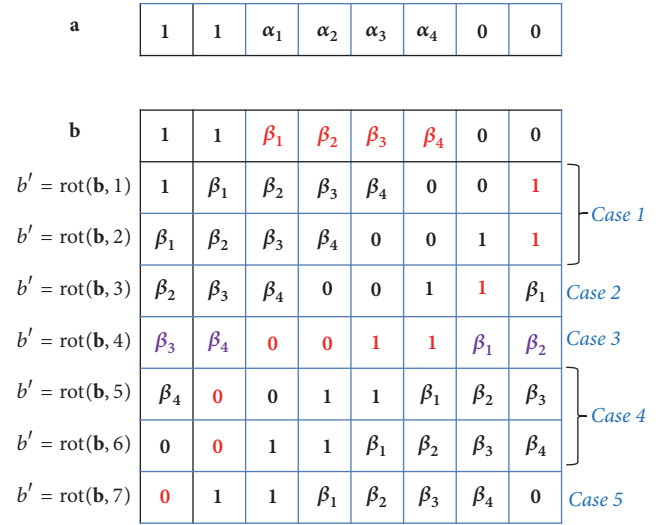
*Case 3* ( $k = m$ ). As indicated by the  $m$  red arrows in Figure 3, the  $m$  bits of sequence  $\mathbf{a}$  starting from  $a_{\lceil m/2 \rceil + 1}$  are  $\{\alpha_1, \dots, \alpha_{m-1}\}$ , while the  $m$  bits of  $b'$  in the same positions are  $\mathbf{0}_{\lfloor m/2 \rfloor} \parallel \mathbf{1}_{\lceil m/2 \rceil}$ . On the other hand, as indicated by the  $m$  purple arrows in Figure 3, the first  $\lceil m/2 \rceil$  bits of sequence  $\mathbf{a}$  are 1's and the last  $\lfloor m/2 \rfloor$  bits are 0's, whereas the first  $\lceil m/2 \rceil$  bits of  $b'$  are  $\{\beta_{\lceil m/2 \rceil}, \dots, \beta_m\}$  and the last  $\lfloor m/2 \rfloor$  bits are  $\{\beta_1, \dots, \beta_{\lfloor m/2 \rfloor}\}$ . And because  $\alpha \neq \beta$ , it holds that there must be at least a single bit that is different in  $\mathbf{a}$  and  $b'$ .

*Case 4* ( $k \in (m, m + \lfloor m/2 \rfloor)$ ). As indicated by the red arrow in Figure 3, it holds that  $a_{\lceil m/2 \rceil} = 1$  and  $b'_{\lceil m/2 \rceil} = 0$ .

*Case 5* ( $k \in (m + \lfloor m/2 \rfloor, 2m - 1)$ ). As indicated by the red arrow in Figure 3, it holds that  $a_1 = 1$  and  $b'_1 = 0$ .

According to these possible cases, we conclude that  $\mathbf{a} \neq \text{rotate}(\mathbf{b}, k)$ ,  $\forall k \in (0, 2m - 1)$ . In Figure 4, we give an example for two ID sequences of original lengths  $m = 4$  which are expanded to  $m = 8$  bits. The figure illustrates the cyclic uniqueness property between the IDs for all the rotation cases (i.e.,  $\forall k \in [0, 7]$ ).

**4.1.2. Generating the Interleaved Sector Hopping Sequence.** We now explain how to generate the symmetric IPES-SH sequence for any SU, say  $SU_i$ . Let the number of sectors for


 FIGURE 4: An illustrative example for the correctness of our cyclic rotationally distinct sequences construction method when  $m = 4$ .

$SU_i$  be  $N_i$  and hence the sector set  $S_i = \{1, \dots, N_i\}$ . Suppose that  $SU_i$  has  $m$ -bits globally unique ID sequence,  $\alpha$ , which is extended by our above method to  $2m$ -bits sequence  $\mathbf{a} = \mathbf{1}_{\lceil m/2 \rceil} \parallel \alpha \parallel \mathbf{0}_{\lfloor m/2 \rfloor}$ .

- (i) Select randomly a starting index  $k \in [1, N_i]$  and generate a rotated set  $S_i^P$  by rotating  $S_i$  circularly starting from  $k$  as  $S_i^P = \text{rotate}(S_i, k - 1)$ . Also, generate another sector indices set as a reverse of  $S_i^P$  which is  $S_i^E = \text{Reverse}(S_i^P)$ .
- (ii) Find ( $P_i : P_i > 3$ ) as the smallest prime number that is not smaller than  $N_i$ . Also find ( $E_i : E_i \notin \text{AES}$ ) as the smallest even number that is not smaller than  $N_i$ .
- (iii) Define an empty matrix  $M_i$  that has  $2m$  columns and  $P_i \times E_i$  rows.
- (iv) Fill the matrix by mapping each bit in  $\mathbf{a}$  to a certain column as described in Algorithm 3.
- (v) Generate the SH sequence by concatenating the matrix rows (row by row).  $SU_i$  keeps hopping according to this generated SH sequence and repeats it in order to rendezvous with its pair partner SU.

Figure 5 illustrates the IPES-SH sequence construction matrices for  $SU_V$  and  $SU_Z$  in our previous example in Section 3.1 (Figure 1(b)). In Figure 5, the ID sequence of  $SU_V$  that has  $N_v = 4$  sectors is  $\alpha = \{1, 0\}$  which is expanded to  $\mathbf{a} = \{1, 1, 0, 0\}$ . On the other side, the ID sequence of  $SU_Z$  that has  $N_z = 3$  sectors is  $\beta = \{0, 1\}$  which is expanded also to  $\mathbf{b} = \{1, 0, 1, 0\}$ . The constructed matrix for  $SU_V$  has  $P_v \times E_v = 5 \times 4 = 20$  rows and  $2m = 4$  columns. Similarly,  $SU_Z$  constructs its matrix with  $P_z \times E_z = 5 \times 4 = 20$  rows and  $2m = 4$  columns. Each SU will assign its matrix columns with either PS sequence or ES sequence based on the corresponding bits of its extended ID sequence. For example, since the first bit of  $SU_V$  extended ID is one,  $SU_V$  firstly

- (1) **for**  $c = 1 : 2m$  **do**
- (2)   **if** ( $a_c == 1$ ) **then**
- (3)     Invoke Algorithm 1 with  $S_i^P$  and  $N_i$  to construct a round  $\omega$  of an PS sequence.
- (4)     generate  $\omega'$  by repeating  $\omega$  for  $E_i$  times.
- (5)     Map the  $c_{th}$  column of the matrix with  $\omega'$ .
- (6)      $S_i^P = \text{Rotate}(S_i^P, 1)$ .
- (7)   **else**
- (8)     Invoke Algorithm 2 with  $S_i^E$  and  $N_i$  to construct a round  $\gamma$  of an ES sequence.
- (9)     generate  $\gamma'$  by repeating  $\gamma$  for  $P_i$  times.
- (10)     Map the  $c_{th}$  column of the matrix with  $\gamma'$ .
- (11)      $S_i^E = \text{Rotate}(S_i^E, 1)$ .
- (12)   **end if**
- (13) **end for**

ALGORITHM 3

generates its first sector sets as  $S_v^P = \{3, 4, 1, 2\}$  and then invokes Algorithm 1 with  $S_v^P$  and  $N_v = 4$  to construct a round of a PS sequence  $\omega = [3\ 4\ 1\ 2\ r]$ . This round  $\omega$  is repeated for  $E_v = 4$  times and assigned to the first column of  $SU_V$  matrix. Similarly, since the second bit of  $SU_V$  extended ID is one, the second column of  $SU_V$  matrix is assigned with a repeated sequence of the PS sequence  $[4\ 1\ 2\ 3\ r]$ , which is constructed after rotating the sector set  $S_v^P$  by one. On the other hand,  $SU_V$  assigns the third and fourth columns of its matrix with ES sequences because the corresponding 3<sub>rd</sub> and 4<sub>th</sub> bits of its extended ID sequence are zeros. Specifically,  $SU_V$  invokes Algorithm 2 with  $S_v^E = \text{Reverse}(S_v^P)$  and  $N_v = 4$  to construct a round of an ES sequence  $\gamma = [2\ 1\ 4\ 3]$ . This round  $\gamma$  of the ES sequence is then repeated for  $P_v = 5$  times and assigned to the third column of  $SU_V$  matrix. Similarly, the fourth column of  $SU_V$  matrix is filled with the ES sequence  $[1\ 4\ 3\ 2]$  after repeating it for  $P_v = 5$  times. Note that  $SU_Z$  will follow the same procedures as  $SU_V$  to construct its matrix with taking into account the different expanded ID sequence  $b_z = \{1, 0, 1, 0\}$  and  $N_z$ , as well as the initial sector sets  $S_z^P$  and  $S_z^E$ .

Figure 6 shows partial sector slots of the IPES-SH sequences for the two SUs ( $SU_V$  and  $SU_Z$ ). As depicted from the figure, the IPES-SH sequence of each SU is generated by concatenating the rows of the SU constructed matrix in Figure 5 row by row. The sequences are generated as interleaved slots of PS (light blue) and ES (gray) slots according to the respective columns types in the matrices. The figure also illustrates the rendezvous sector occurrence between the SUs (indicated by the green circle) on the sector rendezvous pair (4, 1).

**4.2. Scheme Analysis.** In this subsection, the theoretical performance of IPES-SH scheme is studied where the MSRL is derived.

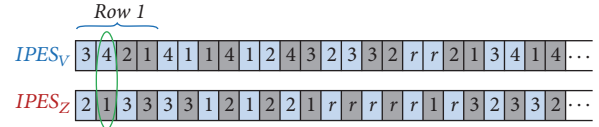
**Theorem 3.** *Under the IPES-SH scheme, the MSRL between a pair of SUs ( $SU_i$  and  $SU_j$ ) is  $2m \times (\max\{(P_i E_j), (E_i P_j)\})$ .*

1	1	0	0
3	4	2	1
4	1	1	4
1	2	4	3
2	3	3	2
r	r	2	1
3	4	1	4
4	1	4	3
1	2	3	2
2	3	2	1
r	r	1	4
3	4	4	3
4	1	3	2
1	2	2	1
2	3	1	4
r	r	4	3
3	4	3	2
4	1	2	1
1	2	1	4
2	3	4	3
r	r	3	2

1	0	1	0
2	1	3	3
3	3	1	2
1	2	2	1
r	r	r	r
r	1	r	3
2	3	3	2
3	2	1	1
1	r	2	r
r	1	r	3
r	3	r	2
2	2	3	1
3	r	1	r
1	1	2	3
r	3	r	2
r	2	r	1
2	r	3	r
3	1	1	3
1	3	2	2
r	2	r	1
r	r	r	r

(a) IPES matrix  $M_V$  for  $SU_V$  (b) IPES matrix  $M_Z$  for  $SU_Z$ 

FIGURE 5: The construction of the IPES matrices  $M_V$  and  $M_Z$  for  $SU_V$  and  $SU_Z$ , respectively.  $N_V = 4$  and  $N_Z = 3$ ;  $\alpha_V = \{1, 0\}$  and  $\beta_Z = \{0, 1\}$ . So the expanded ID sequences are  $\mathbf{a}_V = \{1, 1, 0, 0\}$  and  $\mathbf{b}_Z = \{1, 0, 1, 0\}$ .

FIGURE 6: IPES-SH sector rendezvous between  $SU_V$  and  $SU_Z$  for the synchronous case.

*Proof.* To prove that IPES-SH has  $MSRL = 2m(\max\{(P_i E_j), (E_i P_j)\})$ , it is sufficient to prove that any arbitrary pair of IPES-SH sequences, for example,  $IPES_i$  and  $IPES_j$ , can achieve a successful sector rendezvous within  $2m(\max\{(P_i E_j), (E_i P_j)\})$  sector slots.

Let  $IPES_i$  and  $IPES_j$  be the corresponding IPES-SH sequences of IPES matrices  $M_i$  and  $M_j$  (i.e.,  $IPES_i$  and  $IPES_j$  are generated by concatenating the rows of matrices  $M_i$  and  $M_j$ , resp.). For example, Figures 5(a) and 5(b) show the IPES matrices  $M_V$  and  $M_Z$ , respectively. Without loss of generality, assume that  $SU_j$  starts its SH sequence  $\delta$  sector slots earlier than the start of  $SU_i$ . In each SH period of  $SU_i$ , the SH sequence of  $SU_j$  is  $\text{rotate}(IPES_j, \delta)$ . Clearly, the rendezvous between this pair of SUs is the same as the rendezvous of  $M_i$  and  $M_{(j, \delta)}$ . Suppose that the sector rendezvous pair is  $(h_i, h_j) \in \{1, 2, \dots, N_i\} \times \{1, 2, \dots, N_j\}$ . The rendezvous of the matrices is a pair of entries in the matrices whose value in  $M_i$  is  $h_i$  and its values in  $M_{(j, \delta)}$  is  $h_j$ . Without loss of generality, suppose that the sector slot shift  $\delta = 2m \times \delta_R + \delta_C$ , where  $\delta_R \in [0, (P_j \times E_j) - 1]$ , is the shift of row and  $\delta_C \in [0, (2m) - 1]$  is the shift of column. Below, we consider the two different cases for rendezvous of  $IPES_i$  and  $IPES_j$ .  $\square$

1	0	1	0
---	---	---	---

2	2	3	1
3	r	1	r
1	1	2	3
r	3	r	2
r	2	r	1
2	r	3	r
3	1	1	3
1	3	2	2
r	2	r	1
r	r	r	r
2	1	3	3
3	3	1	2
1	2	2	1
r	r	r	r
r	1	r	3
2	3	3	2
3	2	1	1
1	r	2	r
r	1	r	3
r	3	r	2

0	1	0	1
---	---	---	---

2	3	1	3
r	1	r	1
1	2	3	r
3	r	2	r
2	r	1	2
r	3	r	3
1	1	3	1
3	2	2	r
2	r	1	r
r	r	r	2
1	r	3	2
3	3	2	3
2	1	1	1
r	2	r	r
1	r	3	r
3	r	2	2

(a)  $M_{(Z,40)}$ ,  $\delta_C = 0$ , and  $\delta_R = 10$  (b)  $M_{(Z,41)}$ ,  $\delta_C = 1$ , and  $\delta_R = 10$

FIGURE 7: The IPES matrix  $M_Z$  for  $SU_Z$  when it is circularly rotated with (a)  $\delta = 2m \times 10 + 0 = 40$  sector slots and (b)  $\delta = 2m \times 2 + 1 = 41$  slots.

*Case 1* ( $\delta_C = 0$ ). In this case, it is implied that there is no column shift. Recall that the expanded ID sequences of  $SU_i$  and  $SU_j$  are distinct. Since the columns types of the matrices are assigned based on these distinct expanded IDs, it is guaranteed that there must exist at least a single common column  $f$  in both matrices which is a PS-column in one matrix and an ES-column in the other matrix, and vice versa. In other words, the  $f_{th}$  column of  $M_i$  contains a PS-SH sequence (reps., ES-SH), while the same position  $f_{th}$  column in  $M_{(j,\delta)}$  contains an ES-SH (resp., PS-SH). By Theorem 1, we know that when  $SU_i$  and  $SU_j$  repeat the PS-SH (resp., ES-SH) and the ES-SH (resp., PS-SH) sequences, respectively, they rendezvous within  $P_i \times E_j$  (resp.,  $E_i \times P_j$ ). Meanwhile, since the elements of a specific column of each matrix appear in the corresponding IPES-SH sequence every  $2m$  slots, for any value of the row shift  $\delta_R$ ,  $M_i$  and  $M_{(j,\delta)}$  are guaranteed to rendezvous on their  $f_{th}$  columns no later than  $2m \times \max\{(P_i E_j), (E_i P_j)\}$ . Specifically, the rendezvous happens when an entry of the  $f_{th}$  column in  $M_i$  is  $h_i$ , while the same position entry of the  $f_{th}$  column in  $M_{(j,\delta)}$  is  $h_j$ . For example, Figure 5 shows the rendezvous of  $M_V$  and  $M_Z$  for the synchronous case where the slots shift  $\delta = 2m \times 0 + 0 = 0$ . The sector rendezvous occurs between the second columns of  $M_V$  and  $M_Z$  which is indicated by the green entry in  $M_Z$ . However, Figure 7(a) shows the IPES matrix of  $SU_Z$  when it is shifted with row shift  $\delta_R = 10$ . Hence, this means that  $\delta = 2m \times 10 + 0 = 40$ . The rendezvous between  $M_V$  in Figure 5 and  $M_{(Z,40)}$  in Figure 7(a) is achieved at their third columns.

*Case 2* ( $\delta_C \neq 0$ ). In this case, it holds that there is a column shift  $\delta_C \in [1, (2m - 1)]$ . Let  $\mathbf{a}$  and  $\mathbf{b}$  be the expanded ID sequences of  $SU_i$  and  $SU_j$ , respectively. By Lemma 2, we know

that  $\mathbf{a}$  and  $\mathbf{b}' = \text{rotate}(\mathbf{b}, k)$ , where  $k \in (2m - 1)$  are *cyclic rotationally distinct* to each other. Thus, for a column shift  $\delta_C \in [1, (2m - 1)]$  of matrix  $M_j$ , there must exist a column  $f$  in matrix  $M_i$  which has different type than the same position  $f_{th}$  column in the shifted matrix  $M_{(j,\delta_C)}$ . Accordingly, the rendezvous is guaranteed to occur at the  $f_{th}$  columns in the matrices, despite any value of the row shift  $\delta_R$ . For example, Figure 7(b) shows the shifted IPES matrix of  $SU_Z$  when the column shift  $\delta_C = 1$  and the row shift  $\delta_R = 10$ , which results in  $\delta = 2m \times 10 + 1 = 41$  slots. The first rendezvous between  $M_V$  in Figure 5 and  $M_{(Z,41)}$  in Figure 7(b) is achieved at the fourth columns.

Summarizing the discussion above, we show that, in IPES-SH, any two SUs are guaranteed to rendezvous on their sector rendezvous pair within SH period  $2m \times \max\{(P_i E_j), (E_i P_j)\}$ .

## 5. Combined Sector and Channel Hopping Schemes

While we explained in the previous sections the procedures of our SH schemes by which the SUs keep steering their antennas in order to achieve sector rendezvous with their communicating partners, the scheme for channel hopping (CH) exposed by the SUs in their sectors for achieving a channel rendezvous between them was not explained. In this section, the design of the exposed CH scheme and the procedure for the combined sector and channel hopping (SCH) schemes are presented. The key for the design of the exposed CH scheme is to construct two different types of CH sequences which will be combined within the two different types of PES-SH sequences. These CH sequences must guarantee a successful channel rendezvous between the pair of SUs as long as they achieve a successful sector rendezvous (i.e., directing their antenna beams towards each other). Furthermore, the CH sequences should be designed in such a way that the pair of communicating SUs stay for a similar period (i.e., number of time slots) in each sector of their SH sequences. By doing this, the pair of communicating SUs are guaranteed to achieve successful sector and channel rendezvous within a bounded and short time, despite any asynchronous time offsets between their local clocks.

*5.1. Asymmetric Grid Quorum-Based Channel Hopping.* In this subsection, we explain the design of our Asymmetric Grid Quorum-based Channel Hopping (AGQ-CH) scheme that is executed by the SUs in each sector of their SH sequences. The AGQ-CH scheme utilizes the grid quorum system (GQS) in asymmetric-role design, where two types of CH sequences are constructed. These types of CH sequences will be combined within the two different types of our SH sequences. Some preliminary definitions related to grid quorum systems are presented first to facilitate the understanding of the CH scheme.

*Definition 4.* For a set  $\mathbb{Z}_n = \{1, 2, \dots, n\}$ , a quorum system  $\mathcal{Q}$  under  $\mathbb{Z}_n$  is a group of nonempty subsets of  $\mathbb{Z}_n$ , each called a quorum, such that  $\forall X$  and  $Y \in \mathcal{Q}$ ,  $X \cap Y \neq \emptyset$ . Here,  $\mathbb{Z}_n$  is the set of integers less than or equal to  $n$ .

*Definition 5.* A GQS arranges the elements of  $\mathbb{Z}_n$  as a  $\sqrt{n} \times \sqrt{n}$  square grid array, where  $n$  must be a square of a positive integer. Hence, a quorum is formed as a union of the elements of one column and one row of the grid. There are  $n$  grid quorums in a GQS that is constructed under  $\mathbb{Z}_n$  and each quorum has a size of  $(2 \times \sqrt{n} - 1)$ .

For example, a GQS  $Q$  under  $\mathbb{Z}_n = \{1, 2, 3, 4\}$  is  $Q = \{Q_1, \dots, Q_4\} = \{\{1, 2, 3\}, \{1, 2, 4\}, \{1, 3, 4\}, \{2, 3, 4\}\}$ .

*Definition 6.* For a given integer  $i$  and a grid quorum  $\mathcal{G}$  in a GQS  $Q$  under  $\mathbb{Z}_n$ , we define  $\text{rotate}(\mathcal{G}, i) = \{(x+i) \bmod n, x \in \mathcal{G}\}$  to denote a cyclic rotation of quorum  $\mathcal{G}$  by  $i$ .

*Definition 7.* A GQS  $Q$  under  $\mathbb{Z}_n$  satisfies the rotation closure property because,  $\forall \mathcal{G}_{i_1}, \mathcal{G}_{i_2} \in Q$  and  $\forall j_1, j_2 \in \mathbb{Z}_n$ ,  $\text{rotate}(\mathcal{G}_{i_1}, j_1) \cap \text{rotate}(\mathcal{G}_{i_2}, j_2) \neq \emptyset$ .

GQSs have been utilized to construct CH sequences that achieve asynchronous communications because they satisfy the intersection and the rotation closure properties [33, 34]. In the conventional GQS, each grid quorum is formed as a union of the elements of one column and one row of the grid array. However, different from the conventional GQS, our asymmetric GQS (AGQS) uses semigrig quorums. One semiquorum, called the Grid Column-based Quorum (GCQ), is formed from the elements of a single column of the grid. Meanwhile, the other semiquorum, called Grid Row-based Quorum (GRQ), is formed from the elements of a single row in the grid. The nonempty intersection and rotation closure properties in the AGQS are inherited from the conventional GQS. Specifically, for any arbitrary pair of GCQ and GRQ, there must exist one common element between them despite any rotation of the grid.

The GCQs and GRQs in the AGQS are used to construct two asymmetric CH sequences that can be combined within the different types of sectors in our SH schemes. The constructed CH sequences are guaranteed to achieve a successful channel rendezvous between a pair of communicating SUs as long as there exists at least a single common channel between the available channel sets of the SUs. In our AGQ-CH scheme, to construct CH sequences for assigning  $n$  channels,  $n \times n$  grid array is built. In the GCQ-based CH sequence, the  $n$  rows of the grid are used for assigning the  $n$  channels into the CH sequence, where the elements of each row are used to map a single channel. On the other side, the  $n$  columns of the grid are used for the assignment of the  $n$  channels into the GRQ-based CH sequence. For example, Let  $n = 4$  be the number of channels for a sender  $SU_x$  and a receiver  $SU_y$ . Suppose that  $SU_x$  has the channel set  $\mathcal{C}_x = \{Ch_1, Ch_2, Ch_3, Ch_4\}$ , while the channel set of  $SU_y$  is  $\mathcal{C}_y = \{Ch_3, Ch_5, Ch_6, Ch_8\}$ . Accordingly, a grid array of size  $4 \times 4$  is formed by both SUs as shown in Figure 8. Without loss of generality, assume that the sender uses the 4 GCQs to map its channels into the time slots of its CH sequence as depicted in Figure 8(a), while the receiver  $SU_y$  maps its channels based on the 4 GRQs as depicted in Figure 8(b). The CH sequences for both SUs are shown in Figure 8(c), where they map each channel of their channel sets into the time slots of their CH sequence

according to the selected (GCQ or GRQ) semiquorum. As shown in Figure 8(c), the channel rendezvous is achieved on the common channel  $Ch_3$  between the SUs despite the time offsets between their local clocks.

*5.2. Channel Ranking.* As explained in the beginning of the section, the sector frame length which represents the number of time slots by which every SU spends on each sector for executing CH should be the same in all SUs. This is in order to guarantee channel rendezvous between any pair of neighbouring SUs side by side with the sector rendezvous despite any time offsets between their local clocks. To achieve this, we let the SUs construct their combined CH sequences based on the best-quality ( $n \subseteq L$ ) channels. The channel's quality is generally represented by the quantity of the measured PU noise on the channel within the corresponding sector. However, for cases where some of the channels have the same measured PU noise, channels indices are used to differentiate between their ranking levels. Specifically, the bigger the channel index, the higher the quality. We highlight here that the similarity of the measured PU noises for some channels is a practical issue in DIR-CRNs which happen when the channels are idle from any PU activity within the sector area.

The channel ranking is done by each SU before executing the rendezvous process based only on its own view of the available channels in its sectors. Each  $SU_i$  ranks the  $L$  network channels in each sector  $S_k$  of its sectors set  $S_i = \{S_1, S_2, \dots, S_{N_i}\}$  based on their qualities within the sector  $k$ . Thus, a ranking table of size  $L \times N_i$  is maintained by each  $SU_i$  which contains the ranked channels in all the sectors. This table is called Sectors Ranked Channels Table (SRCT), where each column  $k$  of it indicates a sector of the  $N_i$  sectors. These columns contain the  $L$  network channels ranked decreasingly from the best to the worst according to their qualities within the corresponding sectors. We note here that since each SU in the DIR-CRN performs the same ranking mechanism, this will increase the probability of having a similar ranked channel list among any pair of neighbouring SUs on their rendezvous sectors.

*5.3. Combined SCH Sequence Generation.* We now explain the generation procedures for the combined PES-SCH and IPES-SCH sequences.

*5.3.1. Combined PES-SCH Scheme.* Since our PES-SH scheme is designed based on two different types of coprimality-based sequences (i.e., either PS or ES), we combine each sector of the SH sequences according to its type with a corresponding type from the two AGQ-CH sequences. Specifically, each sector of the sender PS-SH sequence is combined with a GCQ-CH sequence, while each sector of the receiver ES-SH sequence is combined with a GRQ-CH sequence. Algorithms 4 and 5 describe the SCH generation procedures for the sender and receiver SUs, respectively. As illustrated by the algorithms, each SU will keep hopping on its best  $n$  quality channels in each sector of its SH sequence according to the corresponding CH sequence. This will guarantee that when a successful sector rendezvous occurs between a sector

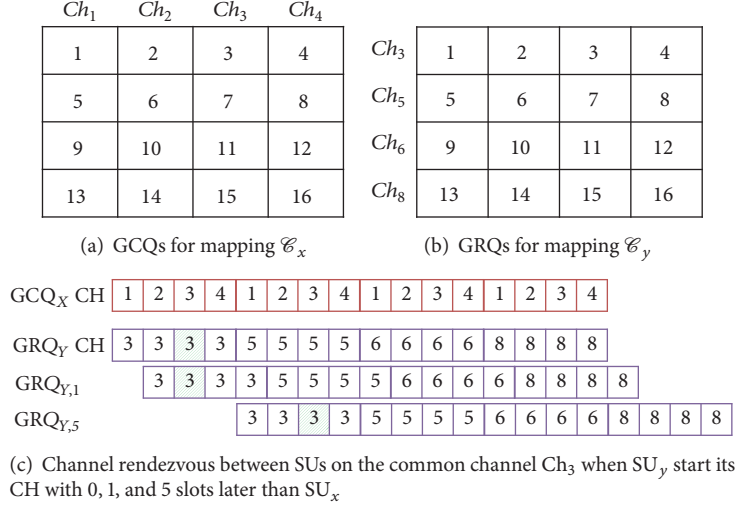


FIGURE 8: An example of AGQ-CH sequences constructions and rendezvous for a pair of communicating SUs.

**Input:**  $N_s, S_s, SRCT_s, n$ .

- (1) Invoke Algorithm 1 with  $N_s$  and  $S_s$  to construct a round  $\omega_s$  of an PS-SH sequence.
- (2)  $t_{\text{Frame}} = 0$
- (3) **while** (*not rendezvous*) **do**
- (4)  $Current\_sector = \omega_s((t_{\text{Frame}} \bmod P_s) + 1)$ .
- (5) Steer the antenna to ( $Current\_sector$ ).
- (6) Select the best channel list (BCL) in ( $Current\_sector$ ) as  $BCL = SRCT_s[1:n][Current\_sector]$ .
- (7) Construct a GCQ-CH sequence based on BCL.
- (8) **for** ( $t = 1 : n^2$ ) **do**
- (9) Attempt rendezvous on channel  $GCQ_s(t)$ .
- (10) **end for**
- (11)  $t_{\text{Frame}} = t_{\text{Frame}} + 1$ .
- (12) **end while**

ALGORITHM 4: The sender SCH generation algorithm (PS-SCH).

**Input:**  $N_r, S_r, SRCT_r, n$ .

- (1) Invoke Algorithm 2 with  $N_r$  and  $S_r$  to construct a round  $\gamma_r$  of an ES-SH sequence.
- (2)  $t_{\text{Frame}} = 0$
- (3) **while** (*not rendezvous*) **do**
- (4)  $Current\_sector = \gamma_r((t_{\text{Frame}} \bmod E_r) + 1)$ .
- (5) Steer the antenna to ( $Current\_sector$ ).
- (6)  $BCL = SRCT_s[1:n][Current\_sector]$ .
- (7) Construct a GRQ-CH sequence based on BCL.
- (8) **for** ( $t = 1 : n^2$ ) **do**
- (9) Attempt rendezvous on channel  $GRQ_r(t)$ .
- (10) **end for**
- (11)  $t_{\text{Frame}} = t_{\text{Frame}} + 1$ .
- (12) **end while**

ALGORITHM 5: The receiver SCH generation algorithm (ES-SCH).

frame of the sender  $SU_s$  and a sector frame of its receiver  $SU_r$ , a successful channel rendezvous is achieved between  $GCQ-CH_s$  and the  $GRQ-CH_r$ . The channel rendezvous is guaranteed as long as there is a common channel between their  $n$  best channels, where they can set up a link through the exchange of RTS/CTS messages.

For example, consider the pair of sender  $SU_X$  and receiver  $SU_Y$  in our previous example in Figure 1(a). The SCH sequences constructions for the pair of SUs and the rendezvous among them when they construct their combined CH sequences based on  $n = 2$  best-quality channels are illustrated in Figure 9. As a sender,  $SU_X$  in Figure 9(a) combines each sector of its PS-SH sequence with a grid column (GCQ-CH) sequence based on the two best-ranked channels of the respected column for the sector in  $SRCT_X$ . For instance, the sector  $S_1$  is combined with a GCQ-CH sequence generated based on the two best channels {2, 4} of the 1st column of  $SRCT_X$ ; the GCQ-CH is [2 4 2 4]. On the other hand, each ES sector of the ES-SH sequence for the receiver  $SU_Y$  in Figure 9(b) is combined with a grid row (GRQ-CH) sequence based on the best two channels of the  $SRCT_Y$  column which corresponds to the sector number. For instance,  $SU_Y$  combine the GRQ-CH sequence [6 6 8 8] within its sector  $S_1$  which is constructed based on the best channels {6, 8}. The sector and channel rendezvous between the SUs when they start their PES-SCH sequences synchronously is shown in Figure 9(c). The rendezvous is achieved during the 25th and 28th time slots on the sector rendezvous pair ( $S_2$  of  $SU_X$ ,  $S_3$  of  $SU_Y$ ), as well as on the rendezvous channels {1, 6}. However, when  $SU_X$  starts its SCH 4 time slots later than  $SU_Y$ , the channel and sector rendezvous is achieved after 5 time slots only from the SCH start time of  $SU_X$ .

**5.3.2. Combined IPES-SCH Scheme.** For this symmetric role scheme, any SU can generate its SCH sequence according

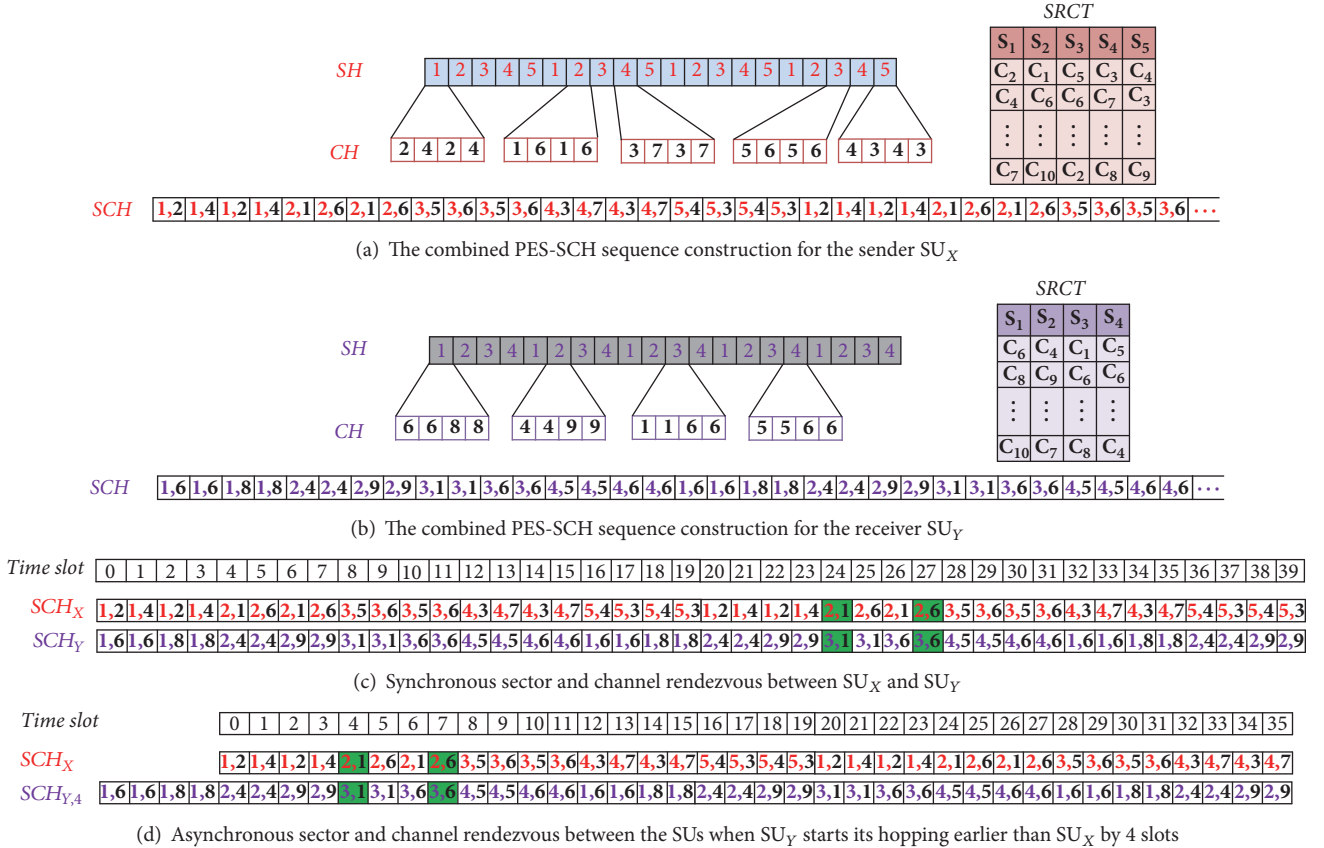


FIGURE 9: Rendezvous between SUs X and Y according to the combined PES-SCH scheme.  $N_X = 5$  and  $N_Y = 4$ . Number of best-quality channels per each sector  $n = 2$ .

to Algorithm 6. During each sector frame of its interleaved SH sequence that is constructed using the method in Section 4.1.2, the SU executes one type of the AGQ-CH sequences according to the type of the frame. Specifically, if the sector frame is a prime-based (P-frame), the SU generates a GCQ-CH based on the  $n$  best-quality channels in the sector. On the other hand, when the sector is an even-based (E-frame), the SU generates a GRQ-CH. This will ensure that whenever the sector rendezvous occurs between a P-frame of IPES<sub>i</sub> and an E-frame of IPES<sub>j</sub>, channel rendezvous is achieved between the GCQ<sub>i</sub> CH sequence and the GRQ<sub>j</sub> CH sequence, and vice versa.

**5.4. Performance Analysis of the Combined SCH Schemes.** In this subsection, we analyze the theoretical performance for the combined SCH schemes. Specifically, we prove the guaranteed rendezvous between any two SUs performing the combined SCH scheme by deriving the maximum time-to-rendezvous (MTTR).

**Theorem 8.** For any scheme  $\mathbb{S}$  of our SH schemes which is combined with the AGQ-CH scheme for  $n$  best-quality channels, the MTTR of the combined SCH is  $(\text{MSRL}(\mathbb{S}) \times n^2)$ . MSRL( $\mathbb{S}$ ) here denotes the maximum sector rendezvous latency for the  $\mathbb{S}$  SH scheme.

**Input:**  $N_i, S_i$ , Extended-ID  $\mathbf{a}$ , SRCT <sub>$i$</sub> ,  $n$ .

- (1) Construct an IPES-SH sequence  $U_i$  as explained in Section 4.1.2.
- (2) period =  $(P_i \times E_i \times \text{length}(\mathbf{a}))$ .
- (3)  $t_{\text{Frame}} = 0$
- (4) **while** (not rendezvous) **do**
- (5)   Current-sector =  $U_i((t_{\text{Frame}} \bmod \text{period}) + 1)$ .
- (6)   Steer the antenna to (Current-sector).
- (7)   BCL = SRCT <sub>$i$</sub> [1 :  $n$ ][Current-sector].
- (8)   **if** (Current-sector is a P-sector) **then**
- (9)     Construct a GCQ-CH sequence based on BCL.
- (10)    **for** ( $t = 1 : n^2$ ) **do**
- (11)     Attempt rendezvous on channel GCQ <sub>$i$</sub> ( $t$ ).
- (12)    **end for**
- (13)    **else**
- (14)     Construct a GRQ-CH sequence based on BCL.
- (15)    **for** ( $t = 1 : n^2$ ) **do**
- (16)     Attempt rendezvous on channel GRQ <sub>$i$</sub> ( $t$ ).
- (17)    **end for**
- (18)    **end if**
- (19)     $t_{\text{Frame}} = t_{\text{Frame}} + 1$ .
- (20) **end while**

ALGORITHM 6: IPES-SCH generation algorithm.

*Proof.* To prove that the combined PES-SCH has MTTR =  $(P_i E_j) \times n^2$ , it suffices to prove that the pair of combined PES-SCH sequences, for example,  $SCH_i$  and  $SCH_j$ , can achieve successful sector and channel rendezvous within  $(P_i E_j) \times n^2$  time slots.

Without loss of generality, assume that  $SU_j$  starts its SCH sequence  $\delta$  time slots earlier than the start of  $SU_i$ . In each SCH period of  $SU_i$ , the SCH sequence of  $SU_j$  is  $\text{rotate}(SCH_j, \delta)$ . As we stated before, the SCH sequence can be viewed as a series of sector frames which are composed of  $n^2$  channel time slots. Let the clock drift  $\delta = n^2 \times \delta_F + \delta_S$ , where  $\delta_F \in [0, E_j - 1]$  denotes the shift amount of the sector frames and  $\delta_S \in [0, (n^2) - 1]$  denotes the shift of the channel time slots. Next, we prove the theorem in the following two cases.

*Case 1* ( $\delta_S = 0$ ). This case implies that the sector frames are perfectly aligned. In this case, since the SUs stay for similar number of time slots in each sector which is  $(n^2)$  for executing their corresponding AGQ-CH sequences, for any value of  $\delta_F$ , there must exist an entire overlap between a PS-frame of  $SCH_i$  and an ES-frame of  $SCH_j$  where the sector rendezvous happened. By Theorem 1, we know that the sector rendezvous is guaranteed to occur between a PS sector frame  $h_i$  and an ES sector frame  $h_j$  within  $(P_i E_j)$  sector frames. As a consequence, the channel rendezvous is guaranteed to happen between the GCQ<sub>i</sub> CH sequence of  $h_i$  and the GRQ<sub>j</sub> CH sequence of  $h_j$ . Thus, the MTTR is  $(P_i E_j)$  multiplied by the sector frame length  $n^2$ . Figures 9(c) and 9(d) show the sector and channel rendezvous between  $SU_X$  and  $SU_Y$  when  $\delta_S = 0$  for two different values of  $\delta_F$  and for  $n = 2$ . In Figure 9(c), when  $\delta_F = 0$  and hence the clock drift  $\delta = (n^2 \times 0 + 0) = 0$ ,  $SU_X$  can achieve the sector rendezvous with  $SU_Y$  on the second round of its SH frames. The SUs rendezvous on their commonly available channels (i.e., CH<sub>1</sub> and CH<sub>6</sub>). However, when  $\delta_F = 1$  and  $\delta = (n^2 \times 1 + 0) = 4$ ,  $SU_X$  can rendezvous with  $SU_Y$  earlier where it rendezvous with  $SU_Y$  during the first round of its SH frames.  $\square$

*Case 2* ( $\delta_S \neq 0$ ). When there is a time slot shift  $\delta_S \in [1, n^2]$ , it implies that the sector frames are not aligned. For any value of  $\delta_F$ , it is easily verified that each PS sector frame of  $SCH_i$  is overlapped with partial channel time slots from two consecutive ES frames of  $SCH_j$ . Specifically, the PS frame of  $SCH_i$  overlaps with  $n^2 - \delta_S$  time slots from the former ES frame and  $\delta_S$  time slots from the later ES frame of  $SCH_j$ . Recall the proof of Theorem 1, when  $SU_i$  repeats each round of its sector frames for  $E_i$  times, each occurrence of the  $h_i$  sector frame must overlap with different sector frame from the  $E_i$  sector frames of  $SU_j$ . The sector rendezvous is achieved when  $h_i$  overlaps with  $h_j$ . However, considering the time slot shift  $\delta_S$  of the  $SCH_j$  sequence, we can prove in the same way as case 1 that, within the same rendezvous delay bound  $((P_i E_j) \times n^2$  time slots), there must exist at least two occurrences of  $h_i$  which overlaps with different partial time slots of  $h_j$ . In one of these occurrences, the overlap happens between the first  $n^2 - \delta_S$  time slots of  $h_i$  and the last  $n^2 - \delta_S$  time slots of  $h_j$ . On the other occurrence, the overlap happens between

the last  $\delta_S$  time slots of  $h_i$  and the first  $\delta_S$  time slots of  $h_j$ . Accordingly, channel rendezvous can be achieved in any of these two partial sector rendezvous chances where partial slots of the GCQ<sub>i</sub> CH sequence in  $h_i$  overlap with other partial slots from the GRQ<sub>j</sub> CH sequence in  $h_j$ . For example, Figure 10 illustrates the asynchronous rendezvous between  $SU_X$  and  $SU_Y$  when  $\delta_F = 0$  for three different values of  $\delta_S$ .

Summarizing the discussion above, we show that, under the combined PES-SCH, any two SUs are guaranteed to achieve channel rendezvous within  $((P_i E_j) \times n^2)$  SCH period. We highlight here that the theoretical MTTR for the combined IPES-SCH is  $(2m \times \max\{(P_i E_j), (E_i P_j)\}) \times n^2$ . It can be proven in a similar way to the proof of the PES-SCH MTTR by considering the two alignment cases of the sector frames.

## 6. Results and Discussions

In this section, we evaluate the performance of our developed directional antenna rendezvous schemes and compare them with three related works in [19, 28, 30]. The former two selected schemes for comparisons are the only schemes in the literature which tackle the rendezvous issue in DIR-CRNs. However, since both of them are asymmetric-role, we select the third scheme [30] which is proposed for rendezvous in the 60 GHz networks for the comparison with our symmetric-role IPES scheme. This scheme follows a similar ID-based approach to our IPES-SH scheme. However, the extended ID in this scheme is relatively longer and the adjusted parameters of the number of sectors which are used for constructing the interleaved SH sequences are different.

*6.1. Performance Comparison of the SH Schemes.* We first compare the performance of our SH schemes with the two blind SH schemes in [28, 30]. The SH scheme in [19] is not compared here because it is not a blind scheme. Extensive simulation experiments are conducted to compute the sector rendezvous latency (SRL) between two neighboring SUs (a sender  $SU_i$  and a receiver  $SU_j$ ). In the simulations, we consider different antenna configurations for the SUs where we simulate several combinations for the number of sectors ( $N_i$  and  $N_j$ ). The relative locations of  $SU_i$  and  $SU_j$  represented by  $(h_i, h_j)$  as well as the clock drift are randomly generated. For the ID-based schemes, two different 7-bit IDs are randomly assigned to the SUs. For each  $(N_i$  and  $N_j)$  combination, the simulation results are obtained by conducting  $10^5$  independent runs where we accordingly compute the average and maximum SRL (ASRL and MSRL).

Figure 11 depicts the SRL results for the asymmetric-role SH schemes (our PES-SH and Li and Xie's SH [28]). The results illustrate the significant reduction on the SRL provided by our PES-SH in terms of ASRL and MSRL under all the different antenna configurations of the pair of SUs. For some antenna configurations, PES-SH can reduce the ASRL and MSRL significantly up to 80% and 84%, respectively. The shorter ASRL and MSRL provided by the PES-SH scheme are due to its efficient design which relies on the coprimality between the adjusted prime and even numbers of  $N_i$  and  $N_j$ , respectively. And since  $N_i$  is prime for all the sender

Time slot	0	1	2	3	4	5	6	7	8	9	10	11	12	13	14	15	16	17	18	19	20	21	22	23	24	25	26	27	28	29	30	31	32	33	34	35	36																																							
$SCH_X$	1	2	1	4	1	2	1	4	2	1	2	6	3	5	3	6	3	5	3	6	4	3	4	7	4	3	4	7	5	4	5	3	5	4	5	3	1	2	1	4	2	1	2	6	2	1	2	6	3	5	3	6	3	5	3	6	4	3	4	7	4	3	4	7	5	4										
$SCH_{Y,1}$	1	6	1	6	1	8	1	8	2	4	2	4	2	9	2	9	3	1	3	1	3	6	3	6	4	5	4	5	4	6	4	6	1	6	1	6	1	8	1	8	2	4	2	4	2	9	2	9	3	1	1	6	3	6	4	5	4	5	4	6	4	6	1	6	1	6	1	8	1	8	2	4	2	4		
$SCH_{Y,2}$	1	6	1	6	1	8	1	8	2	4	2	4	2	9	2	9	3	1	3	1	3	6	3	6	4	5	4	5	4	6	4	6	1	6	1	6	1	8	1	8	2	4	2	4	2	9	2	9	3	1	3	1	3	6	4	5	4	5	4	6	4	6	1	6	1	6	1	8	1	8	2	4	2	4	2	9
$SCH_{Y,3}$	1	6	1	6	1	8	1	8	2	4	2	4	2	9	2	9	3	1	1	6	3	6	4	5	4	5	4	6	4	6	1	6	1	6	1	8	1	8	2	4	2	4	2	9	2	9	3	1	3	1	3	6	4	5	4	5	4	6	4	6	1	6	1	6	1	8	1	8	2	4	2	4	2	9		

FIGURE 10: Asynchronous rendezvous between  $SU_X$  and  $SU_Y$  according to the combined PES-SCH scheme for  $n = 2$  best-ranked channels.  $SCH_Y$  is started earlier than  $SCH_X$  with  $\delta_s \in [1, 3]$ .

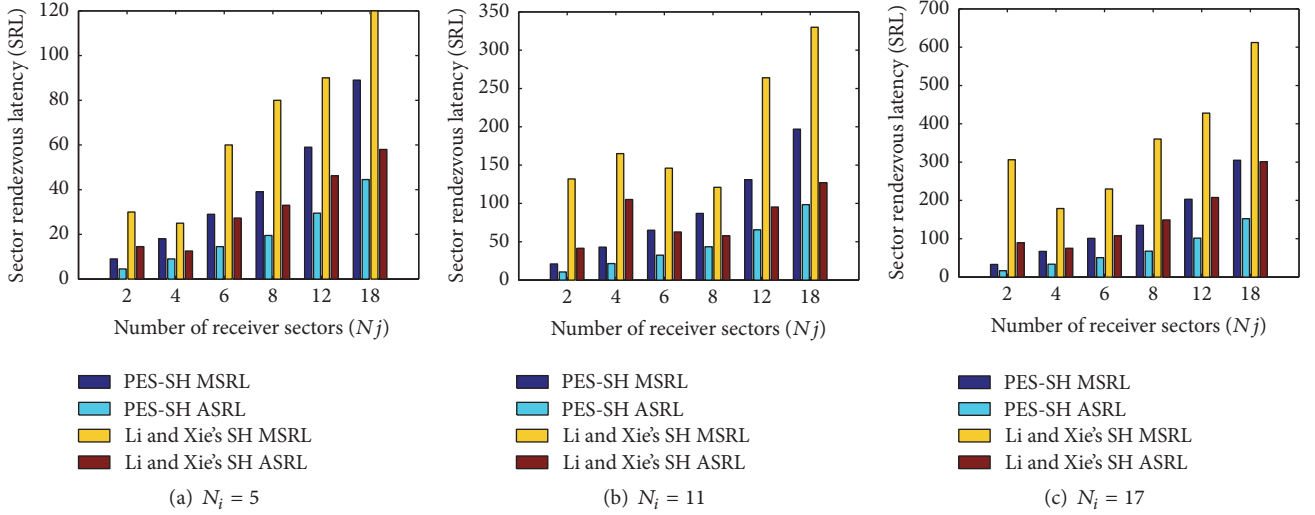


FIGURE 11: Comparison of the sector rendezvous latency between our PES-SH scheme and Li and Xie's SH scheme [28] under fixed  $N_i$  and varying  $N_j$ .

$SU_i$  antenna configurations while the values of  $N_j$  are even numbers that are valid for use (i.e., not in the AES set), this allows the sender  $SU_i$  in our PES-SH to achieve sector rendezvous with its receiver  $SU_j$  within  $N_i N_j$  SH period.

On the other side, the design of Li and Xie's SH scheme requires  $N_i$  and  $N_j$  to be adjusted to primes. Furthermore, the sender should perform an initiating round-robin SH sequence with a length of  $N_i^2$  before it converts to the regular prime-based sequence. Accordingly, this will prolong the SH period needed for achieving the sector rendezvous to  $(N_i^2 + N_i P_j)$  which actually represents the theoretical upper bound for the MSRL of Li and Xie's SH scheme when  $(N_i \neq P_j)$ . We can notice that this upper bound is tight for some  $(N_i$  and  $N_j)$  combinations, while it is not for others. Specifically, when  $(N_i \% P_j = 1)$  where  $P_j$  is the adjusted prime for  $N_j$ , the sender  $SU_i$  cannot rendezvous with its receiver during its initiating  $N_i^2$  round-robin SH sequence. However, when it starts following the regular prime-based SH sequence, the sector rendezvous happens within the subsequent  $N_i P_j$  slots, which results in  $(N_i^2 + N_i P_j)$  MSRL. For example, when  $N_i = 11$  and  $N_j = 4$  in Figure 11(b), the sector rendezvous occurs in  $(121 + 11 \times 5) = 165$  sector slots. The same thing can be noticed for the cases when  $N_j = 2$  in Figures 11(a), 11(b), and 11(c), where the MSRL is  $(N_i^2 + N_i \times 2)$ . This explains the irregular increased results in the figures for such  $(N_i$  and  $N_j)$  combinations.

In Figure 12, the SRL results for the symmetric-role SH schemes (our IPES-SH and the Chen et al.'s SH scheme [30]) are shown. In the figure, it is shown that our IPES-SH scheme outperforms the other compared scheme especially in terms of MSRL. This improvement is due to the shorter SH period provided by IPES for achieving the sector rendezvous. In both schemes, the SH period for sector rendezvous depends mainly on the extended ID length as well as the adjusted numbers for  $(N_i$  and  $N_j)$  that are used for constructing the interleaved sequences. However, the adjusted parameters used by our IPES scheme are smaller than those used by the other scheme. Firstly, in the IPES-SH scheme, the extended ID length is  $2m = 14$  which is relatively smaller than the  $2m + 1 = 15$  extended ID used by the other scheme. Furthermore, the interleaved SH sequences in Chen et al.'s SH scheme are constructed by adjusting the number of sectors to a prime number as well as to a number that is a power-multiple of two (i.e.,  $q_k = 2^{b_k}$ , where  $b_k$  is the smallest integer satisfying  $2^{b_k} \geq N_k$ ). However, these adjusted numbers must be coprime with the extended ID length in order to achieve a successful sector rendezvous. Meanwhile, in IPES-SH, the interleaved PS and ES sequences are constructed based on the closest prime number and the closest even number which is not in the AES set. Hence, under most of the simulated antenna configurations, the adjusted  $E_i$  and  $E_j$  in IPES are smaller than the adjusted  $q_i$  and  $q_j$  parameters in the other scheme.

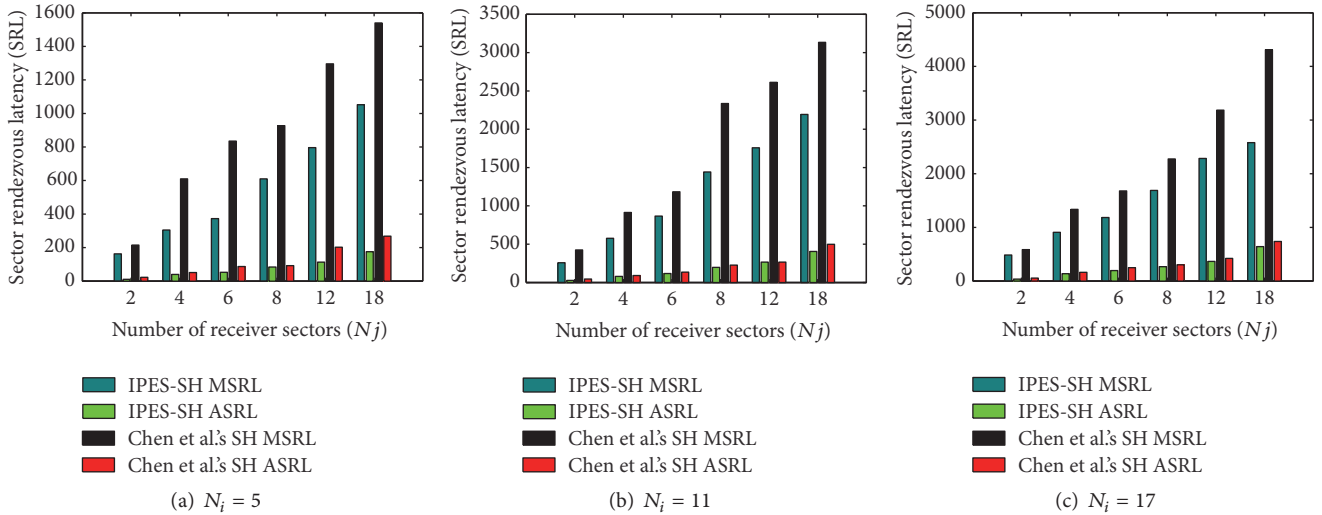


FIGURE 12: Comparison of the sector rendezvous latency between our IPES-SH scheme and Chen et al.'s SH scheme [30] under fixed  $N_i$  and varying  $N_j$ . ID length = 7 bits.

For example, in our IPES-SH scheme,  $E_j = N_j$  for all the  $N_j$  values, while the  $q_j$  adjusted parameters for the  $N_j$  values in Chen et al.'s SH scheme are  $\{2, 4, 8, 16, 32\}$ . Moreover, when  $N_i$  or  $N_j$  is  $\leq 5$ , the adjusted prime number used in IPES is 5, while it is 7 on the other scheme because 7 is the closest prime that is coprime with the 15-bit extended ID. According to that, SUs in the IPES scheme can achieve the sector rendezvous faster than Chen et al.'s SH scheme.

### 6.2. Performance Comparison of the Combined SCH Schemes.

In this subsection, we compare the channel rendezvous performance of our SCH schemes with the other works under a practical DIR-CRN. The simulation configuration parameters are shown in Table 1.

We start our SCH simulation by comparing the performance of our combined PES-SCH with the combined SCH schemes of Song and Xie [19] and Li and Xie [28]. We evaluate our PES-SCH for  $n = 4$  best-quality channels which correspond to a AGQ-CH period of 16 time slots in each sector (i.e., the frame length = 16). The other selected schemes for comparison are simulated with their proposed CH schemes. In [19], the SH scheme is combined with the asymmetric-role CH scheme in [35], where the sender SU stays for  $L^2$  slots on each sector frame of its SH sequence performing a sequential fast CH on the ( $C_i \leq L$ ) available channels within the sector. Meanwhile, the receiver SU stays for  $(N_i + 1) \times L^2$  slots on each sector of its  $N_i$  sectors performing a slow CH on all of its ( $C_j \leq L$ ) available channels. On the other side, the SH scheme of Li and Xie [28] is combined with the EJS-CH scheme [10]. However, due to the long period of the EJS-CH scheme required to guarantee channel rendezvous, Li and Xie simulated their SCH scheme by letting SUs stay for smaller period on each sector of their SH frames. During this period, SUs execute the corresponding subsequences of their generated EJS-CH sequence. Therefore, we simulate Li and Xie's SCH scheme

TABLE 1: Simulation parameters.

Network area deployment	500 m $\times$ 500 m
Number of channels ( $L$ )	10
Number of PUs	50
The radius of the SU sensing/transmission range	150 m
Slot duration for sending a packet on a channel	2 ms
The PU packet arrival rate	10 packets/s
The length of a PU packet	120 slots

with a similar sector frame length to our PES-SCH scheme (i.e., 16 slots). All the schemes are simulated under different asynchronous settings where the clock drifts amount between SUs is selected randomly in each experiment.

Figure 13 depicts the TTR simulation results for the three schemes when they are evaluated under different antenna configurations for the pair of SUs. Even though the combined SCH scheme of Song and Xie is not a blind scheme, it produces very long TTR results. This is due to the large sector frame length where the sender and receiver stay for  $L^2$  and  $L^2 \times (N_i + 1)$  time slots, respectively, on each sector for performing their corresponding CH sequence. As a consequence, the SCH period needed for achieving rendezvous is  $N_j \times (L^2 \times (N_i + 1))$  which is very long as compared to the period of our PES-SCH scheme. On the other side, Li and Xie's SCH scheme can provide shorter ATTR than Song and Xie's scheme because it is simulated with smaller frame length. However, the MTTR of this scheme cannot be traced because we observe that TTR in some cases cannot be achieved within the whole simulation duration which is set to  $5 \times 10^4$  slots. The reason for the indeterministic behaviour of Li and Xie's SCH scheme is because the stay period in each sector (i.e., 16 slots) is insufficient to guarantee rendezvous while using the EJS-CH scheme. According to the EJS-CH

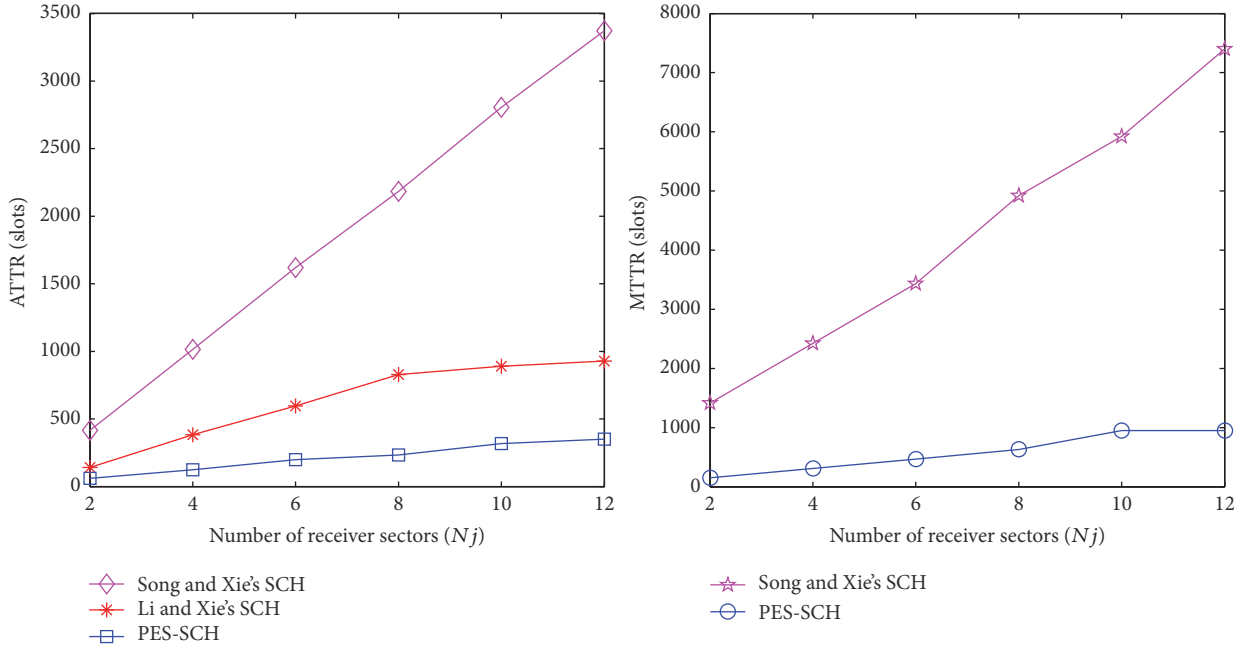


FIGURE 13: Comparison of the time-to-rendezvous (TTR) between the asymmetric-role SCH schemes when  $N_i = 5$ .

[10], the rendezvous cannot be guaranteed unless the EJS-CH sequences of the communicating SUs are overlapped for at least  $4P_L(P_L + 1 - G) = 44(12 - G)$  time slots.  $P_L$  is the smallest prime number greater than  $L$ , while  $G$  is the number of common available channels between the SUs available channels. Hence, to ensure rendezvous regardless of any misalignment of their local clocks, the SUs should stay for at least  $4P_L^2$  on each sector of their SH sequences to perform their EJS-CH sequences. This trade-off between the bounded MTTR of Song and Xie's SCH scheme and the small ATTR of Li and Xie's SCH scheme illustrates the efficiency of our proposed AGQ-CH scheme, which allows PES-SCH to guarantee rendezvous with the shortest TTR results.

In the second setting of the SCH simulation, we combine the SH schemes of Li and Xie [28] and Chen et al. [30] with our proposed AGQ-CH scheme. This is in order to evaluate their channel rendezvous performance when they are combined with an efficient and suitable CH scheme. Figures 14 and 15 show the TTR results of these schemes and our schemes when they are simulated for different values of the best-quality channel  $n$  ( $2 \leq n \leq 5$ ). In the simulation, we consider different values for the sender number of sectors ( $N_i = \{4, 6, 12\}$ ), while the receiver number of sectors  $N_j$  is set as 4. The figures show that our schemes always outperform the other schemes under all the different antenna configurations of the SUs. This is mainly due to the shorter SRL of our SH schemes and, as explained in Section 5.4, TTR depends on the SRL of the SH scheme coupled with the length of the sector frame ( $n^2$ ). Moreover, the figures illustrate the effect of  $n$  (i.e., the number of best-quality channels) on the rendezvous performance where we can notice that as  $n$  increases, the TTR results for all the schemes increase.

This is because the larger  $n$ , the longer the frame length  $n^2$ . Accordingly, when SUs spend longer period in each sector, they may waste more time while attempting rendezvous on other sectors rather than the rendezvous sector. This will result in a longer TTR until they can achieve a successful sector and channel rendezvous.

Finally, to illustrate the performance gain brought by applying directional antennas for channel rendezvous, we compare the performance of our combined PES-SCH scheme with the AAsync-CH omnidirectional antenna rendezvous scheme [16]. The AAsync-CH is selected among the other omnidirectional CH schemes since it is designed for asymmetric-role environment (i.e., SUs have preassigned role) similar to our PES-SCH. The schemes are compared in terms of their probabilities for achieving a successful channel rendezvous under different number of PUs in the network area. In our PES-SCH, the simulated sender and receiver SUs have  $N_i = 5$  and  $N_j = 6$  number of sectors and the number of best-quality channels  $n = 3$ .

Figure 16 shows the significant outperformance of our directional antenna scheme as compared with the omnidirectional antenna scheme. It can be noticed from the figure that when the number of PUs in the network increases, the probability of the successful channel rendezvous for the omnidirectional scheme decreases dramatically. Meanwhile, in the PES-SCH, this probability is almost 1 for most of the cases and only decreases slightly when the number of PUs is close to 100. This is due to the smaller interference region of the directional antenna, which results in higher channel availability for the SUs as compared to the omnidirectional antenna. So, when the total number of PUs in the network area increases, only few of them may reside within

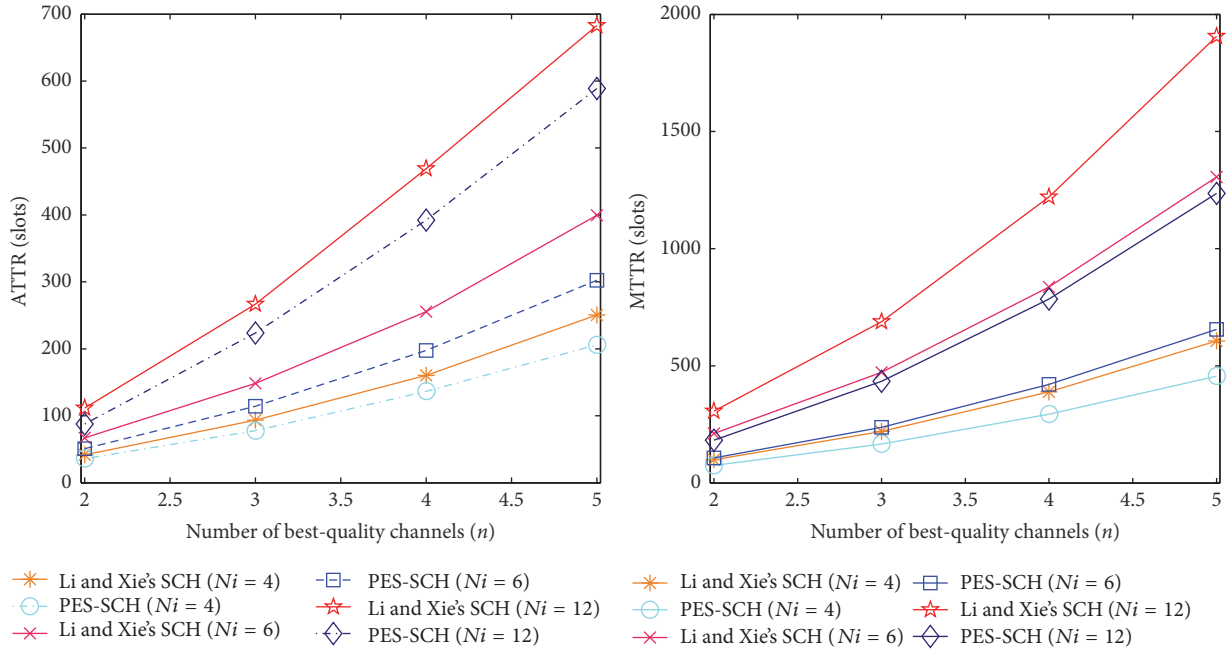


FIGURE 14: Comparison of the time-to-rendezvous (TTR) between the asymmetric-role SCH schemes when  $N_j = 4$ .

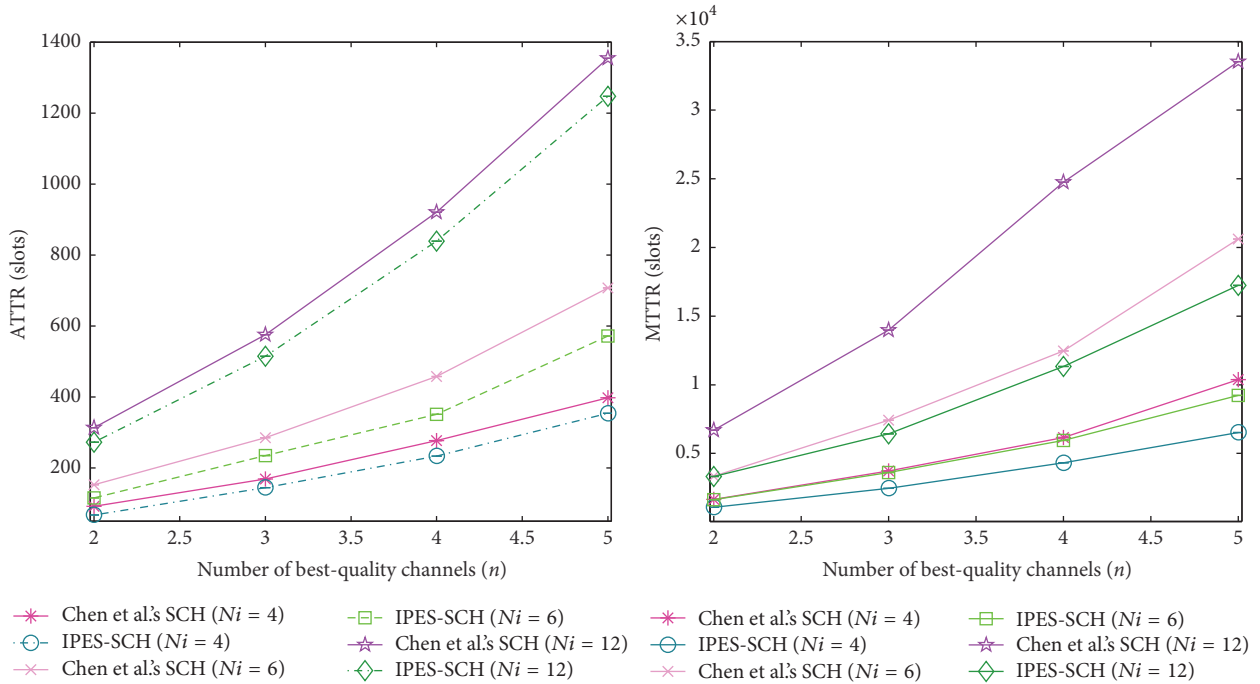


FIGURE 15: Comparison of the TTR between the symmetric-role SCH schemes when  $N_j = 4$ . ID length = 7 bits.

the SUs rendezvous sectors where they can only impose a slight change in the channel availability. Accordingly, the probability of having common channels between the SUs on their sector rendezvous pair is always high, which increases the probability of successful channel rendezvous.

These results justify the motivation of our proposed schemes where equipping SUs with directional antennas can significantly enhance the channel rendezvous performance in high-density PU networks as compared with the omnidirectional antennas paradigm.

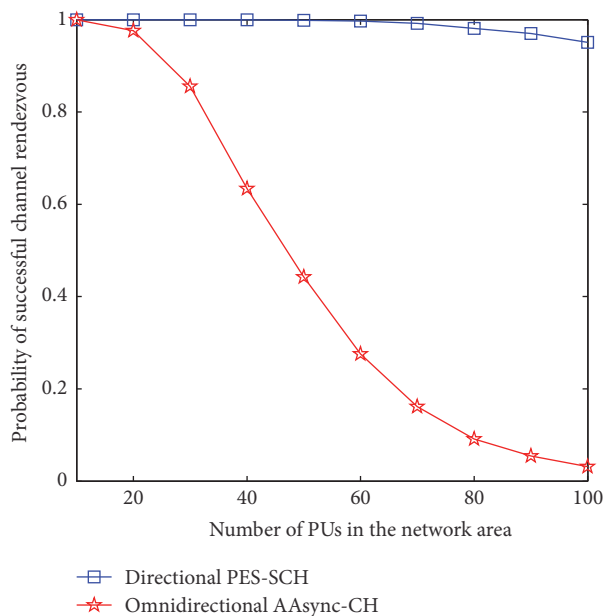


FIGURE 16: Comparison of the successful channel rendezvous probability between our PES-SCH directional antenna scheme and the AAsync-CH omnidirectional scheme.

## 7. Conclusions

In this paper, we studied the sector and channel rendezvous problem for SUs in DIR-CRNs. Two efficient coprimality-based sector hopping schemes have been proposed for providing sector rendezvous in asymmetric- and symmetric-role environments. The SH schemes are combined with an efficient grid-quorum-based CH scheme for providing a guaranteed sector and channel rendezvous simultaneously between the SUs in DIR-CRNs. Theoretical analysis and extensive simulations are conducted to demonstrate the efficiency of the proposed schemes. The simulation results verify that our schemes significantly outperform the previous directional antenna rendezvous schemes (in terms of SRL and TTR). Furthermore, they demonstrate that our directional antenna rendezvous paradigm is more resistant to rendezvous failures under high-density PU CRNs, as compared with the omnidirectional antenna rendezvous paradigm.

## Conflicts of Interest

The authors declare that they have no conflicts of interest.

## Acknowledgments

The authors would like to acknowledge Malaysian Ministry of Higher Education for funding this study under the Fundamental Research Grant Scheme (FRGS) entitled “On the Cogitation of Primary User Reappearance in Cognitive Radio Network” (Project Code: MOHE: FRGS/1/2015/TK10/UPM/02/2, UPM:03-01-15-1626FR, Vote no. 5524731).

## References

- [1] N. C. Theis, R. W. Thomas, and L. A. DaSilva, “Rendezvous for cognitive radios,” *IEEE Transactions on Mobile Computing*, vol. 10, no. 2, pp. 216–227, 2011.
- [2] B. F. Lo, “A survey of common control channel design in cognitive radio networks,” *Physical Communication*, vol. 4, no. 1, pp. 26–39, 2011.
- [3] M.-R. Kim and S.-J. Yoo, “Distributed coordination protocol for ad hoc cognitive radio networks,” *Journal of Communications and Networks*, vol. 14, no. 1, pp. 51–62, 2012.
- [4] P. Ren, Y. Wang, and Q. Du, “CAD-MAC: a channel-aggregation diversity based MAC protocol for spectrum and energy efficient cognitive Ad Hoc networks,” *IEEE Journal on Selected Areas in Communications*, vol. 32, no. 2, pp. 237–250, 2014.
- [5] G. Prasad Joshi, S. Y. Nam, S. W. Kim, and B.-S. Kim, “Adaptive window size-based medium access control protocol for cognitive radio wireless sensor networks,” *Journal of Sensors*, vol. 2016, Article ID 2049859, 9 pages, 2016.
- [6] S. Omar, O. E. Ghandour, and A. M. A. El-Haleem, “Multipath activity based routing protocol for mobile cognitive radio Ad Hoc networks,” *Wireless Communications and Mobile Computing*, vol. 2017, Article ID 5380525, 12 pages, 2017.
- [7] A. Mahmud, Y. Lee, and I. Koo, “A fully distributed resource allocation mechanism for CRNS without using a common control channel,” *Mathematical Problems in Engineering*, vol. 2015, Article ID 537078, 9 pages, 2015.
- [8] G. P. Joshi, S. Y. Nam, and S. W. Kim, “Rendezvous issues in ad hoc cognitive radio networks,” *KSII Transactions on Internet and Information Systems*, vol. 8, no. 11, pp. 3655–3673, 2014.
- [9] S. Romaszko, “A rendezvous protocol with the heterogeneous spectrum availability analysis for cognitive radio ad hoc networks,” *Journal of Electrical and Computer Engineering*, vol. 2013, Article ID 715816, 18 pages, 2013.
- [10] Z. Lin, H. Liu, X. Chu, and Y.-W. Leung, “Enhanced jump-stay rendezvous algorithm for cognitive radio networks,” *IEEE Communications Letters*, vol. 17, no. 9, pp. 1742–1745, 2013.
- [11] J. Kim, G. Park, and K. Han, “A Rendezvous Scheme for Self-Organizing Cognitive Radio Sensor Networks,” *International Journal of Distributed Sensor Networks*, vol. 10, no. 1, article 315874, 2014.
- [12] E. O. Guerra, V. A. Reguera, R. D. Souza, E. G. Fernández, and M. E. Pellenz, “Systematic construction of common channel hopping rendezvous strategies in cognitive radio networks,” *EURASIP Journal on Wireless Communications and Networking*, vol. 2015, no. 1, 2015.
- [13] G.-Y. Chang, J.-F. Huang, and Y.-S. Wang, “Matrix-based channel hopping algorithms for cognitive radio networks,” *IEEE Transactions on Wireless Communications*, vol. 14, no. 5, pp. 2755–2768, 2015.
- [14] B. Yang, W. Liang, M. Zheng, and Y.-C. Liang, “Fully distributed channel-hopping algorithms for rendezvous setup in cognitive multi-radio networks,” *IEEE Transactions on Vehicular Technology*, vol. PP, no. 99, 2015.
- [15] J.-P. Sheu, C.-W. Su, and G.-Y. Chang, “Asynchronous quorum-based blind rendezvous schemes for cognitive radio networks,” *IEEE Transactions on Communications*, vol. 64, no. 3, pp. 918–930, 2016.
- [16] P. K. Sahoo and D. Sahoo, “Sequence-based channel hopping algorithms for dynamic spectrum sharing in cognitive radio networks,” *IEEE Journal on Selected Areas in Communications*, vol. 34, no. 11, pp. 2814–2828, 2016.

- [17] W. Chen, G. Yang, M. Chang, and W. C. Kwong, "Construction and analysis of shift-invariant, asynchronous-symmetric channel-hopping sequences for cognitive radio networks," *IEEE Transactions on Communications*, vol. 65, no. 4, pp. 1494–1506, 2017.
- [18] A. Al-Mqdashi, A. Sali, M. J. Abdel-Rahman, N. K. Noordin, S. J. Hashim, and R. Nordin, "Efficient rendezvous schemes for fast-varying cognitive radio ad hoc networks," *Transactions on Emerging Telecommunications Technologies*, article e3217, 2017. <http://dx.doi.org/10.1002/ett.3217>.
- [19] Y. Song and J. Xie, "Enhancing channel rendezvous in cognitive radio networks with directional antennas," in *Proceedings of the IEEE International Conference on Communications, ICC 2015*, pp. 3702–3707, June 2015.
- [20] H. Jung and I.-H. Lee, "Connectivity Analysis of Millimeter-Wave Device-to-Device Networks with Blockage," *International Journal of Antennas and Propagation*, vol. 2016, Article ID 7939671, 9 pages, 2016.
- [21] A. M. Al-Samman, T. A. Rahman, M. H. Azmi et al., "Statistical modelling and characterization of experimental mm-wave indoor channels for future 5G wireless communication networks," *PLoS ONE*, vol. 11, no. 9, pp. 1–29, 2016.
- [22] Y. Zhao, Z. Wei, Y. Liu, Q. Zhang, and Z. Feng, "Angle-Domain Spectrum Holes Analysis with Directional Antenna in Cognitive Radio Network," in *Proceedings of the 2017 IEEE Wireless Communications and Networking Conference (WCNC)*, pp. 1–6, San Francisco, CA, USA, March 2017.
- [23] H. Yazdani and A. Vosoughi, "On cognitive radio systems with directional antennas and imperfect spectrum sensing," in *Proceedings of the 2017 IEEE International Conference on Acoustics, Speech and Signal Processing (ICASSP)*, pp. 3589–3593, New Orleans, LA, USA, March 2017.
- [24] Y. Dai and J. Wu, "Boundary helps: Efficient routing protocol using directional antennas in cognitive radio networks," in *Proceedings of the 10th IEEE International Conference on Mobile Ad-Hoc and Sensor Systems, MASS 2013*, pp. 502–510, October 2013.
- [25] S. Anamalamudi, M. Jin, and J. M. Kim, "Hybrid CCC based AODV routing protocol for cognitive radio ad-hoc networks with directional antennas," in *Proceedings of the 7th International Conference on Ubiquitous and Future Networks, ICUFN 2015*, pp. 40–45, July 2015.
- [26] Y. Wang, Q. Wang, H.-N. Dai, H. Wang, Z. Zheng, and J. Li, "On local connectivity of cognitive radio ad hoc networks with directional antennas," in *Proceedings of the 2016 IEEE International Conference on Communication Systems, ICCS 2016*, pp. 1–6, December 2016.
- [27] L. T. Dung, T. D. Hieu, S.-G. Choi, B.-S. Kim, and B. An, "Impact of beamforming on the path connectivity in cognitive radio ad hoc networks," *Sensors*, vol. 17, no. 4, 2017.
- [28] J. Li and J. Xie, "Directional antenna based distributed blind rendezvous in cognitive radio ad-hoc networks," in *Proceedings of the 58th IEEE Global Communications Conference, GLOBECOM 2015*, pp. 1–6, December 2015.
- [29] C.-M. Chao, H.-Y. Fu, and L.-R. Zhang, "A fast rendezvous-guarantee channel hopping protocol for cognitive radio networks," *IEEE Transactions on Vehicular Technology*, vol. 64, no. 12, pp. 5804–5816, 2015.
- [30] L. Chen, Y. Li, and A. V. Vasilakos, "Oblivious neighbor discovery for wireless devices with directional antennas," in *Proceedings of the 35th Annual IEEE International Conference on Computer Communications, IEEE INFOCOM 2016*, pp. 1–9, April 2016.
- [31] I. Niven, H. S. Zuckerman, and H. Montgomery, *An Introduction to the Theory of Numbers*, John Wiley & Sons, New York, NY, USA, 1991.
- [32] K. Bian and J.-M. J. Park, "Maximizing rendezvous diversity in rendezvous protocols for decentralized cognitive radio networks," *IEEE Transactions on Mobile Computing*, vol. 12, no. 7, pp. 1294–1307, 2013.
- [33] M. J. Abdel-Rahman and M. Krunz, "Game-theoretic quorum-based frequency hopping for anti-jamming rendezvous in DSA networks," in *Proceedings of the 2014 IEEE International Symposium on Dynamic Spectrum Access Networks, DYSPAN 2014*, pp. 248–258, April 2014.
- [34] A. Al-Mqdashi, A. Sali, N. K. Noordin, S. J. Hashim, R. Nordin, and M. J. Abdel-Rahman, "An efficient quorum-based rendezvous scheme for multi-radio cognitive radio networks," in *Proceedings of the 2016 IEEE 3rd International Symposium on Telecommunication Technologies (ISTT)*, pp. 59–64, November 2016.
- [35] Y. Song and J. Xie, "QB<sup>2</sup>IC: A QoS-based broadcast protocol under blind information for multihop cognitive radio ad hoc networks," *IEEE Transactions on Vehicular Technology*, vol. 63, no. 3, pp. 1453–1466, 2014.